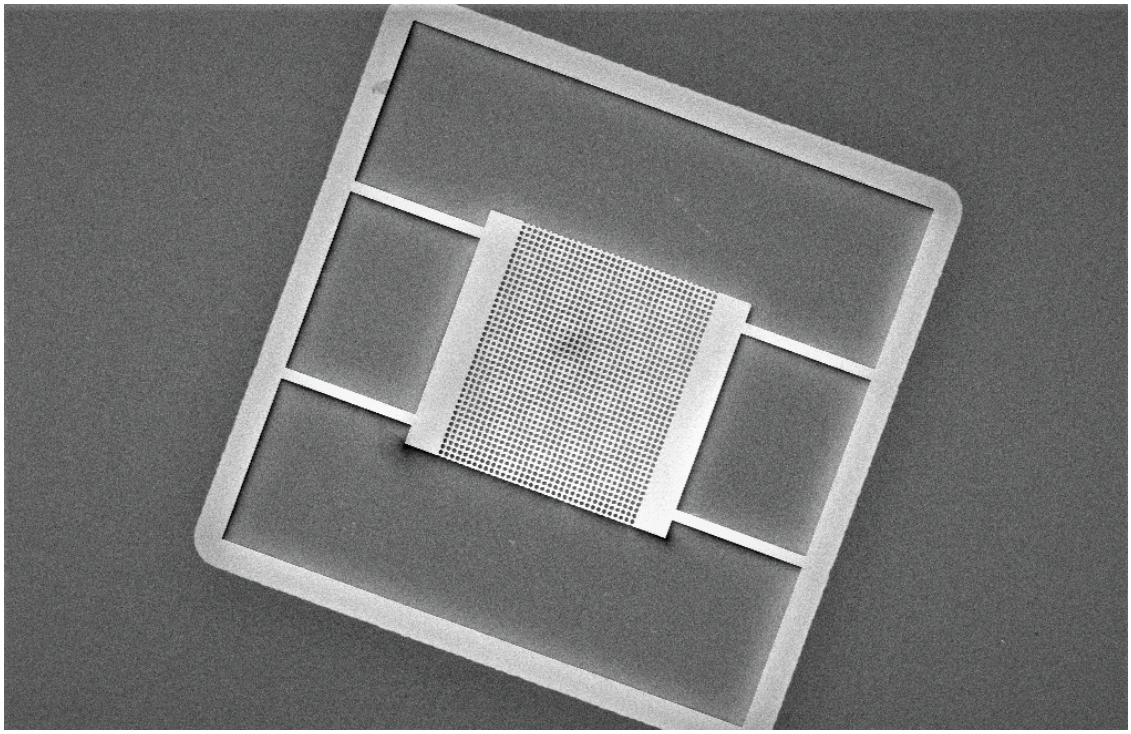

High Reflectivity GaAs-based Photonic Crystal Reflectors for Cavity Optomechanics

Master's Thesis in the Erasmus Mundus Master of Science in Nanoscience and Nanotechnology

KARIM ELKHOULY

Department of Microtechnology and Nanoscience
CHALMERS UNIVERSITY OF TECHNOLOGY
Gothenburg, Sweden 2019

With the support of the Erasmus+ Programme of the European Union

Master's thesis 2019

High Reflectivity GaAs-based Photonic Crystal Reflectors for Cavity Optomechanics

KARIM ELKHOULY

CHALMERS
UNIVERSITY OF TECHNOLOGY

Department of Microtechnology and Nanoscience (MC2)
Division of Quantum Technology Laboratory
Chalmers University of Technology
Gothenburg, Sweden 2019

High Reflectivity GaAs-based Photonic Crystal Reflectors for Cavity Optomechanics

KARIM ELKHOULY

Assistant Supervisor: Sushanth Kini, MC2 Department, Chalmers
Promoter and Supervisor: Witlef Wieczorek, MC2 Department, Chalmers
Co-promoter: Pol Van Dorpe, ESAT Department, KU Leuven

Master's Thesis 2019
Department of Microtechnology and Nanoscience (MC2)
Division of Quantum Technology Laboratory
Chalmers University of Technology
SE-412 96 Gothenburg
Telephone +46 31 772 1000

Cover: Scanning electron microscope image of a photonic crystal patterned GaAs membrane.

Typeset in LaTeX
Printed by Chalmers Reproservice, Chalmers University of Technology
Gothenburg, Sweden 2019

High Reflectivity GaAs-based Photonic Crystal Reflectors for Cavity Optomechanics
KARIM ELKHOULY
Department of Microtechnology and Nanoscience (MC2)
Chalmers University of Technology

Abstract

Cavity optomechanical devices couple light and mechanical motion. These devices enable reaching the quantum regime of mechanical motion, and thus, achieving the ultimate limits of sensing, and offer opportunities for hybrid quantum hardware. A current limitation in the field of cavity optomechanics is the weak coupling on the single photon level. Multi-element optomechanics has been proposed to enter the regime of strong coupling by enhancing the interaction strength in an array of high-reflectivity mechanical membranes placed inside a Fabry-Pérot cavity. This thesis investigates photonic crystal patterned GaAs-based single membrane devices, which constitute the building block of the multi-element optomechanical system. Homodyne detection was used for the mechanical characterization of GaAs membranes. Best performing devices achieved quality factors $\sim 10^4$. Furthermore, a mechanical mode tomography technique was developed, which allowed probing the mode shapes of the mechanical eigenmodes, and thus, comparing them to simulations. Photonic crystal patterns were designed to enhance the reflectivity of GaAs membranes. Optical characterization demonstrated devices with reflectivity $> 98\%$. Moreover, unexpected Fano resonances appeared in the reflectivity spectrum. Rigorous coupled wave analysis was used to model the photonic crystal membrane, and it is shown that the parasitic feature is due to probing the membrane with a Gaussian beam of finite beam size. The feature is studied with respect to several physical parameters such as photonic crystal parameters, beam waist and beam polarization. The mechanical and optical properties shown in this thesis demonstrate the possibility of tuning the reflectivity of GaAs membranes, without degrading their mechanical properties. This is an important step towards the demonstration of a multi-element optomechanical system in the single-photon strong coupling regime based on GaAs membranes.

Keywords: multi-element optomechanics, GaAs membrane, photonic crystal slabs, mode tomography, plane wave decomposition.

To my beloved mother
To my father, who remains my everlasting source of inspiration

Acknowledgements

First and foremost, I would like to thank my promoter Assistant Prof. Witlef Wieczorek for giving me the opportunity to work in his laboratory. At all times, Witlef has given me valuable support. I thank him for his guidance, for his trust and for allowing me to pursue my passion towards science under his supervision.

Secondly, I would like to thank my daily supervisor Sushanth Kini. Sushanth has been a great mentor throughout this thesis. His support in the lab and our scientific discussions were critical for the success of my work. I wish you all the best for your PhD and for your future life.

Thirdly, I would like to thank my co-promoter Associate Prof. Pol Van Dorpe for supervising this thesis. Pol has given me the opportunity to do a research internship in his group at IMEC last summer. It was an exciting research experience.

Next, I would like to express my sincere gratitude to Marti. Although this work was not part of his research topic, Marti supported me with an extremely valuable input and fruitful scientific discussions. I will also miss our short conversations during coffee breaks. I wish you all the best for your PhD and future plans. I would also like to thank Matthias for his support. Matthias designed the electronic board which was crucial for the optical reflectivity measurements and was always supportive. Moreover, I would like to thank Jamie Fitzgerald and Associate Prof. Philippe Tassin. Their input and scientific discussions about photonic crystals was extremely important for solving the problems I tackled in this thesis.

Then, I would like to thank the Professors of the EMM-Nano program. The program was an amazing experience thanks to them. I would like to especially thank Prof. Michel Houssa, Prof. Marc Heyns and Prof. Bart Sorée for their courses which helped shape my knowledge. I would also like to thank Associate Prof. Thilo Bauch, who made my stay here in Chalmers an extremely smooth and enjoyable experience. I would like to thank everyone who contributed to this master's program, and express my gratitude towards the European Commission for supporting me with the scholarship that made this work possible.

Furthermore, I would like to thank my friends here in Gothenburg. I would like to mention Kristi, Andres, Ruben and Amr. Our chats, outings and amazing trips have helped me clear lots of the frustration and stress from work. I want also to thank all my friends in the EMM-Nano program. I wish you all the best in your lives.

Last but not least, I would like to thank my family. My mother Maha, my brother Ahmed, my sister Eman, my brother-in-law Mostafa and my little nephew Omar. It is your presence and support that made this possible, being thousands of kilometers away from home.

Karim Elkhouly, Gothenburg, July 2019

Contents

List of Figures

List of Tables

1

Introduction

This chapter starts with giving an intuitive explanation to cavity optomechanics, and showing how light and mechanical motion can be coupled through radiation pressure force. Then, the most notable achievements in the field are briefly mentioned, and the current challenges which prevent reaching the single-photon strong coupling regime are elaborated. Furthermore, multi-element optomechanics is introduced as a promising approach to enter this regime. The main concept behind the multi-element optomechanics approach is discussed, and several examples of state of the art progress are shown. Finally, our approach of using GaAs/AlGaAs heterostructures is motivated and the thesis organization is discussed.

1.1 Cavity optomechanics

The research field of cavity optomechanics has emerged within the last decades. Cavity optomechanics exploits the interaction between electromagnetic radiation and mechanical resonators mediated by the radiation pressure force [Aspelmeyer et al., 2014]. Photons carry momentum $p = \hbar k$; whenever momentum exchange takes place, a force is exerted on the mechanical body, this is the radiation pressure force. The simple system in Fig 1.1 intuitively explains the basic concept of cavity optomechanics. If we assume an optical cavity with a fixed mirror and another movable mirror excited by an external laser, then photons exert radiation pressure force during each round-trip inside the cavity. As a result, photons affect the mechanical degree of freedom of the mirror. On the other hand, as the mirror moves, the cavity length changes which alters the light path and the resonance properties of the cavity. This simple model summarizes the main concept of cavity optomechanics. A simple derivation for the optomechanical Hamiltonian of this system is done in section 2.3.

The experimental realization of laser cooling in the field of quantum optics was a major breakthrough that allowed many exciting physics experiments. For example, cooling of ions into their quantum mechanical ground state. The possibility of using radiation pressure force to control the mechanical motion of macroscopic objects became interesting, and the first optomechanical effect was observed by demonstrating radiation-pressure bistability on a macroscopic end mirror [Dorsel et al., 1983].

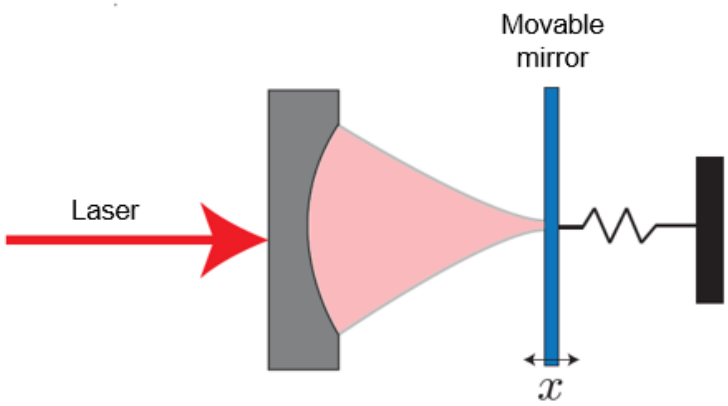

Figure 1.1: Simple model for a cavity optomechanics system with a fixed mirror and a movable mirror excited by an external laser. Courtesy of Sushanth Kini, Chalmers.

Within the last decades, the advances in micro-fabrication technology have led to the realization of micron-sized mechanical resonators with small mass and high mechanical quality factor Q_m which allowed to enter the regime of coherent cavity optomechanics [Aspelmeyer et al., 2014]. Parametric instability in optical microtoroid resonators was the first optomechanical effect demonstrated in this new regime [Kippenberg et al., 2005]. Radiation pressure cavity cooling was demonstrated by several teams in 2006 [Arcizet et al., 2006; Gigan et al., 2006; Schliesser et al., 2006]. The research field has highly evolved since then and optomechanical effects were reported in a multitude of systems. Some examples are membranes in Fabry-Pérot cavities [Thompson et al., 2008], microdisks [Wiederhecker et al., 2009], and photonic crystals (PhCs) [Eichenfield et al., 2009]. Ground state cooling of a nanomechanical resonator on a silicon microchip by means of radiation pressure force from a laser was demonstrated in 2011 [Chan et al., 2011]; a scanning electron microscope image of the device is shown in Fig. 1.2a. Another exciting development is bidirectional transduction between microwave and optical photons [Andrews et al., 2014].

Despite the huge progress in the field of cavity optomechanics, one of the main remaining challenges is to achieve the single-photon strong coupling regime, in which a single photon could displace a mechanical resonator by δx which is bigger than its zero point fluctuations x_{ZPF}. At the same time, the presence of one photon in the cavity should shift the cavity resonance ω_{cav} by $\delta\omega$ which is larger than the cavity linewidth κ. In physical terms, achieving such goal requires the single-photon optomechanical coupling strength g_0 to be much larger than the mechanical damping rate γ_m and optical losses κ in the system; i.e. $g_0 \gg \gamma_m, \kappa$ [Aspelmeyer et al., 2014]. Entering the strong coupling regime will allow preparing non-Gaussian states of mechanical motion directly [Ludwig et al., 2008]. Optomechanical systems operating in this regime could be used for single photon detection [Aspelmeyer et al., 2014]. Moreover, quantum non-demolition measurement of phonon number will be possible [Thompson et al., 2008].

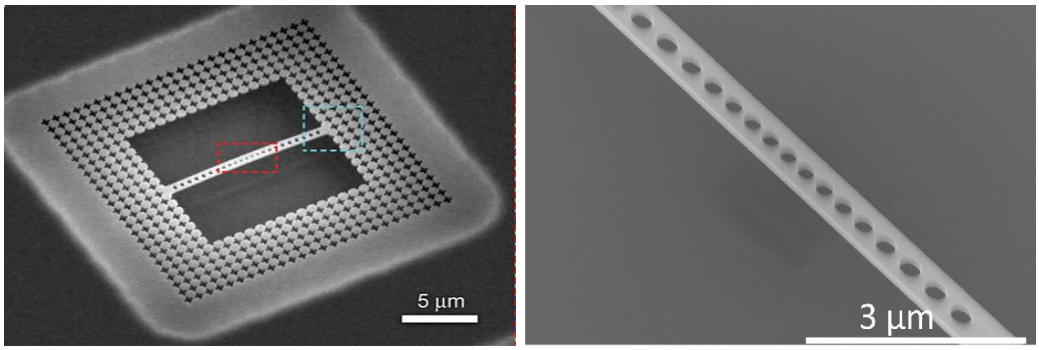

(a) (b)

Figure 1.2: (a) Scanning electron microscope image of PhC nanobeam surrounded by a phononic shield [Chan et al., 2011]. (b) GaP PhC nanobeam with $g_0/2\pi \sim$ 400 kHz [Schneider et al., 2017]. All figures are adapted from the corresponding references.

The miniaturization of mechanical resonators has led to achieving $g_0 \sim$ MHz. For example, PhC nanobeams as shown in Fig. 1.2b have low mass $\sim$ pg which pushes their g_0 to large values in the MHz range [Schneider et al., 2017]. However, it remains a huge challenge to achieve low optical losses, and strong coupling strengths on chip simultaneously. State of the art devices have a ratio $g_0/\kappa \sim 10^{-2}$ for on-chip optomechanical systems [Chan et al., 2011], which is two orders of magnitude lower than the desired value.

1.2 Multi-element optomechanics

One of the approaches to realize high g_0 value without compromising κ is the so-called membrane in the middle approach, in which a mechanical element is placed in the middle of a Fabry-Pérot cavity. This approach has the advantage of decoupling the mechanical design from the optical one. Therefore, it is possible to fabricate high Q_m and low mass resonators, and at the same time, use a high finesse optical cavity [Marquardt and Girvin, 2009]. For the membrane in the middle case, g_0 is linearly proportional to the reflectivity of the mechanical membrane; i.e maximized for a large reflectivity element [Xuereb et al., 2012]. This approach could be extended to using multiple mechanical resonators instead of the single resonator case.

There has been strong interest in studying collective optomechanical interactions between multiple mechanical resonators and electromagnetic fields [Chang et al., 2011; Heinrich et al., 2011]. Xuereb *et al* theoretically investigated the possibility of exploiting such multi-element approach to push the coupling strength to the strong coupling regime [Xuereb et al., 2012]. Fig. 1.3a shows a generic system of N mechanical scatterers with Reflectivity $R = 0.2$ placed in a Fabry-Pérot cavity of length L. Fig. 1.3c shows that according to the separation d between these elements,

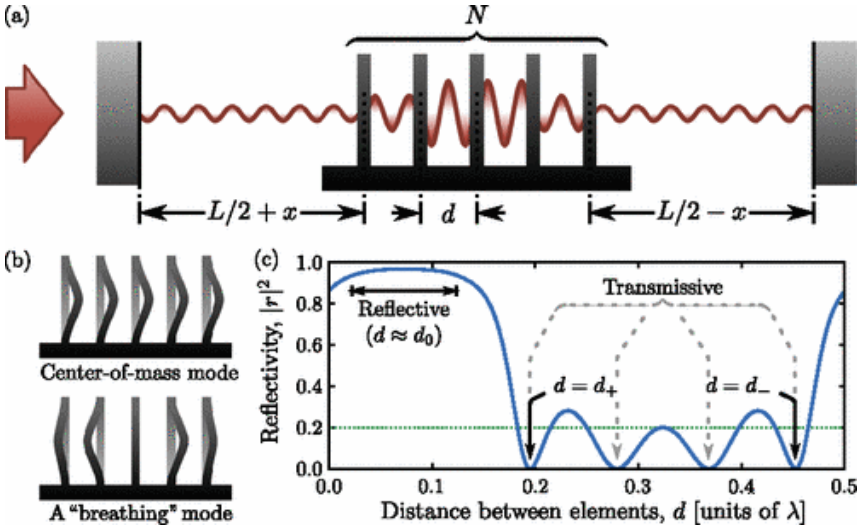

Figure 1.3: A Schematic of the multi-element optomechanical system, mechanical modes, and working points. (a) A general schematic of N scatterers separated by a distance d in the middle of a Fabry-Pérot cavity of length L. (b) Examples of super-element collective motional modes. (c) Reflectivity of an array of 5 scatterers as a function of distance separating the elements d, while each element has a reflectivity of 0.2 as shown in green [Xuereb et al., 2012].

it is possible to operate in either a reflective regime where $R \approx 1$, or in a transmissive regime where $R = 0$. In case of operating at the transmissive points, electromagnetic radiation couples to the collective motional modes as the ones shown in Fig. 1.3b, which could potentially lead to enhanced optomechanical coupling strength.

Fig. 1.4 shows the coupling strength for the multi-element case normalized by the single element case as a function of single element reflectivity. By inspection, we observe that depending on the motional mode the radiation couples to, the coupling strength changes dramatically. For example, coupling to sinusoidal modes gives an enhancement, while coupling to the center of mass mode leads to deterioration in coupling strength. Moreover, there is a strong dependence on the reflectivity of individual elements in the stack, the higher the reflectivity the stronger the enhancement in g_0, which can be orders of magnitude more than the single element case. We can also conclude that in case of using only 2 elements, it is possible to get highly enhanced coupling if the condition of achieving high reflectivities approaching unity for each element is met [Xuereb et al., 2013].

Several experimental research groups adopted the approach of multi-element optomechanics in the attempt to reach the single-photon strong coupling regime. Many groups relied on tensile strained silicon nitride (SiN) nanomembranes deposited on silicon (Si) substrate. SiN is a material with excellent mechanical properties showing Q_m exceeding 10^6 by means of strain engineering, and when placed in a high finesse optical cavity, SiN membrane systems show excellent optomechanical properties [Thompson et al., 2008].

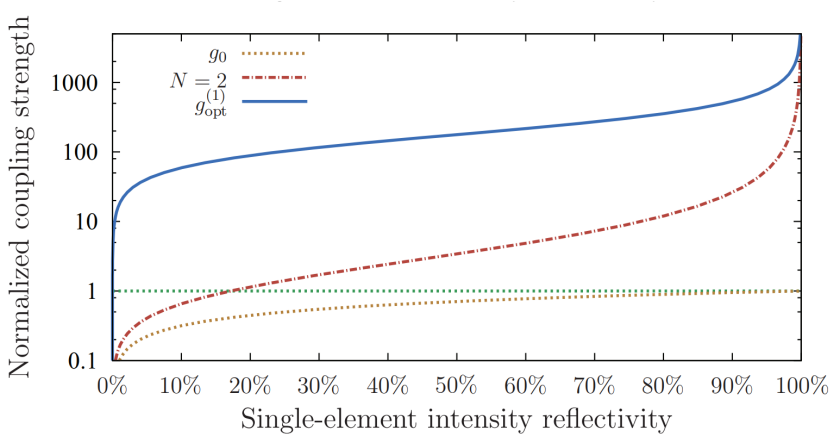

Figure 1.4: The coupling strength of a sinusoidal mode with an optimal element number N (dark blue curve) and for $N = 2$ (dashed-dotted orange). The coupling strength for the center of mass mode is shown (dotted orange). All curves are normalized by g_0 of the single element curve (dotted green). Figure is adapted from the corresponding reference [Xuereb et al., 2013].

Nair *et al* studied stacks of 100 nm thin tensile stressed ($\sim$ 1 GPa) SiN double membrane devices having spacing varying from 8.5 μm to 200 μm both optically and mechanically. They demonstrated excellent $Q_m > 10^6$ and showing peak optical transmission $\sim$ 99.7% [Nair et al., 2017]. Piergentili *et al* studied a two membrane SiN system and demonstrated the possibility to tune the optomechanical coupling by varying the membrane separation, achieving a maximum gain of $\sim$ 2.47 compared to the single membrane case [Piergentili et al., 2018]. Gärtner *et al* fabricated and characterized fully integrated stacks of SiN single and double membrane devices of multiple reflectivites. The reflectivity of the stack was changed by adding PhC patterns of different parameters, where they verified the enhanced optomechanical coupling for the high reflectivity double membrane stacks [Gärtner et al., 2018].

1.3 Multi-element optomechanics with AlGaAs heterostructures

Despite the current progress in multi-element optomechanics using SiN nanomembranes, the approach is inherently limited, as SiN is not a crystalline material which is usually deposited on Si wafer using chemical vapor deposition. As a result, it is not possible to grow multiple layers with high quality on one side of the wafer. The current progress in the multi-element approach using SiN makes use of the idea of depositing another layer on the backside of the Si wafer, and then etch the Si in between the membranes. Clearly, the approach has many constraints considering layer thicknesses and alignment. In [Nair et al., 2017] for example, custom made spacers were used to study various stack thickness.

The proposed approach in our group is to take advantage of molecular beam epitaxy, which is capable of growing III-V material heterostructures of sub-nanometer precision. This allows a versatile approach to make multi-element membranes with customized thickness and separation in a simple and reproducible manner. The material system of choice is GaAs/AlGaAs heterostructures which can be grown lattice matched minimzing the surface defects which could severely affect the mechanical performance. Moreover, it allows simple fabrication procedure in the cleanroom as AlGaAs can be sacrificially etched by hydrofluoric acid (HF), giving free standing GaAs membranes. To engineer the reflectivity of GaAs membranes, an approach similar to [Gärtner et al., 2018] is used, where PhC patterns are designed to tune the reflectivity of individual mechanical elements. A topic which is discussed in section 2.4.

1.4 Thesis organization

This thesis aims to characterize PhC-patterned and non-patterned GaAs membranes. Both optical and mechanical properties are of interest. Mechanical characterization of membrane Q_m is of primary importance, as Q_m is an important figure of merit in cavity optomechanics, and high Q_m is needed for cooling the mechanical resonator to the quantum mechanical ground state. Moreover, a mode tomography technique is implemented to relate the mechanical eigenmodes in simulations to experiment. Optical reflectivity measurements aim to study the peak reflectivity of PhC-patterned membranes, and simulations are done to have a better understanding and prediction of the measured spectrum.

Chapter 2 focuses on the theory of mechanical membranes, harmonic oscillators, Fabry-Pérot cavities and PhC slabs. It includes the derivation of the main equations which relate theory to experiments which is at the heart of this thesis. Moreover, Gaussian beam decomposition into plane waves will be discussed which is important to model the interaction of Gaussian beams with PhC slabs.

Chapter 3 discusses the experimental methods used in this thesis. *Homodyne detection* system used to probe mechanical modes will be explained. It also includes the process of automation of Q_m measurement procedure, and developing mode tomography technique to experimentally identify different mechanical modes. The setup for characterizing optical reflectivity will be discussed in detail as well.

Chapter 4 is concerned with the results. It systematically studies performance of GaAs membranes in regard to their eigenfrequencies ω_m and Q_m. It also compares COMSOL simulations to the experimental findings of ω_m of different mechanical modes. Finally, it discusses optical reflectivity measurements of various PhC patterns on GaAs membranes and compares them to simulations.

Chapter 5 gives a brief conclusion to the main findings of the thesis, and an outlook for future research.

2

Theory

This chapter introduces the theoretical background necessary for this thesis. Firstly, the theory of vibrational modes of mechanical membranes is introduced and the noise power spectrum is derived from the relevant physical parameters. Secondly, the theory of Fabry-Pérot cavity is explained and the main physical parameters of an optical cavity are defined. Combining the quantum mechanical Hamiltonian of the mechanical and the optical part allows us to derive the optomechanical Hamiltonian from simple arguments. Moreover, the theory of Fano resonance in PhC slabs is introduced to explain how these structures can be designed for broadband reflection. Finally, the decomposition of Gaussian beams into plane waves will be discussed.

2.1 Mechanical modes of nanomembranes

A thin plate is a flat mechanical object bounded by two parallel planes. The distance separating the two planes is referred to as the thickness h, which is small compared to other characteristic dimensions of the structure such as the length L and the width W as shown in Fig. 2.1. Membranes are thin plates which have a ratio $\frac{a}{h} >$ 80...100, where a is the typical plate dimension [Ventsel and Krauthammer, 2001]. Since the structures under investigation in this thesis have $\frac{a}{h} > 400$ and $h = 100$ nm, they are classified as nano-membranes. In this section, the basic approach to derive mechanical modes from the wave equation is introduced. Then, finite element method (FEM) is discussed as means to simulate the eigenmodes for more complex geometries. Finally, I introduce the classical harmonic oscillator model and the main physical parameters of a mechanical resonator which are highly relevant for the interpretation of the mechanical characterization experiments.

2.1.1 Mechanical vibrational modes

The vibrational modes of a rectangular plate can be derived by solving the wave equation in rectangular coordinates x and y as defined in Fig. 2.1:

$$\frac{\partial^2 z}{\partial x^2} + \frac{\partial^2 z}{\partial y^2} = \frac{1}{v^2}\frac{\partial^2 z}{\partial t^2}, \tag{2.1}$$

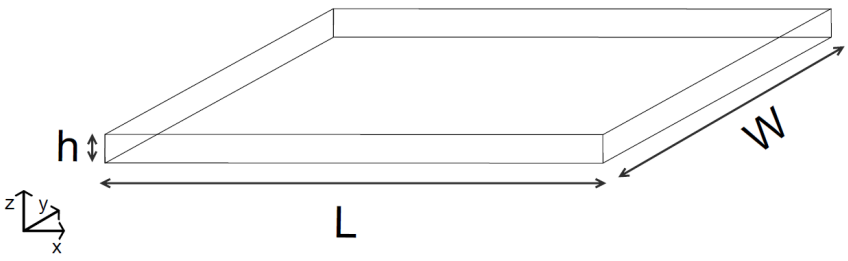

Figure 2.1: Geometry of a thin plate showing the characteristic dimensions: length L, width W and thickness h.

v is the speed of sound in the medium, which is given by:

$$v = \sqrt{\frac{E}{\rho}} \tag{2.2}$$

where E is Young's modulus, and ρ is the material density. If the boundary conditions are set to be zero displacement at the boundary and the partial differential equation (PDE) is solved, we get the following eigenfrequencies [Rasmussen, 2013]:

$$\omega_{mn} = v\pi\sqrt{\left(\frac{m}{L_x}\right)^2 + \left(\frac{n}{L_y}\right)^2}, \tag{2.3}$$

and the eigenmodes:

$$z_{mn}(x, y, t) = (A_{mn}\cos\omega_{mn}t + B_{mn}\sin\omega_{mn}t)\sin\left(\frac{m\pi x}{L_x}\right)\sin\left(\frac{n\pi y}{L_y}\right), \tag{2.4}$$

where A_{mn} and B_{mn} are coefficients which depend on the initial conditions. The eigenmodes are parametrized by integers m and n, which correspond to the number of nodes - 1 in the x and y directions, respectively. Fig. 2.2 shows the first 4 eigenmodes according to eqn 2.4. It can be observed that as the frequency increases the number of nodes increases. Any excitation of the membrane can be analyzed as linear combination of its eigenmodes.

2.1.2 FEM simulations

For complex geometries, analytic solutions do not exist. It is necessary to rely on numerical techniques and simulations to estimate the eigenmodes of such structures and compare them to measurements. FEM is an extremely powerful tool to analyze these modes. COMSOL multiphysics is a commercial FEM solver which gives the capability to combine different physics modules to analyze complex physical problems. For the task of finding the eigenmodes of a mechanical structure, COMSOL offers the possibility to do frequency domain analysis. The eigenmodes are always ordered in terms of increasing energy, which is helpful as it saves computational time if one is mainly interested in low order modes [Rasmussen, 2013].

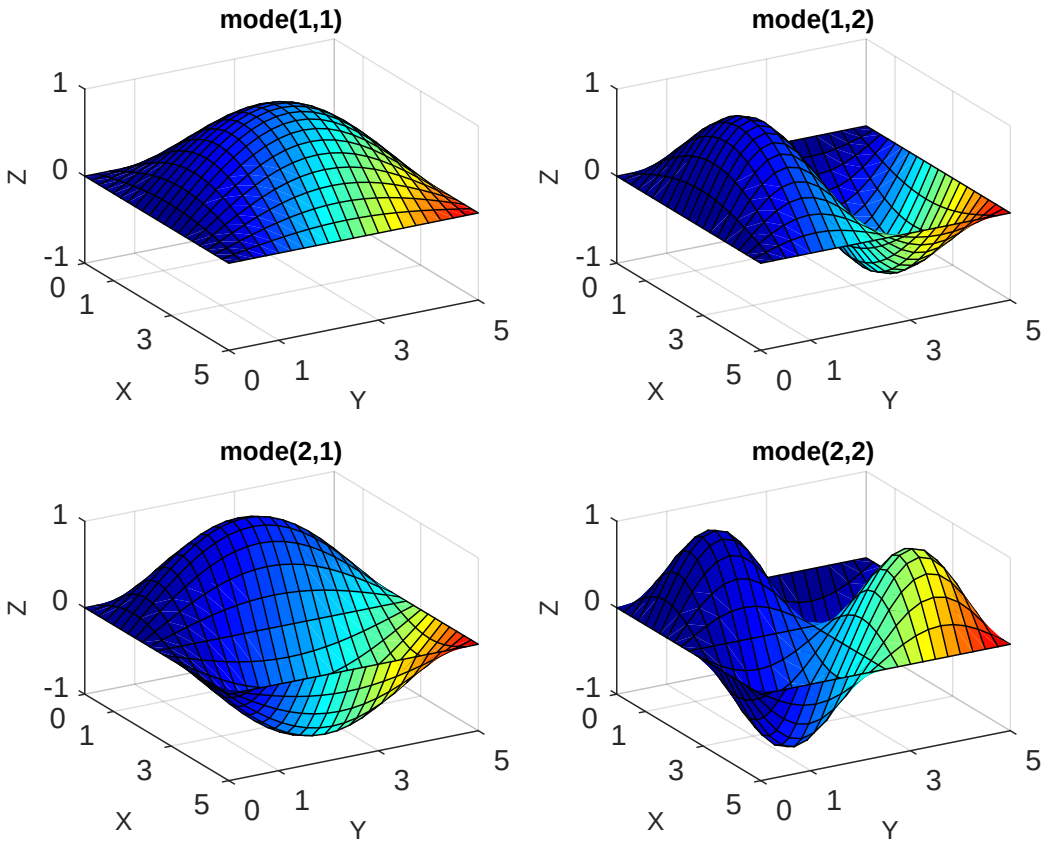

Figure 2.2: The first 4 mechanical modes of a membrane according to eqn 2.4. Figure is reproduced from [Rasmussen, 2013].

2.1.3 The classical harmonic oscillator

The classical mechanical harmonic oscillator is a standard problem in introductory physics textbooks, which I will not discuss in detail. However, the main important results will be derived as they are highly relevant to the characterization of mechanical membranes. The theoretical explanation I discuss relies on the one given in [Gröblacher, 2012].

Various physical systems give the behaviour of a harmonic oscillator. Typical examples are the pendulum and guitar string. The physical concept is having repetitive oscillations around a reference position due to a restoring force which is proportional to the displacement from this reference position. If the system is coupled to the environment, which is usually the case, then a damping term is added to the differential equation (DE) to account for dissipation. As a result, the DE for the position $x(t)$ reads:

$$\frac{dx^2(t)}{dt^2} + \gamma_m \frac{dx(t)}{dt} + \omega_m^2 x(t) = 0, \tag{2.5}$$

where γ_m is the damping rate and is assumed to be frequency independent and ω_m is the eigenfrequency:

$$\omega_m = \sqrt{\frac{k}{m}}, \tag{2.6}$$

where k is the spring constant. The solution to the DE is straightforward and is given by:

$$x(t) = A_d \exp\left(-\frac{\gamma_m t}{2}\right) \sin\Big(\sqrt{\omega_m^2 - \Big(\frac{\gamma_m}{2}\Big)^2}\, t + \phi_d\Big). \tag{2.7}$$

The solution is a sinusoidal function oscillating at a frequency $\omega_d = \omega_m^2 - (\frac{\gamma_m}{2})^2$, with an exponentially decaying envelope function at a rate $\frac{\gamma_m}{2}$. The Amplitude A_d and the phase ϕ_d are given by the initial conditions. An extremely important parameter to characterize damped mechanical oscillators is the quality factor Q_m, which gives the number of cycles the oscillator undergoes before the amplitude decays to $1/e$ its initial value. Q_m is defined as:

$$Q_m := \frac{\omega_m}{\gamma_m}. \tag{2.8}$$

The discussed solution is for the so-called unforced oscillation, but often harmonic oscillators are coupled to an external bath which drives their motion. The DE which describes the system reads:

$$\frac{dx^2(t)}{dt^2} + \gamma_m \frac{dx(t)}{dt} + \omega_m^2 x(t) = \frac{F(t)}{m}. \tag{2.9}$$

where $F(t)$ is the external driving force which can have any arbitrary form. Eqn 2.9 is more conveniently solved in Fourier space, by introducing the Fourier transform $x(\omega) = \int_{-\infty}^{\infty} x(t) e^{i\omega t} dt$. The solution of $x(t)$ in Fourier space is:

$$x(\omega) = \frac{F(\omega)}{m} \frac{1}{\omega_m^2 - \omega^2 + i\omega\gamma_m}, \tag{2.10}$$

where $F(\omega)$ is the Fourier transform of the driving force. A common case is when the harmonic oscillator is coupled to a thermal bath at a temperature T, the bath can be described as an infinite sum over harmonic oscillators exerting a total force $F_{tot}(t)$. The noise power spectral density (PSD) $S_{xx}(\omega)$, which is a measure for the signal power distribution for different frequency components is given by:

$$S_{xx}(\omega) = \frac{F_{tot}(\omega)}{m^2} \frac{1}{(\omega_m^2 - \omega^2)^2 + \omega^2\gamma_m^2}. \tag{2.11}$$

This expression can be approximated if we assume $Q_m \gg 1$, then in the vicinity of the response maximum $\omega \approx \omega_m$, $S_{xx}(\omega)$ can be approximated by a Lorentzian

function using the identity $(\omega_m^2-\omega^2) = (\omega_m-\omega)(\omega_m+\omega) \approx 2(\omega_m-\omega)\omega_m$ [Aspelmeyer et al., 2014]. Then, the expression for $S_{xx}(\omega)$ becomes:

$$S_{xx}(\omega) = \frac{F_{tot}(\omega)}{4m^2\omega_m^2}\frac{1}{(\omega_m-\omega)^2+(\frac{\gamma_m}{2})^2}. \tag{2.12}$$

The Fourier transform of the autocorrelation function can be connected to $S_{xx}(\omega)$ through the Wiener-Khinchin theorem which is applicable for a random variable with a constant mean [Gröblacher, 2012]:

$$S_{xx}(\omega) = \int_{-\infty}^{\infty} \langle x(t)x^*(t-\tau)\rangle e^{-i\omega\tau} d\tau, \tag{2.13}$$

if we set $\tau = 0$:

$$\langle x^2\rangle = \int_{-\infty}^{\infty} \frac{S_{xx}(\omega)}{2\pi} d\omega = \frac{F_{tot}}{2m^2}\frac{1}{\omega_m^2\gamma_m}. \tag{2.14}$$

This leads to an extremely important result, that the variance of the mechanical displacement is proportional to the area under the experimentally measured $S_{xx}(\omega)$. Here we can notice a difference in the definition between references [Gröblacher, 2012] and [Aspelmeyer et al., 2014] by a factor of 2π, I opted for the latter definition which is the correct one.

In the weak damping limit, equipartition theorem states that each degree of freedom contributes $\frac{1}{2}k_BT$. Therefore, for a 1D harmonic oscillator, the kinetic energy E_k and potential energy E_p contribute equally to a total Energy $E_{tot} = k_BT$, where k_B is Boltzmann constant and T is the temperature of the oscillator. Since $E_p = \frac{1}{2}m\omega_m^2\langle x^2\rangle = \frac{1}{2}k_BT$, and using eqn 2.14 to plug the expression for F_{tot} in eqn 2.12, $S_{xx}(\omega)$ reads:

$$S_{xx}(\omega) = \frac{\gamma_m k_B T}{2m\omega_m^2}\frac{1}{(\omega_m-\omega)^2+(\frac{\gamma_m}{2})^2}. \tag{2.15}$$

We can observe that a damped mechanical oscillator driven by the Brownian noise of a thermal force gives a Lorentzian-like function in Fourier space with resonance frequency ω_m and full width at half maximum (FWHM) γ_m. This expression is extremely important for experimentally extracting γ_m to calculate Q_m for our GaAs membranes.

2.1.4 The quantum harmonic oscillator

To reach the quantum optomechanical hamiltonian, one needs to quantize the mechanical harmonic oscillator, which is a standard problem in any quantum mechanics textbook. Following the procedure of canonical quantization, one arrives at the quantum mechanical Hamiltonian [Aspelmeyer et al., 2014]:

$$\hat{H} = \hbar\omega_m\hat{b}^\dagger\hat{b} + \frac{1}{2}\hbar\omega_m, \tag{2.16}$$

where $\hat{b}^\dagger$ and $\hat{b}$ are the phonon creation and annihlation operators, respectively. the position and momentum operators $\hat{x}$ and $\hat{p}$ can be written as:

$$\hat{x} = x_{ZPF}(\hat{b} + \hat{b}^\dagger), \tag{2.17}$$

$$\hat{p} = -im\omega_m x_{ZPF}(\hat{b} - \hat{b}^\dagger), \tag{2.18}$$

where

$$x_{ZPF} = \sqrt{\frac{\hbar}{2m\omega_m}} \tag{2.19}$$

is the zero point fluctuation of the quantum mechanical oscillator.

2.2 Optical cavities

As discussed in the introduction, cavity optomechanics investigates the interaction between modes of a mechanical resonator and modes of an optical cavity. Having discussed the basics of mechanical resonators; in this section the fundamentals of optical resonators are discussed and the main physical parameters are derived. The explanation is inspired by the one given in [Saleh and Teich, 2007].

There are many possible experimental realizations for an optical resonator. The simplest resonator is the Fabry-Pérot resonator as schematically shown in Fig. 2.3, which is realized by having two partially transmissive mirrors separated by a distance L. The optical path length for a round trip should be a multiple of 2π,

$$\phi = 2kL = m2\pi, m = 1, 2, 3... \tag{2.20}$$

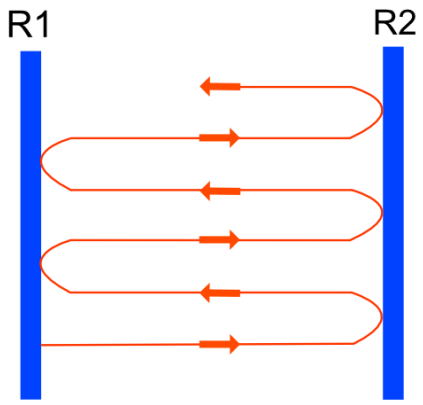

Figure 2.3: Schematic of a Fabry-Pérot resonator composed of a cavity of length L and two partially reflective mirrors with intensity reflectivity R1 and R2, respectively.

where k is the wavevector. This condition imposes certain frequencies at which cavity resonance occurs, these frequencies are:

$$\nu_{cav} = m\frac{c}{2L}. \tag{2.21}$$

The separation between two different longitudinal modes is referred to as the free spectral range (FSR) of the cavity and is given by:

$$\Delta\nu_{FSR} = \frac{c}{2L}. \tag{2.22}$$

An important parameter which characterizes an optical resonator is the finesse $\mathcal{F}$, which is effectively the number of round trips done by the photon before exiting the cavity. High $\mathcal{F}$ optical cavities can have $\mathcal{F} > 10^6$ [Rempe et al., 1992]. $\mathcal{F}$ is related to the round trip loss $|r|$ of the optical cavity and is given by [Saleh and Teich, 2007]:

$$\mathcal{F} = \frac{\pi\sqrt{|r|}}{1-|r|}, \tag{2.23}$$

where

$$|r|^2 = R_1 R_2, \tag{2.24}$$

R_1 and R_2 are the intensity reflectivities of the two mirrors. The distributed losses inside the cavity are neglected in such treatment which is realistic if the resonator medium is air.

Assuming an input wave with a certain intensity, we can derive the transmittance of the optical cavity as the ratio of output to input intensity ($\frac{I_{out}}{I_{in}}$). This is a standard exercise in any introductory optics textbook, and the final result is [Saleh and Teich, 2007]:

$$T = \frac{(1-R_1)(1-R_2)}{(1-\sqrt{R_1R_2})^2 + 4\sqrt{R_1R_2}\sin\theta}, \tag{2.25}$$

where

$$\theta = kL = \frac{2\pi\nu L}{c}. \tag{2.26}$$

We can observe that as the reflectivity of the mirror increases, $\mathcal{F}$ increases leading to sharper resonance peaks as shown in Fig. 2.4. If we assume $\mathcal{F} \gg 1$, then the FWHM of the optical resonator is:

$$\delta\nu \approx \frac{\Delta\nu_{FSR}}{\mathcal{F}}. \tag{2.27}$$

Achieving low loss optical cavities is a primary concern for the field of cavity optomechanics. Furthermore, this physical situation will be encountered in optical reflectivity measurements of single membrane devices.

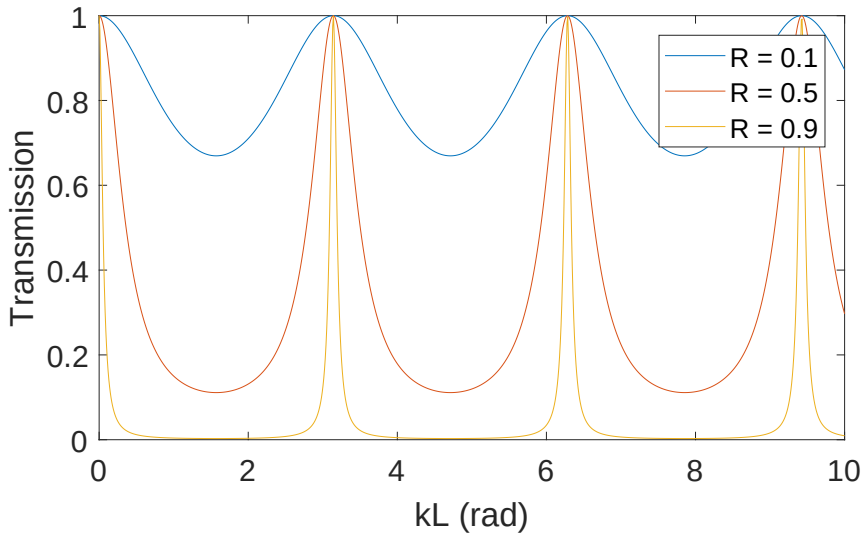

Figure 2.4: Transmission spectrum of a Fabry-Pérot cavity for different mirror reflectivety according to eqn 2.25.

2.3 The optomechanical Hamiltonian

In this section, the optomechanical Hamiltonian will be dervied from semi-classical arguments for the simple system shown in Fig. 1.1, and then generalized to the quantum mechanical Hamiltonian. This will lead us to derive the single-photon optomechanical coupling strength g_0 from simple assumptions.

In section 2.2, the resonance modes of a Fabry-Pérot cavity are derived; the cavity resonance frequencies are $\nu_{cav} = \frac{mc}{2L}$, where c is the speed of light and L is the length of the cavity and m is a positive integer. If we assume the force exerted by photons shift the cavity length by δ_x, then the new cavity resonance frequency becomes:

$$\nu' = \frac{mc}{2(L + \delta_x)}, \tag{2.28}$$

which can be rearranged as:

$$\nu' = \frac{mc}{2L(1 + \frac{\delta_x}{L})}. \tag{2.29}$$

Since $\delta_x \ll L$, we Taylor expand around L; keeping the linear term we get:

$$\nu' \approx \frac{mc(1 - \frac{\delta_x}{L})}{2L} = \nu\Big(1 - \frac{\delta_x}{L}\Big). \tag{2.30}$$

This simple model shows that optomechanical coupling leads to a linear shift in ν for small mirror displacements. An approximation which is valid for the vast majority of cavity optomechanics experiments [Rasmussen, 2013].

To move to the quantum mechanical picture, we first use the Hamiltonian of the coupled optomechanical system which reads:

$$\hat{H} = \hbar\omega'_{cav}(x)\hat{a}^\dagger\hat{a} + \hbar\omega_m\hat{b}^\dagger\hat{b}, \tag{2.31}$$

where $\hat{a}^\dagger$ and $\hat{a}$ are the photon creation and annihilation operators respectively, while $\hat{b}^\dagger$ and $\hat{b}$ are the phonon creation and annihilation operator of the mechanical mode. ω'_{cav} is the shifted optical cavity resonance frequency due to optomechanical coupling ($\omega'_{cav} = 2\pi\nu'_{cav}$), and ω_m is the mechanical mode resonance frequency. Now we make use of the result of eqn 2.30 for a small cavity shift $\delta_x \ll L$ to reach the optomechanical Hamiltonian [Rasmussen, 2013]:

$$\hat{H} = \hbar\omega_{cav}\Big(1 - \frac{\delta_x}{L}\Big)\hat{a}^\dagger\hat{a} + \hbar\omega_m\hat{b}^\dagger\hat{b}. \tag{2.32}$$

Next, we can promote the mirror displacement δ_x to the quantum mechanical position operator $\hat{x}$. Moreover, we define $G = \omega_{cav}/L$ which describes the change in cavity resonance with position [Aspelmeyer et al., 2014]. Therefore, the quantum mechanical Hamiltonian reads:

$$\hat{H} = \hbar(\omega_{cav} - G\hat{x})\hat{a}^\dagger\hat{a} + \hbar\omega_m\hat{b}^\dagger\hat{b}. \tag{2.33}$$

From the quantization of the quantum mechanical harmonic oscillator described in section 2.1.3, we make use of the definition of position operator in terms of the phononic creation and annihilation operators $\hat{x} = x_{ZPF}(\hat{b} + \hat{b}^\dagger)$ to reach the interaction part of the Hamiltonian:

$$\hat{H}_{int} = -\hbar g_0\hat{a}^\dagger\hat{a}(\hat{b}^\dagger + \hat{b}), \tag{2.34}$$

where

$$g_0 = Gx_{ZPF}. \tag{2.35}$$

g_0 is the single-photon optomechanical coupling strength which is one of the most fundamental physical parameters in the field of cavity optomechanics. It captures the coupling strength between a single photon and a single phonon [Aspelmeyer et al., 2014]. One can intuitively interpret $\hat{H}_{int}$ by observing that the photon number operator $\hat{a}^\dagger\hat{a}$ couples to the position operator of the mechanical oscillator $\hat{x}$. Moreover, $\hat{H}_{int}$ is inherently nonlinear, as it is cubic in field operators. However, most of the state of the art experiments in cavity optomechanics can be understood using a linearized version of the Hamiltonian.

2.4 Photonic crystals

Photonic crystals are "*periodic arrays of dielectric scatterers in homogeneous dielectric matrices*" [Joannopoulos et al., 1997]. As a consequence of such periodicity,

PhCs form photonic bandgaps in analogy to the energy bandgap in semiconductors. In other words, certain light frequencies can not propagate through such material, which offers an extremely exciting way to manipulate light. In this section, the physics of light confinement in PhC slabs will be discussed. This will lead us to explore the phenomenon of Fano resonance in PhC slabs, which can be tailored to engineer the slab with certain functionality. For example, it can be used to design broadband reflectors which are relevant to maximize the radiation pressure force. Even more, such slabs could help reach the single-photon strong coupling regime using the multi-element optomechanics approach.

2.4.1 Photonic crystal slabs

2D PhC slabs are an important class of PhCs. A PhC slab is a quasi-3D structure which offers in-plane confinement due to the presence of an in-plane photonic band gap. Moreover, refractive index confinement through total internal reflection takes place in the vertical direction. As an illustration, we investigate one of the most commonly studied PhC slab structures in the literature, which is the triangular lattice PhC slab with air columns. Fig. 2.5 shows a schematic of a PhC slab with thickness h, and with a triangular lattice pattern. The PhC pattern is defined by 2 parameters: the hole radius r and the lattice period a. Fig. 2.5b shows the photonic band diagram. The frequency is normalized by a due to the scale invariance property of Maxwell's equations. The band diagram is given for both TE-polarization, defined when the electric field is in the xy plane and the magnetic field is in the z-direction, and TM-polarization, defined when the magnetic field is in the xy plane and the electric field is in the z-direction. We can see that this structure gives a complete photonic bandgap for both TE and TM polarization. Moreover, we can notice the light cone formed due to vertical confinement. All modes below the light-line, defined as the boundary of the shaded region, are in-plane guided modes and they do not couple to external radiation. On the other hand, the modes above the light-line can radiate in the air. We refer to these modes as guided resonances [Zhou et al., 2014].

2.4.2 Fano resonance

Due to total internal reflection, the guided modes below the light-line do not couple to external radiation and have their energy highly confined in the slab. Thus, they have an infinite lifetime. On the other hand, guided resonances are the modes located above the light-line. Similar to the guided modes, guided resonances have their electromagnetic energy confined in the slab. However, since they are above the light-line, they can couple to external radiation providing an efficient pathway to couple to the environment, and thus, have a finite lifetime [Fan and Joannopoulos, 2002]. As seen in Fig. 2.6, if we assume light is Incident from an out of plane direction on the PhC slab, then light can interact in two different ways: a direct pathway through the PhC slab without coupling to the guided resonances, and an

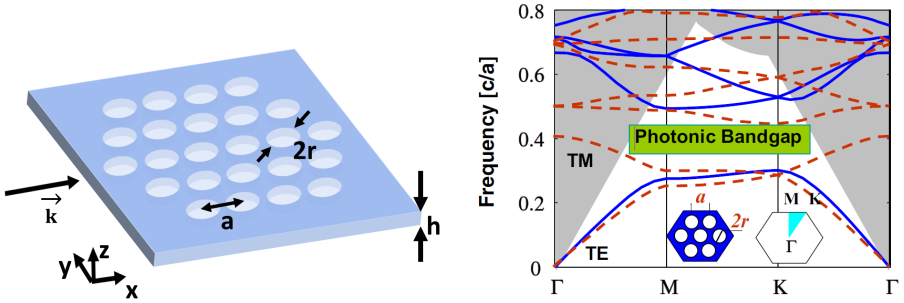

(a) (b)

Figure 2.5: (a) A schematic of PhC slab with triangular lattice. (b) Photonic band diagram for the simulated structure. The left inset shows the triangular lattice structure with parameters r and a. The right inset shows the 1st Brillouin zone. Γ, M and K are the high symmetry points which form the irreducible zone. All figures are adapted from the corresponding references [Zhou et al., 2014].

indirect pathway by coupling to the guided resonance mode and then leaking to free space. Interference can occur between these two pathways leading to the so-called Fano resonance phenomenon, which is characterized by its asymmetric lineshape, the transmission and reflection amplitude can be expressed as follows [Fan and Joannopoulos, 2002]:

$$t = t_d + f\frac{\gamma}{i(\omega - \omega_0) + \gamma}, \tag{2.36}$$

$$r = r_d \pm f\frac{\gamma}{i(\omega - \omega_0) + \gamma}, \tag{2.37}$$

where t_d and r_d are the direct reflection and transmission coefficients. ω_0 and γ are the resonance frequency and linewidth of the guided resonance, respectively. f is the normalized complex amplitude of the guided resonance mode, and the plus/minus sign is for even/odd symmetry of modes. Even/odd symmetry is defined with respect to the mirror plane parallel to the slab. Fano resonance properties of PhC slabs can be used to design optical filters, for which high quality factors are desirable. Moreover, broadband reflectors can be designed which give $R \approx 1$ for a wide wavelength range which is of interest in this thesis.

2.4.3 2D photonic crystal reflectors

As explained in the introduction, realization of membranes with $R \approx 1$ at normal incidence is an important condition to reach the single-photon strong coupling regime. The process of designing a PhC slab to act as a broadband reflector is mostly a trial-and-error approach using computational techniques. Usually large r/a values (~ 0.4) favor broadband reflectors, while small r/a values (~ 0.1) work

for high optical quality factor filters [Zhou et al., 2014]. To achieve high reflectivity for our GaAs membranes, the chosen lattice structure is a square lattice shown in Fig. 2.6. Square lattices possess a 90° rotational symmetry. This makes the reflectivity of the lattice polarization insensitive, which is a highly desirable property for our broadband reflector [Yang et al., 2011]. High reflectivity broadband reflectors have been demonstrated with square lattice PhC patterns. For example, $R > 99.8\%$ was reported with square lattice in an InP PhC slab at wavelength $\lambda = 1064$ nm [Makles et al., 2015]. Our design of PhC slab to achieve high reflectivity is discussed in section 4.2.1.

Since the discontinuities in the dielectric permittivity $\epsilon(r)$ prevents an analytic solution to Maxwell's equations, numerical techniques have to be used. There are different approaches to simulate such structure. The techniques are generally classified into either time-domain (TD) approaches such as Finite Difference Time Domain (FDTD), or frequency domain (FD) approaches [Tsvirkun, 2015]. Two of the most prominent FD approaches are FEM simulations, and rigorous coupled wave analysis (RCWA). RCWA solves Maxwell's equations in Fourier space, and is particularly useful for periodic structures. Recently, a free software package was developed by Liu and Fan, and is now available as Stanford Stratified Structure Solver (S^4) [Liu and Fan, 2012], which can be used online through nanohub.com. The package combines RCWA with the scattering matrix formalism ensuring high resolution and short computation time. The software deals with periodic structures as seen in Fig. 2.6 as infinite in xy plane by defining a unit cell and using Bloch Boundary conditions. While for the propagation direction, the relative permittivity ϵ of each layer is the relevant physical value. The software gives the final result of reflection and transmission spectra normalized by the incident wave for the first and last layer of the multi-layer structure.

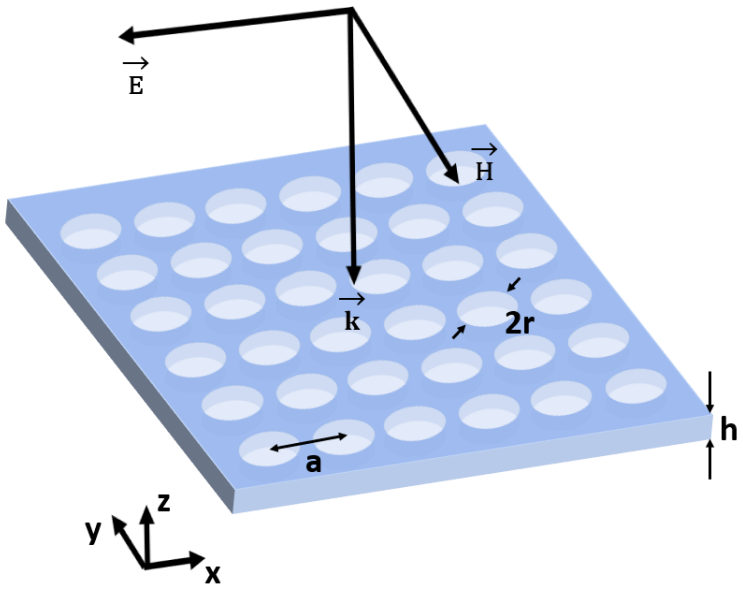

Figure 2.6: Schematic of a PhC slab with a square lattice.

2.5 Gaussian beams

In the design of the optical setups used in experiments throughout this thesis, laser beams travel in free space and pass through multiple optical components altering the beam properties. In order to design our experiments and interpret the results, a proper model is needed which can accurately describe laser beam properties. Although monochromatic plane waves are the simplest solution to the *Helmholtz equation*, but they fail to properly model laser beams, as their amplitude extends to infinity in the transverse direction and they do not diverge. On the other hand, laser beams are spatially collimated, and have some divergence in the propagation direction. Gaussian beams show these properties and hence, can properly model laser beams. Gaussian beams can be obtained by solving the *paraxial Helmholtz equation*, which is a standard derivation in optics textbooks (for example: [Saleh and Teich, 2007]).

2.5.1 Properties of Gaussian beams

If we assume a Gaussian beam propagating in the z-direction, it can be uniquely described by 2 parameters: the wavelength λ and the Rayleigh range z_0. The beam size $w(z)$ is defined as [Saleh and Teich, 2007]:

$$w(z) = w_0 \sqrt{1 + \left(\frac{z}{z_0}\right)^2}, \tag{2.38}$$

where w_0 is the beam waist, which is the minimum value for the beam size, as shown at $z = 0$ in Fig. 2.7. The expression for w_0 is:

$$w_0 = \sqrt{\frac{\lambda z_0}{\pi}}. \tag{2.39}$$

On the other hand, z_0 is the position at which the $w(z) = \sqrt{2} w_0$ - marked by red lines in Fig. 2.7 -. Thus, z_0 is a measure of the divergence of a Gaussian beam. The larger z_0 is, the longer the distance the beam covers while remaining focused. Considering the wavefronts - the planes of constant phase - which are marked by the blue lines, we can observe that they are planar at the position of w_0, but the radius of curvature increases by increasing z. One can immediately see that for a fixed λ, w_0 is proportional to $\sqrt{z_0}$. Thus, if the beam is required to be collimated for a large distance, then a large z_0 is needed which directly translates to a large w_0. In other words, it is not possible to have a highly focused beam which is collimated for long distances at the same time.

In free space optical setups, it is desirable to use a highly collimated laser beam which passes by multiple optical elements. Finally, it is focused by a lens with focal length f on the device of interest. Focusing a collimated Gaussian beam having a

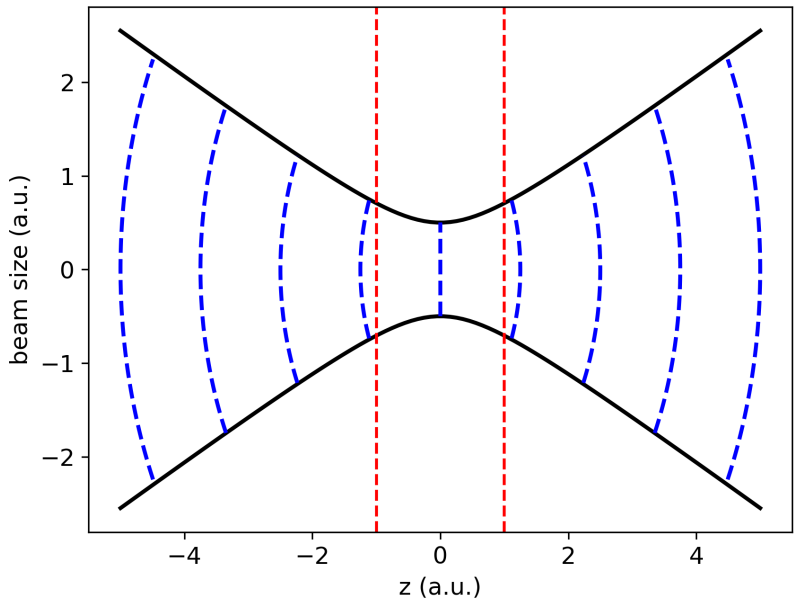

Figure 2.7: Plot of a Gaussian beam with a beam waist $w_0 = 0.5$ and Rayleigh range $z_0 = 1$. The dashed blue lines are the wavefronts at different z-position. The dashed red lines are the positions of z_0.

diameter D and $z_0 \gg f$ using a lens is a standard case in optics textbooks. The spot size $2w_0'$ is given by [Saleh and Teich, 2007]:

$$2w_0' \approx \frac{4\lambda}{\pi}\frac{f}{D}. \tag{2.40}$$

This formula is extremely important in the design of optical setups, it shows that to focus a collimated beam with a wavelength λ into a small spot, It is desirable to have:

1. An input beam with a large D.
2. A lens with a short f.

2.5.2 Plane wave decomposition of a Gaussian beam

Gaussian beams satisfactorily model laser beams in optical systems. In this thesis, we will encounter a situation in which a Gaussian beam excites a PhC-patterned membrane. To model such process, RCWA analysis can be used to model optical structures which are periodic in the transverse direction, and homogeneous in the longitudinal direction. This is ideally the situation in a 2D PhC slab. However, a main limitation of this analysis is that it assumes the structure is infinitely periodic in the transverse direction. i.e. diffraction at the edges due to the termination of the

slab can not be modeled, nor the optical losses due to the finite slab size. Another limitation is that RCWA simulates plane waves. Thus, one can not directly model the excitation of a PhC slab with a Gaussian beam. Thus, Gaussian beams have to be decomposed into plane waves incident from all possible directions [Moura et al., 2018].

Assuming that the RCWA simulations are computed for all plane waves, and the reflection coefficients $r_{s,p}(\phi, \theta, \lambda)$ are computed, where s and p denote s-polarized Gaussian beam and p-polarized Gaussian beam, respectively. ϕ is the polar angle, and θ is the azimuthal angle. The full coordinate system is described in Fig. 2.8, where the implementation is discussed. If the sample position is adjusted at the beam waist ($z = 0$) position at normal incidence, The distribution of the electric field E at the waist is [Moura et al., 2018]:

$$E(x, y) = \sqrt{\frac{2}{\pi w_0^2}} \exp^{-\frac{x^2+y^2}{w_0^2}}, \tag{2.41}$$

$E(x, y)$ can be Fourier transformed according to the plane wave decomposition:

$$E(k_x, k_y) = \iint E(x, y) \exp^{i(k_x x + k_y y - \frac{2\pi c}{\lambda} + \phi)} \, dx \, dy. \tag{2.42}$$

Finally, the computed $r_{s,p}(\phi, \theta, \lambda)$ are weighted by the plane wave decomposition in spherical coordinates. Thus, the reflectivity spectrum can be written as [Moura et al., 2018]:

$$R_{s,p}(\lambda, w_0) = \frac{\iint |r_{s,p}(\phi, \theta, \lambda)|^2 \exp^{-\frac{1}{2}(w_0 k \sin(\phi))^2} \sin(\phi) \, d\theta \, d\phi}{\iint \exp^{-\frac{1}{2}(w_0 k \sin(\phi))^2} \sin(\phi) \, d\theta \, d\phi}. \tag{2.43}$$

Eqn. 2.43 will be extremely important in simulating the interaction of a Gaussian beam with a PhC slab in this thesis.

2.5.3 Gaussian beam reconstruction

S^4 free software package is used to do the RCWA analysis for incident plane waves. The S^4 code starts with defining a unit cell in the xy plane. Since our PhC forms a square lattice, thus, the unit cell is a square with side length a, where a is the period of the PhC. Next, the pattern is added which is a circle with radius r. The material is defined to be GaAs in the slab, and vacuum in the holes. Finally, the layers are defined in the z-direction, which is only the 100 nm PhC slab for this purpose. The slab is surrounded by semi-infinite vacuum layers from the top and bottom. All the relevant dimensions and the spherical coordinate system for plane wave incidence are shown in Fig. 2.8.

One of the most important simulation parameters is the number of Fourier modes in each unit cell. This constitutes a trade-off between accuracy and computational

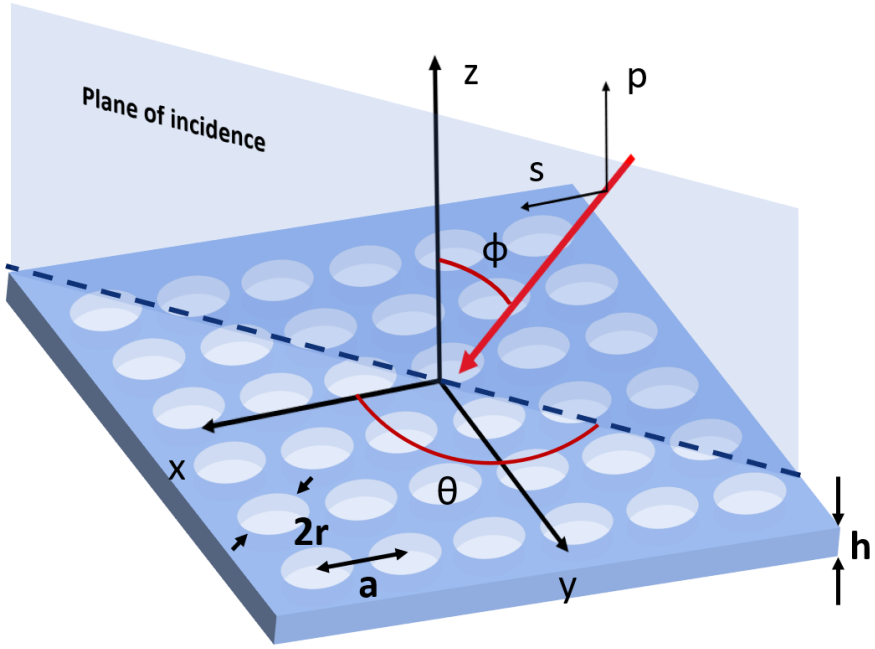

Figure 2.8: Plane wave incident on a PhC slab in spherical coordinates system. ϕ is the polar angle $\vec{k}$ makes with z-axis , θ is the azimuthal angle defined between the projection of $\vec{k}$ on the xy plane and the positive x-axis. *s*-polarization is defined by having the electric field perpendicular to the plane of incidence. *p*-polarization is when the electric field is parallel to the plane of incidence. Note that for the Gaussian beam, the *s* and *p* polarization components of each plane wave have to be transformed according to eqn 2.45 and 2.47.

time. Fig. 2.9 shows the reflectivity spectrum of a plane wave incident at $\phi = 5°$ and $\theta = 30°$ on a PhC slab with $r = 418$ nm and $a = 1081$ nm as a function of the number of Fourier modes used. The choice of the r and a values will be justified in the results section. We can observe that as the number of Fourier modes increases, the simulations converge to the same curve. However, this comes at the expense of computational time which increases dramatically. The maximum shift in the curve between different simulations is about 2 nm and no other significant changes are observed. 50 modes were considered satisfactory for our purpose.

To study the polarization dependence of the reflectivity of our structure, one has to align the polarization of all incident plane waves uniformly for all angles. The S^4 simulation tool rotates the coordinate system when rotating the incident plane wave. The following transformation for the s and p components of the electric field $\vec{E}$ is done to compensate for this rotation [Moura et al., 2018]:

$$E_s \Rightarrow \frac{\cos\theta}{\cos\phi}, \tag{2.44}$$

$$E_p \Rightarrow -\sin\theta, \tag{2.45}$$

for an s-polarized Gaussian beam, and:

$$E_s \Rightarrow \frac{\sin\theta}{\cos\phi}, \tag{2.46}$$

$$E_p \Rightarrow \cos\theta, \tag{2.47}$$

for a p-polarized Gaussian beam. The coordinate system is shown in Fig. 2.8, where the angles ϕ, θ and both s and p polarization of a plane wave are defined. In principle, plane waves incident from all possible θ and ϕ angles should be considered. However, one can make use of symmetry arguments to reduce the computational space of our problem. For the polar angle ϕ, there is a mirror symmetry around normal incidence, which allows to reduce simulation points by half. One can reduce the computational space further by noting that the value of the beam waist w_0 determines the angular contribution of the tilted plane waves. Fig. 2.10 plots the function $\left(\exp^{-\frac{1}{2}(w_0 k \sin(\phi))^2} \sin(\phi)\right)$, which is the weighting factor of plane wave $r_{s,p}(\phi, \theta, \lambda)$ in eqn 2.43. One can see that for smaller w_0, more tilt angles contribute to the Gaussian beam. Nonetheless, our smallest beam waist is $w_0 = 4.2$ μm, thus only a limited range of ϕ angles contribute to the integral. Therefore, our simulations are done for the range $0° \leq \phi \leq 10°$ in steps of 0.25°.

Furthermore, the crystal symmetry can be used to reduce the number of points of the azimuthal angle θ. Intuitively, the symmetry of square lattice should reduce the range for θ to $0° \leq \phi \leq 45°$. But this is not true in our case, because the polarization

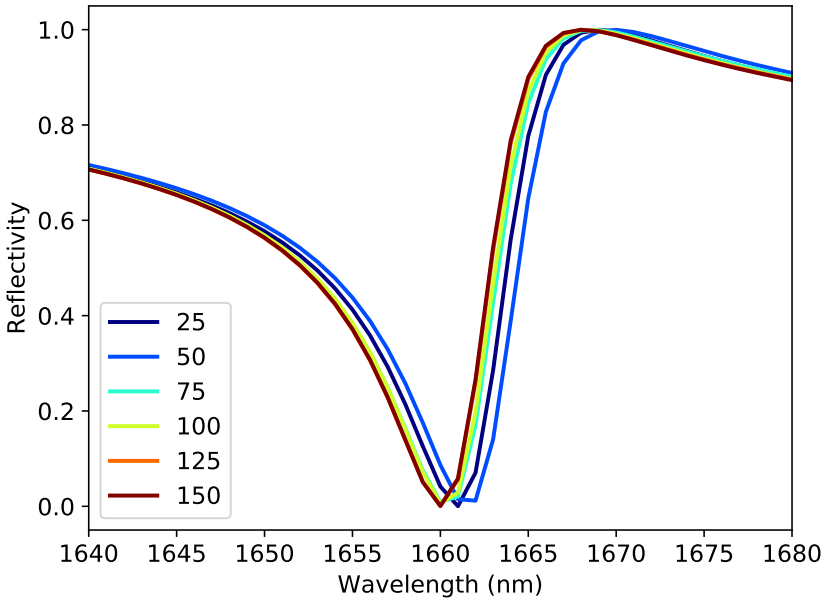

Figure 2.9: Reflectivity spectrum of a plane wave incident at $\phi = 5°$ and $\theta = 30°$ on a PhC slab with $r = 418$ nm and $a = 1081$ nm for different number of simulated Fourier modes per the unit cell.

alignment for all incident waves reduces the symmetry to 90°. i.e. double the value. Therefore, the simulations are done for the range $0° \leq \theta < 90°$ in steps of 2.5°.

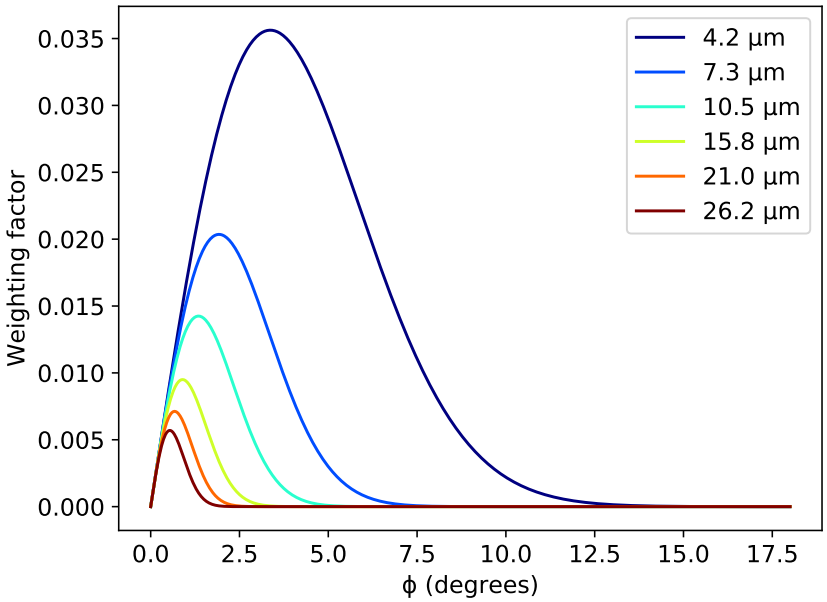

Figure 2.10: Plot of the weighting factor of plane wave components as a function of the polar angle ϕ for different beam waists w_0.

3

Methods

This chapter discusses the experimental methods used in this thesis. Firstly, we are interested in the mechanical eigenfrequencies ω_m and quality factors Q_m of the GaAs membranes. To this end, *homodyne detection* scheme is used for the mechanical characterization of our devices. Moreover, to determine different mechanical eigenmodes experimentally; a mode tomography technique based on *homodyne detection* is implemented. This technique characterizes the mode shape of different eigenmodes in order to compare them to FEM simulations. The operation of these measurement procedures is fully automated, which was a main task in this thesis. On the optical side, we are mainly interested in the optical reflectivity of our fabricated devices. Therefore, we designed an experimental setup which could measure the optical reflectivity of our devices at normal incidence.

3.1 Mechanical characterization

3.1.1 Homodyne detection

As discussed in section 2.1.3, a harmonic oscillator is in contact with a thermal bath at temperature T, and thus, is subject to a random force. This random force excites different mechanical modes of the suspended membrane. In our experiments, we are interested in different physical quantities such as: mechanical displacement, mechanical frequency ω_m, mechanical damping γ_m and the mechanical quality factor Q_m. To experimentally measure these quantities, *homodyne detetction* is used.

When a laser beam ($\lambda = 1550$ nm) is reflected from a membrane at normal incidence, the optical path length $\Delta\Phi = \Delta x k$ is modulated by the vibration of the membrane Δx which changes the phase of the laser beam. In order to detect phase change, a reference signal is needed so that the measurement can be done interferometrically. To this end, the original laser beam is split into two arms: 1) A strong local oscillator arm to be used as a reference. 2) A weak signal arm which is modulated by the membrane. This is the main principle of *homodyne detection*, where the reference signal is generated from the same source. This is in contrast to *heterodyne detection*, where the reference signal is generated from a different source with a different

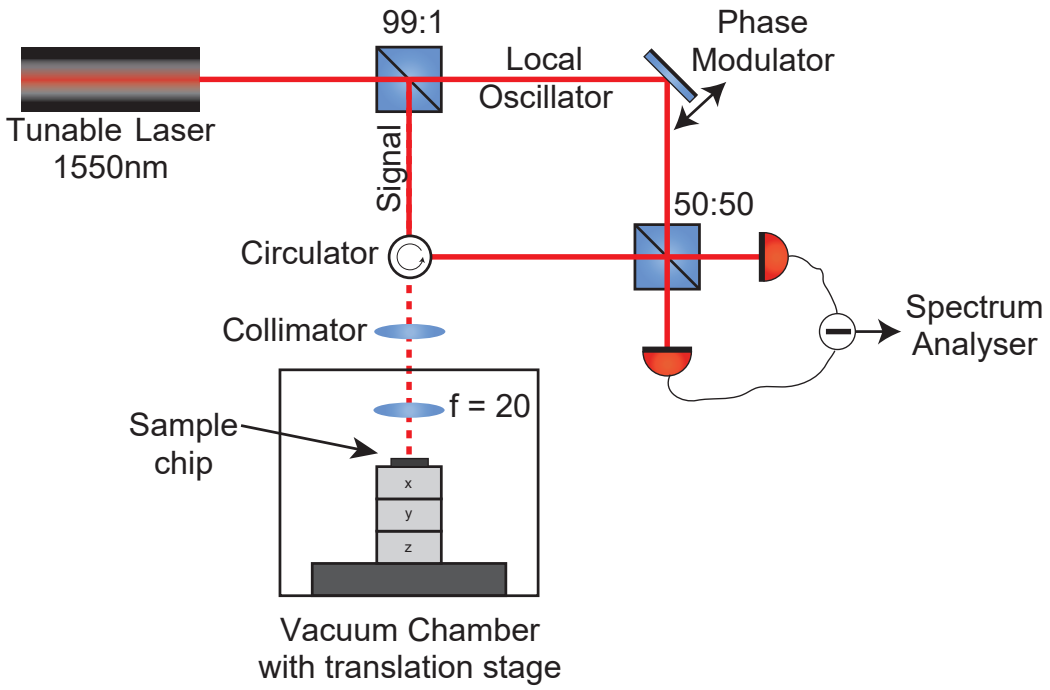

Figure 3.1: Schematic of the homodyne detection setup for the mechanical characterization of GaAs membranes. A 1550 nm laser source is split by a 99:1 beamsplitter into two arms: 1) A strong local oscillator arm. 2) A weak signal arm. The signal arm passes through a circulator, and then, it is collimated to free space - the red dotted beam - by means of a fiber collimator. The laser beam is focused on the membrane in the vacuum chamber using a focusing lens. Then, it reflects from the membrane at normal incidence and is coupled back into the optical fiber. The two signals interefere on a beamsplitter. The difference signal of the detector is the homodyne signal, which contains information about the amplitude and the phase quadratures of the signal field. This depends on the the relative phase between the two arms as the phase of the local oscillator arm is controlled by a phase modulator. The chip is placed on an xyz piezo-translation stage to adjust the vertical position to the focus of the lens, and to move between different membranes in the xy direction. Courtesy of Sushanth Kini, Chalmers.

frequency. A schematic of the setup is shown in Fig. 3.1, if one assumes a signal with steady state amplitude α_s, and an amplitude and phase fluctuation δX_s and δY_s around the steady state value α_s, respectively. The signal can be written as [Gröblacher, 2012]:

$$\alpha_s(t) = \alpha_s + \delta X_s(t) + i\delta Y_s(t), \tag{3.1}$$

where α_s, δX_s and δY_s are real numbers. δX_s and δY_s are referred to as the amplitude

and phase quadrature. Similarly, the local oscillator signal can be written as:

$$\alpha_{lo}(t) = (\alpha_{lo} + \delta X_{lo}(t) + i\delta Y_{lo}(t))e^{i\phi}, \tag{3.2}$$

where ϕ corresponds to the phase difference between the signal arm and the local oscillator arm. As shown in Fig. 3.1, the signal from both arms interfere on a beamsplitter, and two photodetectors measure photocurrents i_{D1} and i_{D2}. The homodyne signal is the difference of these two currents. The full derivation can be found in [Gröblacher, 2012], and the final result is:

$$i(t) = i_{D1} - i_{D2} \approx 2\cos(\phi)\alpha_{lo}\alpha_s + 2\alpha_{lo}[\cos(\phi)\delta X_s(t) + \sin(\phi)\delta Y_s(t)]. \tag{3.3}$$

This is a very simple and interesting result. It shows that the homodyne signal consists of a DC term and an AC term. The AC signal is modulated by δX_s and δY_s depending on the relative phase ϕ between the two arms. In other words, by controlling ϕ, one can choose to measure the amplitude quadrature or the phase quadrature or a combination of both of them. Since in our experiment we are interested in the phase quadrature, as the membranes modulate the phase of the laser beam, the AC signal is fed-back to a PID controller which creates an error signal and locks onto the phase quadrature, i.e. locks on the position of maximum slope which corresponds to maximum sensitivity to phase change ϕ. The output voltage of the PID controller is fed to the phase modulator in the local oscillator arm. Using this feedback loop, the PID controller keeps ϕ locked on the phase quadrature.

The homodyne signal $i(t)$ is fed to the Keithley N9020B MXA spectrum analyzer, which does a Fourier transform and gives the noise power spectrum. Fig. 3.2 shows the noise power spectrum of a 70 μm $\times$ 40 μm un-patterned GaAs membrane. We can observe that the electronic noise power level is significantly lower than the shot noise level of the input laser at higher frequencies. On the other hand, $1/f$ noise dominates at low frequencies. Moreover, we can observe the homodyne signal peaks at different frequencies. The noise level of the homodyne signal matches the shot noise level, which should be the case in *homodyne detection*. It is important that our noise level is dominated by the shot noise of the laser source and not by the electronic noise of the equipment to achieve the maximum possible signal to noise ratio (SNR).

3.1.2 Automation of mechanical quality factor measurements

The homodyne signal contains different frequency components which correspond to the mechanical eigenfrequencies. However, it also contains spurious frequency components which do not correspond to mechanical motion. One method to check if the peak corresponds to mechanical motion is by using a piezoelectric transducer connected to an RF signal generator. The piezoelectric element is also in contact with the mount of the chip. If the frequency of the RF source matches a mechanical

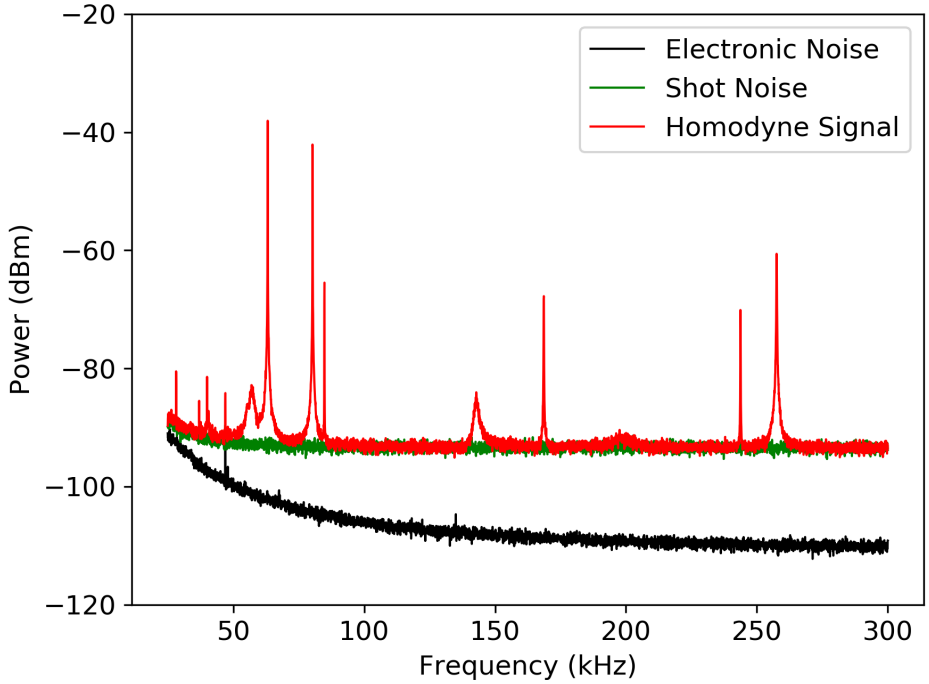

Figure 3.2: Noise power spectrum of a 70 μm $\times$ 40 μm un-patterned GaAs membrane showing the homodyne signal, electronic noise and shot noise levels.

eigenfrequency, then the eigenmode should get excited which is directly seen in the noise power spectrum. In case of increasing the driving voltage, higher order resonance modes start to appear. On the other hand, if the peak is produced by some electronic circuitry, then it is not excited by the piezoelectric element.

The mechanical quality factor Q_m is an important physical parameter for mechanical resonators as explained in section 2.1.3. But in order to estimate Q_m from eqn 2.8, both the mechanical eigenfrequencies ω_m and mechanical damping γ_m are needed. ω_m is directly accessible from the spectrum analyzer, while γ_m is not directly accessible. In order to measure γ_m, one can make use of eqn 2.15 to fit each mechanical peak to a lorentzian while using γ_m as a fitting parameter. Another method is to excite each mechanical mode with a piezoelectric element, and extract γ_m from fitting the exponential decay according to eqn 2.7. Both methods will be used in this thesis and will be discussed in the next sections in more detail.

In order to analyze many devices and many mechanical modes, it is important to automate the measurement procedure of Q_m such that it is done for all devices on chip without intervention. This requires synchronization between the spectrum analyzer, the signal generator and the piezo-translation stage. In addition, data analysis and fitting is needed to extract different physical parameters. Python programming language allows easy control of different instruments through pyvisa library. Moreover, data manipulation, analysis and plotting through numpy and matplotlib libraries is also straightforward, which makes Python well suited to the task.

3.1.2.1 Piezo-translation stage

The chip is mounted on Attocube ANPz101 piezo-translation stage. Attocube ANC350 controller is used to change the xyz position of the stage. This allows moving between different membranes and adjusting the vertical position to be in the focus of the lens inside the vacuum chamber. The automation of the piezo-translation stage is done through pyvisa library. To specify the location of different membranes, one can take advantage from having all devices on chip in a regular grid as shown in Fig. 3.3. To be able to locate different devices, an illumination setup is built - not shown in schematic - where a wideband light source and lenses are used to form a magnified image of the chip on a Si CCD camera. Since the 1550 nm laser is not visible on the CCD, a 980 nm laser is coupled into the same optical fiber via a wavelength division multiplexer (WDM) to uniquely determine which device is being probed as it is visible on the CCD. This idea provides a cheap alternative to using an IR camera. Manually, one adjusts the position and focus of the bottom left membrane of the chip. Similarly, the optimal position for the top left membrane is also specified - both devices are marked by blue dots -. By knowing the x and y coordinates of two devices, and specifying the number of columns and rows on the chip, a 2D grid of all device locations is created. Using this simple approach, it is possible to probe all membranes automatically.

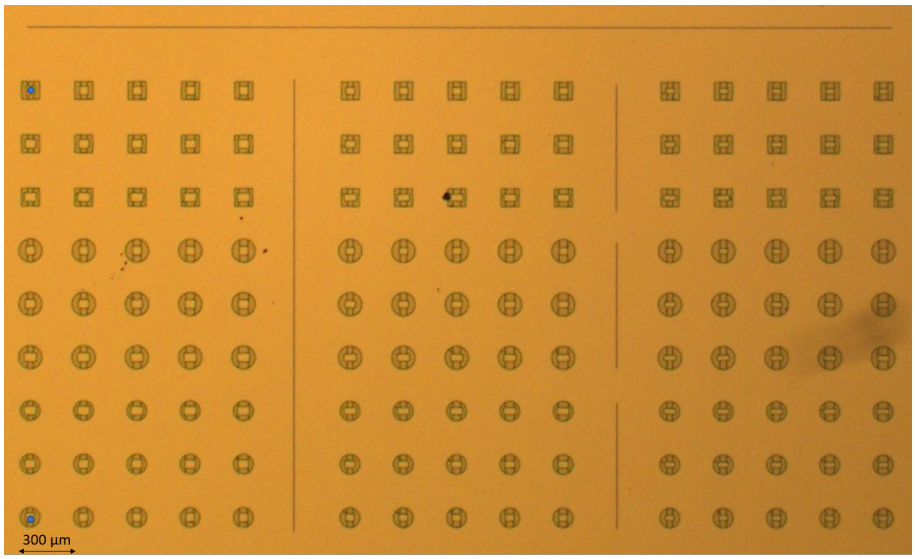

Figure 3.3: An optical microscope image of suspended GaAs membranes on chip. The two blue dots point to the devices whose coordinates are used to make a 2D grid of all membrane locations on chip.

3.1.2.2 Extraction of mechanical eigenfrequencies

Once the piezo-translation stage moves to a new device, the first step is to extract the eigenfrequencies ω_m of the membrane. The frequency range of interest is specified, which is between 30 kHz and 300 kHz in Fig. 3.2 for example. The spectrum is

averaged for 100 times, and the frequencies of different resonance peaks is extracted by using the peak search command of the spectrum analyzer. Note that at that moment, we are not certain that the extracted peaks correspond to mechanical eigenmodes. The next step is to study each peak and estimate Q_m if it corresponds to a mechanical eigenmode. For this we use two different techniques: 1) Lorentzian fit. 2) Ringdown fit.

3.1.2.3 Lorentzian fit method

As previously mentioned, The first approach to extract the mechanical damping γ_m is to specify a narrow frequency range around a single peak with the minimum possible bandwith allowed by the spectrum analyzer, that is 1 Hz, and average the spectrum for an appropriate number of cycles to improve SNR and resolve the peak. An example trace is shown in Fig. 3.4. Next, we make use of eqn 2.15, which was derived in section 2.1.3. The equation shows that a damped harmonic oscillator with $Q_m \gg 1$ can be approximated by a Lorentzian function with FWHM γ_m. The following equation is used for curve fitting using Scipy Python library:

$$y(f) = y_0 + \frac{A}{(f - f_0)^2 + (\gamma')^2}. \tag{3.4}$$

This is an equation for a Lorentzian-like function at a center frequency f_m with a constant noise background y_0. f_m is already extracted from the previous measurement step ($\omega_m = 2\pi f_m$), and y_0 is the background noise level. This leaves us with only 2 fitting parameters: A and γ'. It is important to notice the difference between eqns 3.4 and 2.15, which leads to a conversion factor of 4π between the fitted γ' and the physical quantity γ_m; i.e. $\gamma_m = 4\pi\gamma'$.

An example of the fitting is shown in Fig. 3.4, where we can see that a Lorentizan nicely matches the experimental data giving $\gamma' = 2.034 \pm 0.014$ Hz, which corresponds to $Q_m = (1.930 \pm 0.013) \times 10^4$. The accuracy of the fitting parameter γ' is limited by the minimum bandwidth of the spectrum analyzer which is 1 Hz. Therefore in our implementation, if $\gamma' > 3.0$ Hz, the calculation is considered as an accurate estimate for Q_m. Otherwise, The code proceeds with ringdown measurement. Note that if the peak is a spurious peak and not a mechanical eigenmode, the lorentzian fit would still work but it would give an unrealistically large value for the Q_m. As a result, the ringdown measurement will proceed which is able to distinguish mechanical peaks from spurious ones.

3.1.2.4 Ringdown measurement

The idea of a ringdown measurement can be intuitively understood in analogy to exciting a guitar string. Once a guitar string is excited by being pulled for example,

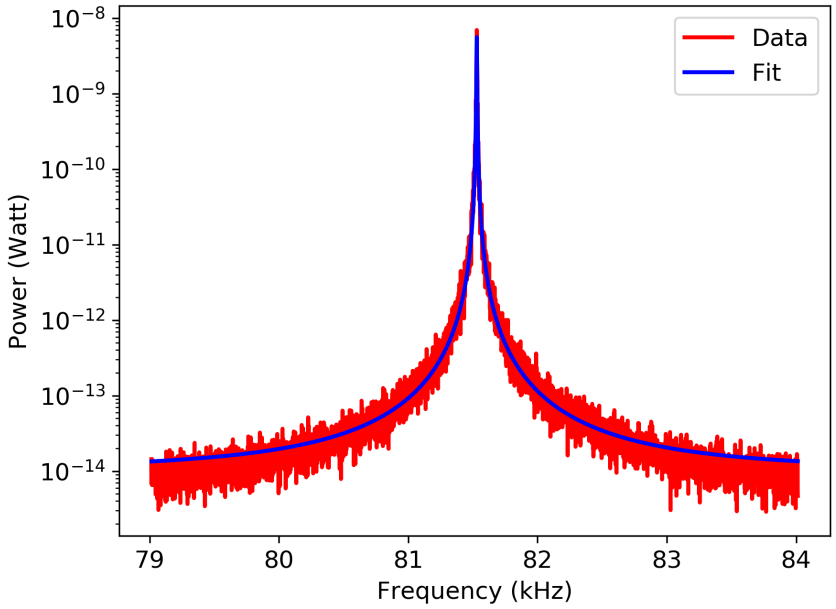

Figure 3.4: Experimental data of the noise power spectrum of a mechanical eigenmode and the corresponding Lorentzian fit. The fitting gives $\gamma' = 2.034 \pm 0.014$ Hz, and $Q_m = (1.930 \pm 0.013) \times 10^4$.

the amplitude of the oscillation decays exponentially according to the equation:

$$x(t) = x_0 e^{-\frac{\gamma_m t}{2}}, \tag{3.5}$$

where x_0 is the initial amplitude. This equation is the envelope part of eqn 2.7. The time it takes for the amplitude to decay to $1/e$ of its initial value is $2/\gamma_m$. The equation for the power is square of that of the amplitude and is given by:

$$P(t) = P_0 e^{-\gamma_m t}, \tag{3.6}$$

where P_0 is the initial power. We can easily see that the time it takes for the power to decay to $1/e$ of its initial value is $1/\gamma_m$. i.e., half of that for the amplitude. In our setup, the mechanical mode is excited using a piezoelectric transducer, which is excited by a RF signal generator with a certain voltage at the frequency of the mechanical mode of interest. Similar to the Lorentzian fit approach, Python Scipy library is used for curve fitting. The fitting is done in a logarithmic scale. By taking the natural logarithm of eqn 3.6, we reach following equation:

$$y(t) = y_0 - \gamma_m (t - t_0), \tag{3.7}$$

where $y(t)$ is the power as a function of time, y_0 is the background noise level and t_0 is the time at which the mechanical mode is excited. Therefore, γ_m is the only fitting parameter. Fig. 3.5 shows the experimental data for ringdown measurement, and the linear fit which gives $\gamma_m = 8.085 \pm 0.004$ Hz; this corresponds to $Q_m = (4.990 \pm 0.003) \times 10^4$. This measurement is for a mode different from the one in Fig. 3.4. It is important to note that if the peak is a spurious resonance, then it will not be possible to excite it, and it will be recorded that the peak does not correspond

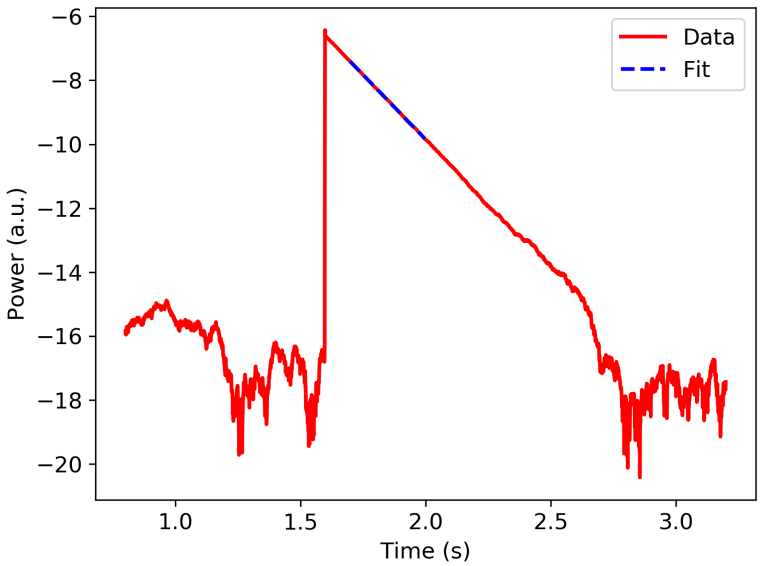

Figure 3.5: Experimental data of the ringdown measurement of a mechanical eigenmode and the corresponding ringdown fit. The fitting gives $\gamma_m = 8.085 \pm 0.004$ Hz, and $Q_m = (4.990 \pm 0.003) \times 10^4$.

to a mechanical mode. Moreover, it is obvious that spurious peaks are replicated in different measurements and it is straightforward to neglect them once they are known.

There are some important considerations that must be taken into account during the ringdown measurement. Firstly, There is a mismatch between the frequency given by the signal generator and the one given by the spectrum analyzer as they do not have the same reference clock. Secondly, each mechanical mode responds differently to the excitation voltage V_{pp}; some modes need considerably high $V_{pp} > 5$ V to be excited, while other modes can get excited by $V_{pp} < 10$ mV. It is not possible to use a single high V_{pp} of, for example 5 V, for all modes as it leads to heating of the mechanical mode which shifts ω_m and strongly affects the measurement. A common solution lies in doing a frequency sweep in a small window of 100 - 200 Hz in steps of 1 Hz around ω_m to find ω_m' due to the frequency mismatch, and accompanied to that, V_{pp} is swept until a signal to noise ratio > 20 dB is reached, which is found to be optimal and does not cause heating of the mechanical mode. An example trace is shown in Fig. 3.6, where we can see that the maximum power is achieved at a detuning = - 16 Hz at $V_{pp} = 5$ mV.

3.1.3 Mode tomography

The different eigenmodes supported by our GaAs membrane were shown in section 2.1.2 through FEM simulations. The *homodyne detection* discussed so far gives

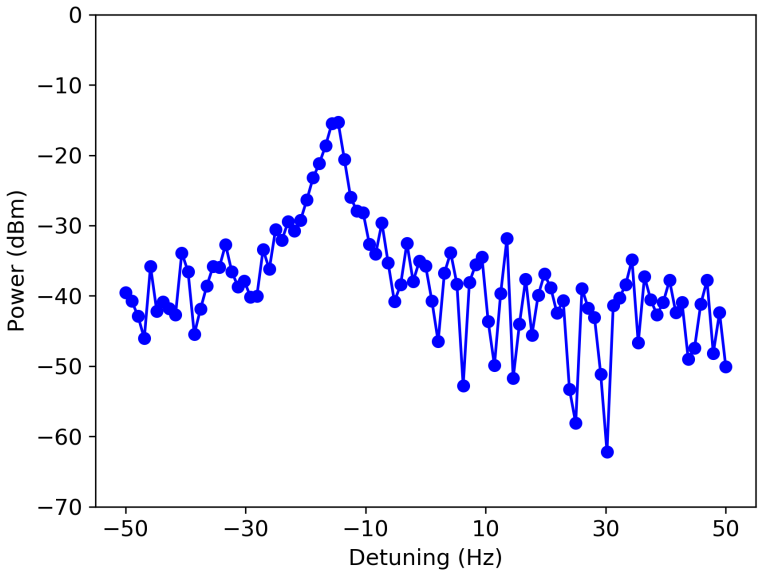

Figure 3.6: Power as a function of the detuning between the signal generator excitation frequency and the spectrum analyzer frequency.

access to ω_m and Q_m of the eigenmodes. However, the mode shape of each peak in the noise power spectrum is not known. Here, I present a technique in which the same setup is used to probe the mode shape of each eigenmode in the noise power spectrum.

Eqn 2.14 shows that the area under the experimentally measured mechanical peak equals the variance of the mechanical displacement. We use a highly focused 1550 nm laser beam with $w_0 = 4.2$ μm to probe different positions on the membrane as shown in Fig. 3.7a. At each of these positions, one gets a noise power spectrum with several mechanical modes. If one considers a single mechanical mode, then the area under the lorentzian-fitted curve is proportional to the variance of the mechanical motion (Fig. 3.7b). Thus, we can measure the mechanical mode shape by performing a 2D scan over the area of the membrane. Fig. 3.7c shows a heatmap of the normalized RMS-displacement in the z-direction of the Free-Free mode of 70 μm $\times$ 40 μm GaAs membrane. Fig. 3.7 shows the FEM simulation of the Free-Free mode for a membrane with the same geometry.

Similar to the Q_m measurement procedure, the mode tomography technique is automated using Python. The piezoelectric translation stage is moved in small displacement steps of 1-2 μm, and the noise power spectrum is integrated for each mechanical peak at each membrane position. Once the scan is finished, the data is post-processed by taking the square root of the measured values to get a value proportional to the RMS-displacement, and then the data is normalized by the largest value in the scan.

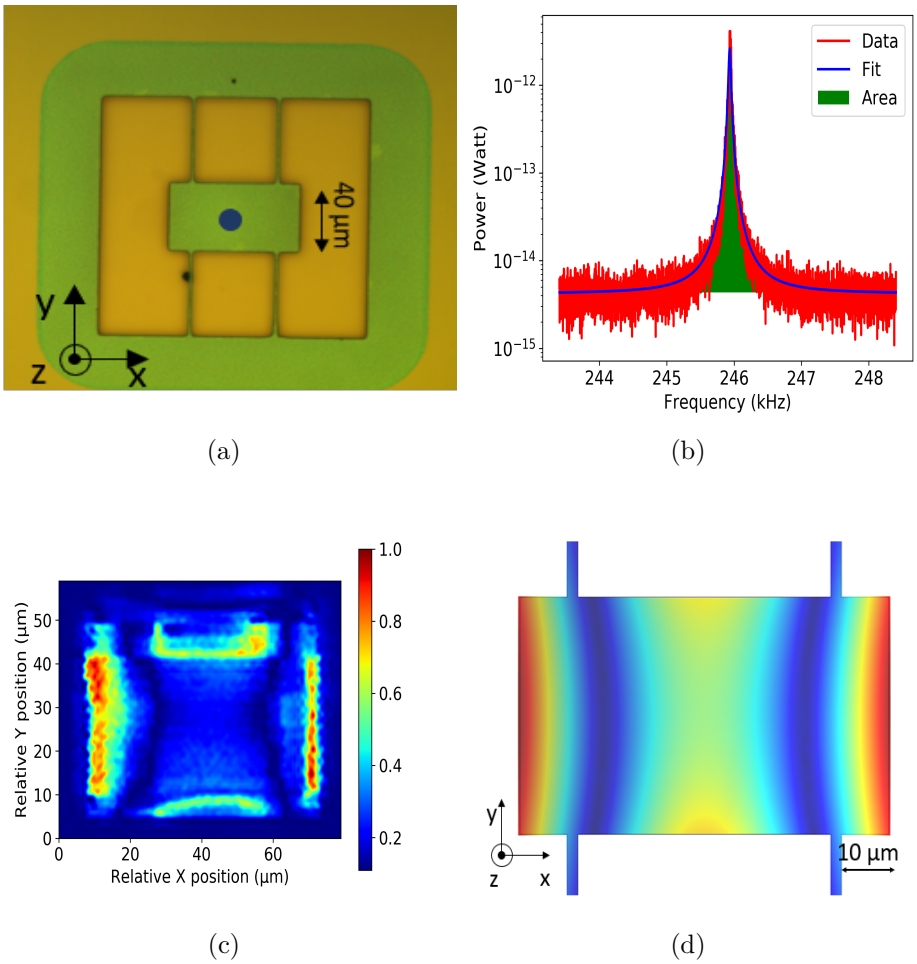

(a) (b)

(c) (d)

Figure 3.7: Mode tomography of 70 μm $\times$ 40 μm un-patterned GaAs membrane. (a) Optical microscope image of a free standing GaAs membrane, the blue dot show the gaussian laser spot probing the membrane at a random position. (b) Example of the noise power spectrum of a mechanical eignemode, the shaded green region show the area under the fitted curve. (c) 2D Heatmap of the normalized RMS-displacement of the Free-Free mechanical mode. (d) FEM simulations of the Free-Free mode.

3.2 Optical characterization

As discussed in section 2.4.3, the design of PhC pattern is optimized to achieve $R \approx 1$ at $\lambda = 1550$ nm. To experimentally verify that such reflectivity is achieved, an optical reflectivity setup was built to probe GaAs membranes as shown in Fig. 3.8. The basic idea is splitting a laser beam using a polarizing beam splitter into two beams: 1) Reference beam. 2) Probe beam. Normalizing the probe beam reflected from the membrane by the reference beam gives the reflectivity of the membranes. To account for optical losses in the setup, the reflectivity spectrum is normalized by the measured reflectivity spectrum of a silver mirror with known reflectivity ($R_{mirror} \approx 0.982$).

Thus, the reflectivity spectrum can be written as:

$$R = \frac{V_{reflected}/V_{reference}}{V^{mirror}_{reflected}/V^{mirror}_{reference}} R_{mirror}, \tag{3.8}$$

where $V_{reflected}$ and $V_{reference}$ are the photodetector's output voltage of the reflected power arm and the reference power arm for the measured device, respectively. Similarly, $V^{mirror}_{reflected}$ and $V^{mirror}_{reference}$ are the photodetector's output voltage of the reflected power arm and the reference power arm for the silver mirror. Reflectivity of PhC slabs are highly sensitive to small changes in tilt and deviation from normal incidence [Lousse et al., 2004]. Therefore, special care is needed in aligning our devices. To overcome this challenge, a circulator is added before the triplet collimator. The third port of the circulator is connected to a power meter which reads the reflected power from the membrane during alignment. The power meter is monitored while adjusting the sample position and tilt until maximum power point is found, which provides an extremely sensitive way to align the sample position to be at normal incidence.

Although the PhC slabs are designed for maximum reflectivity at 1550 nm, we are also interested in the spectral response of our devices in a wider wavelength span. The Toptica laser is continuously tunable between 1520 nm and 1630 nm. Studying the full range allows better understanding of the physics of the PhC membranes. Moreover, the wavelength at which maximum reflectivity is achieved can be shifted due to microfabrication errors. The measurement procedure is automated through Python. Pyvisa library is used to communicate with the laser controller to do a wavelength sweep in steps of 0.25 nm. The photodetectors are connected to a custom-made electronic board which provides a gain of 10^4 to the signal. An analog to digital converter (ADC) digitizes the signal and transmits it to Arduino nano. A serial communication link is established between the board and the PC to read the voltage output of the photodetectors.

Fig. 3.9 shows the spectral response of the reference silver mirror. It can be seen that the spectral response of the reference and reflected power are wavelength dependent. This is due to the fact that the laser output power is not constant and it depends on wavelength. Fig. 3.10 shows the normalized reflectivity spectrum and the calibration curve provided by Thorlabs. The measured reflectivity is nearly flat showing peak $R \approx 0.96$. The deviation from the calibration curve is due to the losses from the optical elements and non-ideal spectral response as all elements are optimized to operate at 1550 nm. Moreover, it was found that the spectral behaviour of the setup is highly dependent on the chosen polarization. The dichroic mirror spectral response is flat in case of vertical polarization as shown in Fig. 3.11. On the contrary, choosing a different alignment makes the final spectrum highly wavelength dependent. Generally, this should not be a problem as all the setup systematic errors are corrected for by normalization. However, the setup was aligned such that the input polarization for the dichroic mirror is vertical to get a more flat response.

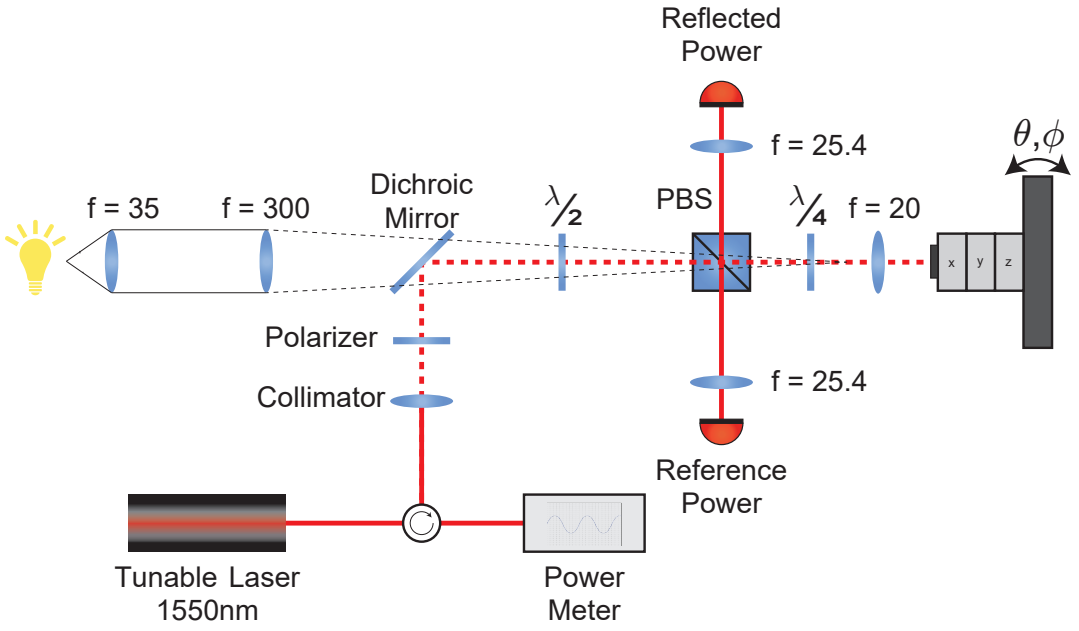

Figure 3.8: Schematic of the optical reflectivity setup. A fiber coupled Toptica tunable laser between 1520 nm and 1630 nm is used to probe the membranes. The optical fiber is coupled to a triplet collimator (Thorlabs TC25APC-1550), which gives a collimated beam of 4.65 mm diameter - the red dotted beam -. The laser beam is transmitted through a linear polarizer which acts as a polarization selective element in the setup. Then, the laser light reflects from a dichroic mirror which is fully reflective at 1550 nm, and semi-transparent for visible light needed for chip illumination. The incoming beam polarization is rotated by a half wave plate to any chosen angle. The polarizing beam-splitter is used to split the incoming light based on its polarization. i.e. vertically polarized light gets reflected into the reference arm and horizontally polarized light gets transmitted. For the transmitted beam, a quarter wave plate changes the linearly polarized light into circularly polarized light, which gets focused by a 20 mm lens into a 4.2 μm laser spot. The focused beam is reflected from the membrane and gets a phase shift of 180° at normal incidence. Due to the phase shift, the polarizing beamsplitter reflects the laser beam into the opposite direction to the reference arm; that is the reflected power arm. Both the reference and the reflected laser beams are focused on an InGaAs photodetector using 25.4 mm focusing lenses. Courtesy of Sushanth Kini, Chalmers.

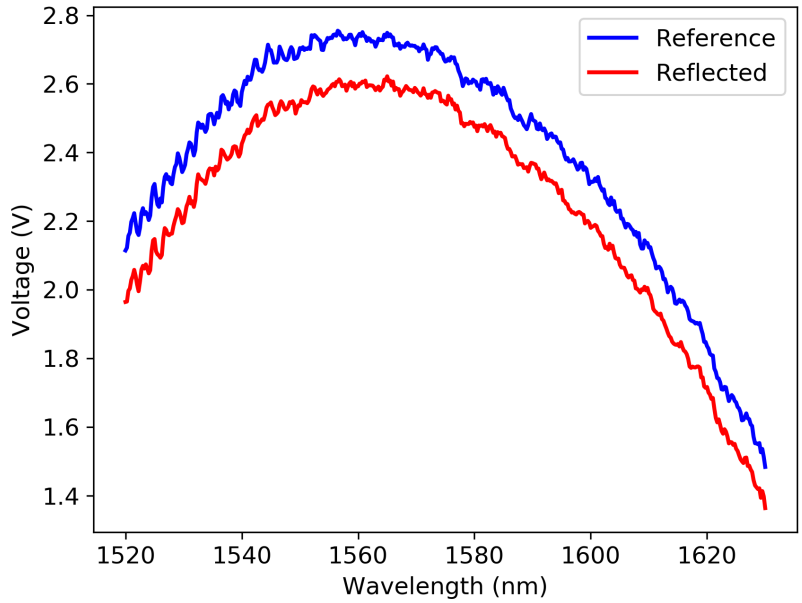

Figure 3.9: Reference and reflected photodetector voltage as a function of wavelength.

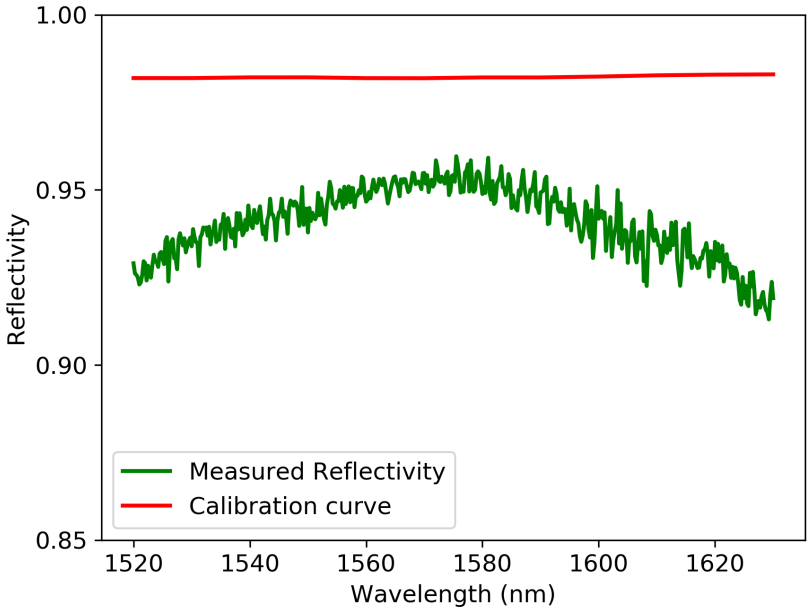

Figure 3.10: Normalized reflectivity spectrum of the silver mirror and the calibration curve provided by Thorlabs.

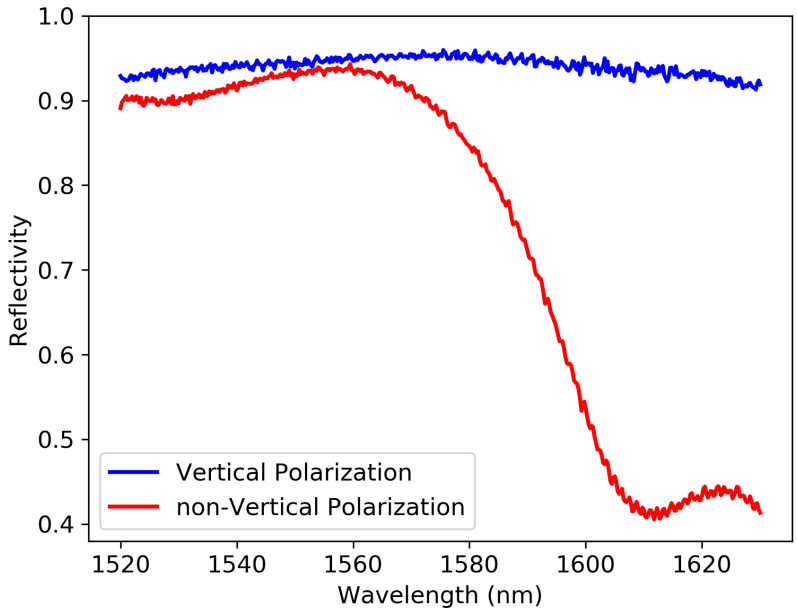

Figure 3.11: Normalized reflectivity spectrum of the silver mirror at input vertical polarization to the dichroic mirror vs non-vertical input polarization.

4

Results

This chapter discusses the main findings of the thesis. For the mechanical properties, the membrane geometry and design parameters are shown. Then, the simulated mechanical eigenfrequencies are compared to experimental results. Mechanical mode tomography technique is developed to probe the mode shape of each eigenfrequency. This allows a direct comparison between each experimental eigenfrequency and the corresponding FEM eigenfrequency, which has the same mode shape. Finally, the quality factor of both PhC-patterned and un-patterned devices are compared. Considering the optical properties, the design of the PhC slab is discussed and the main design parameters are clarified. Next, optical reflectivity measurements are used to investigate un-patterned and PhC-patterned devices. The experimental measurements are supported with numerical simulations; transfer matrix method and RCWA S^4 simulations are done to interpret the measurements. Finally, Gaussian beam reconstruction is implemented to model the interaction of a Gaussian beam with a PhC slab.

4.1 Mechanical characterization

4.1.1 Membrane geometry: design and simulations

The mechanical structure investigated in this thesis is a GaAs rectangular membrane which is supported by two tethers on each side as shown in Fig. 4.1. L and W refer to length and width, respectively. t is the tether position from the center, b is the tether width and h is the membrane thickness as previously introduced. To get an intuitive idea of the dependence of the mechanical eigenfrequencies ω_m on the device geometry, one can use a free-free rectangular beam model, but then, the effect of the tethers is neglected. The eigenfrequencies are [Hall, 2002]:

$$f_1 \approx 1.028 \frac{h}{L^2} \sqrt{\frac{E}{\rho}}, \tag{4.1}$$

$$f_n \approx 0.441 \left(n + \frac{1}{2} \right)^2 f_1, \tag{4.2}$$

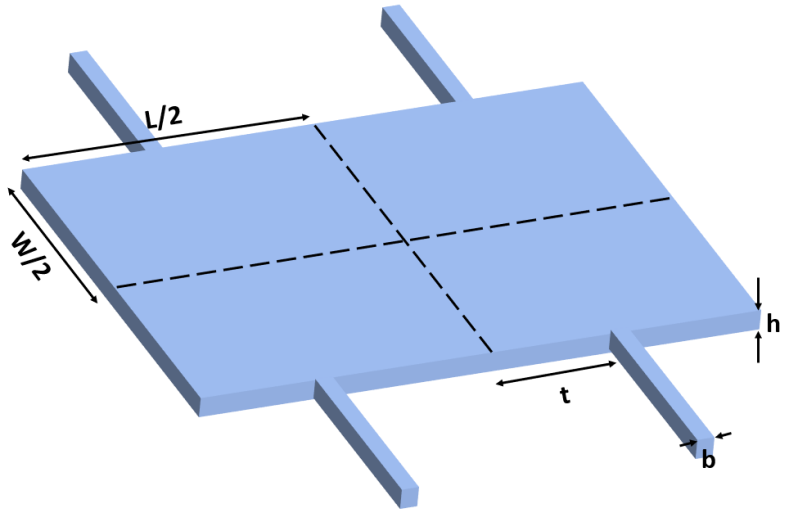

Figure 4.1: Geometry of GaAs membrane simulated using COMSOL multiphysics showing the main geometrical parameters.

where E is Young's modulus and ρ is the material density. Although our structure is not expected to quantitatively obey these equations, as the effect of the tethers is neglected, but some of the important dependencies are captured. Firstly, ω_m is proportional to the speed of sound in medium v; recall eqn 2.2. Secondly, ω_m is directly proportional to h, but inversely proportional to L^2. If we plug some typical numbers for our GaAs membrane: $\rho = 5316$ kg/m^3, $E = 85.9 \times 10^9$ Pa, $h = 100$ nm and $L = 70$ μm, we get $\omega_1 \approx 2\pi \times 82.0$ kHz. This simple calculation shows that our ω_m values are in the 100 kHz range, which is consistent with the observation in the noise power spectrum in Fig. 3.2.

For a more complete analysis, FEM can be used to give a complete set of eigenmodes and eigenfrequenices for any given geometry. The only physical parameters relevant to this problem are E and ρ. Considering the geometry, typical membrane L and W under investigation in this thesis are in the range of 50 μm to 100 μm. A small membrane size is desirable to push ω_m to larger values according to eqn. 4.1. On the other hand, the smallest pad size is limited by the requirement that all the optical power of the focused laser beam falls on the pad to minimize optical losses. Other typical dimensions are $b = 2$ μm, $h = 100$ nm, while t varies among different devices.

COMSOL Multiphysics is used to simulate the membrane geometry shown in Fig. 4.1. The first 5 mechanical eigenmodes of a 70 μm $\times$ 40 μm device are shown in Fig. 4.2. We can recognize the fundamental mode in Fig. 4.2a at an eigenfrequency $\omega_1 = 2\pi \times 12.2$ kHz. The estimated mechanical eigenfrequency value of the first 5 eigenmodes are in the range $\omega_m < 2\pi \times 100$ kHz.

This particular geometry has been extensively studied in literature, and the main motivation behind its adoption lies in the free-free mechanical eigenmode of this structure which is shown in Fig. 4.2d. The quality factor Q_m of the free-free mode

can be enhanced by optimizing the tether position. As shown Fig. 4.2d, if the tethers are placed at the flexural nodes of the free-free mode, the movement of the tethers becomes minimal. As a result, clamping losses are minimized which enhances Q_m [Cole et al., 2010, 2011]. An interesting remark is that eqn 4.1 is a good approximation for the frequency of the free-free mode, given that the tether length is much larger than the membrane thickness [Wang et al., 1999].

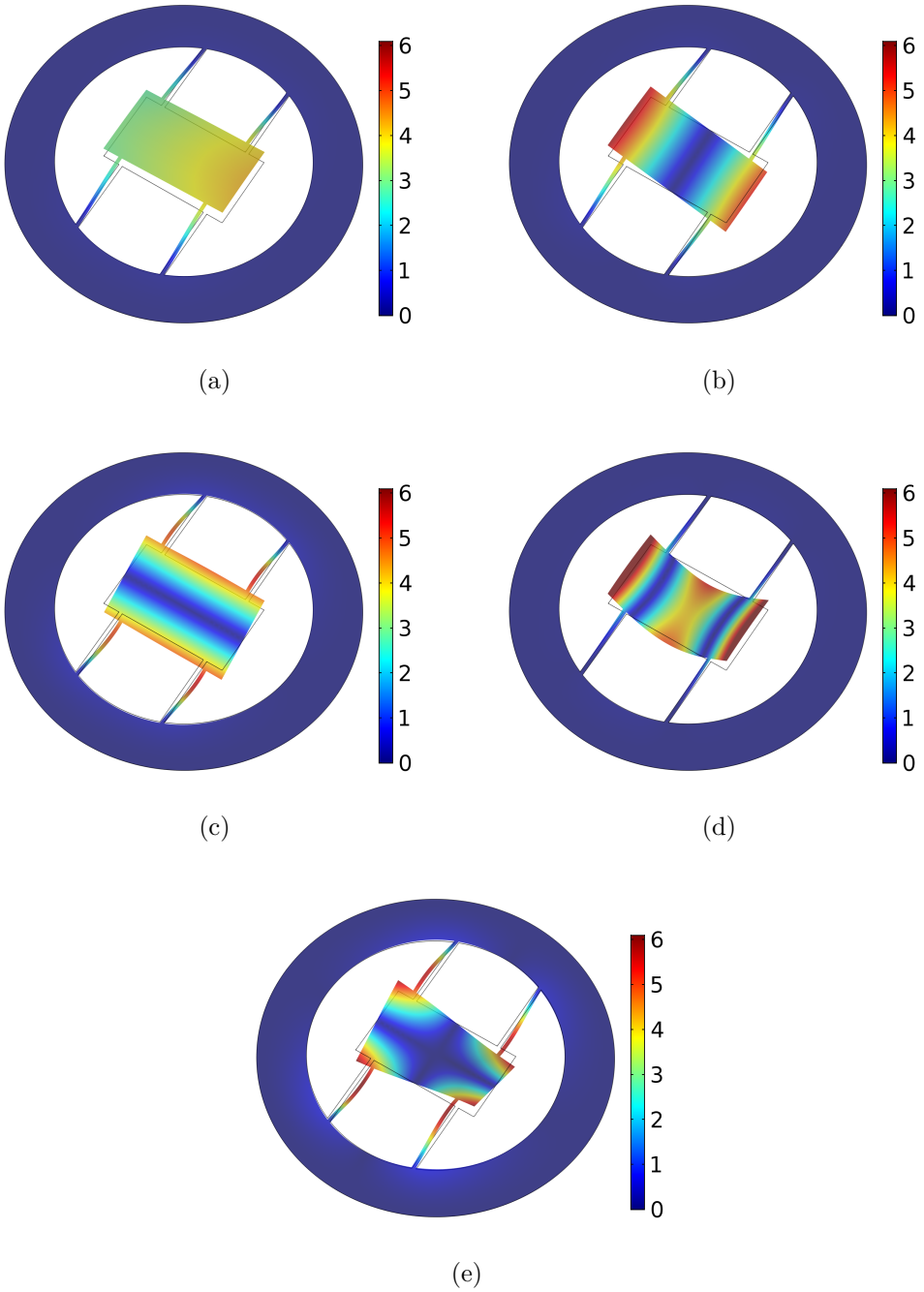

Figure 4.2: The first 5 FEM eigenmodes of a 70 μm $\times$ 40 μm GaAs membrane with h = 100 nm, t = 24 μm and b = 2 μm: (a) 12.2 kHz. (b) 17.9 kHz. (c) 42.7 kHz. (d) 90.9 kHz. (e) 95.0 kHz.

4.1.2 Characterization of mechanical eigenfrequencies of unpatterned membranes

The *homodyne detection* setup described in Fig. 3.1 was used for the mechanical characterization of the GaAs membranes. For each membrane, one records a spectrum similar to the one seen in Fig. 3.3, where the automated characterization procedure extracts all ω_m and Q_m within the specified frequency range. The FEM simulated and the measured ω_m of the first 5 mechanical eigenmodes are shown in Table 4.1. These data are of the same device geometry simulated in Fig. 4.2. We can see that the experimentally measured ω_m are significantly shifted to higher frequencies compared to the FEM simulations. The error in measurement is dominated by the minimum bandwidth of the spectrum analyzer = 1 Hz, and the FEM simulations are done with a precision of 1 Hz as well. Obviously, this experimental error margin does not take into consideration the fabrication errors and deviation from ideal design values.

In order to understand the origin of the mismatch between experimentally measured ω_m and simulations, we need to understand the way the FEM problem is set-up. The problem of finding the mechanical eigenfrequencies is only dependent on the speed of sound in medium v which is approximated by eqn 2.2. Thus, aside from the geometry and boundary conditions, the only two relevant physical parameters in the problem are E and ρ. Unfortunately, this is not enough to give the right values for ω_m. This is because stress in the fabricated structures plays an important role, and this is why the bulk value of E in GaAs fails to give the right answer. The approach suggested in [Rasmussen, 2013] is to use FEM to specify the mode shapes and the order of the eigenmodes. Once one of the modes is identified experimentally, the effective Young's modulus E' is estimated and plugged in the FEM to get the correct eigenfrequencies for all modes. One main assumption is that the stress distribution is isotropic, which is highly dependent on the geometry under investigation [Rasmussen, 2013].

Table 4.1: Eigenfrequenices of the first 5 modes in FEM simulations and experiment of a 70 μm $\times$ 40 μm simulated GaAs membrane with $h = 100$ nm, $t = 24$ μm and $b = 2$ μm. All data have an error of ± 1 Hz.

Mode number	FEM frequency (kHz)	Experimental frequency (kHz)
1	12.177	63.546
2	17.938	80.768
3	42.737	169.117
4	90.867	244.93
5	94.993	255.855

4.1.3 Mechanical mode tomography

4.1.3.1 Identifying the mode shapes

To get a deeper understanding of the experimentally measured eigenmodes, mechanical mode tomography was used to investigate the mode shapes of the eigenmodes of the 70 μm $\times$ 40 μm GaAs membrane; the technique was discussed in section 3.1.3. As shown in Fig. 4.3, the mode shapes of the eigenmodes (a-e) match the FEM simulations remarkably well. The order of different eigenmodes is also preserved except for the two modes with highest frequency shown in panels (d) and (e). FEM simulations showed their frequencies to be separated by 3 kHz only. In experiment, their order is reversed although they remain relatively close in frequency with only 11 kHz difference.

An interesting observation was the mode shown in Fig. 4.3f, which is at a frequency of 85.3 kHz, and it looks identical to the mode in Fig. 4.3b, which is at a frequency of 80.8 kHz. In theory, all mechanical eigenmodes are orthogonal to each other and it should not be possible for 2 eigenmodes to have the same mode shape. This case was found for the same mode shape in several measured samples. No valid hypothesis was found that could explain this experimental result.

4.1.3.2 Mode shape hybridization

For some of the measured devices, an interesting observation occurred: when two eigenmodes are close in frequency, it is observed that their mode shapes are distorted as seen in Fig. 4.4. The probed device has the same geometry as the device discussed so far, except for the tether position t, which is changed from $t = 24$ μm to $t = 18$ μm. One can see that the two pairs of modes (a, b) and (c, d), whose modes are separated by < 5 kHz, are skewed from the mode shapes seen in Figs. 4.3(a-d). This phenomenon was observed for two identical devices on two different chips.

By inspection, one can observe that the mode shapes appear to be a symmetric/asymmetric linear combination of the original mode shapes. Since each pair of modes are extremely close in frequency, one could hypothesize that mode coupling occurs. Coupling between different mechanical modes has been demonstrated in nanomechanical ring resonators, and it was systematically shown that two mechanical normal modes have an avoided crossing in frequency [Anetsberger et al., 2008]. Although the observation in our case appears to be consistent with that explanation, but it should be systematically studied by varying t in small steps on the fabrication mask, and then observe the frequency evolution of the two mechanical modes depending on t.

In similarity with the previous device, we observe this additional mode in Fig. 4.4f, which has the same mode shape as the one in 4.4a. On the contrary, the 2 modes are not successive in frequency, as a different mode exists in between.

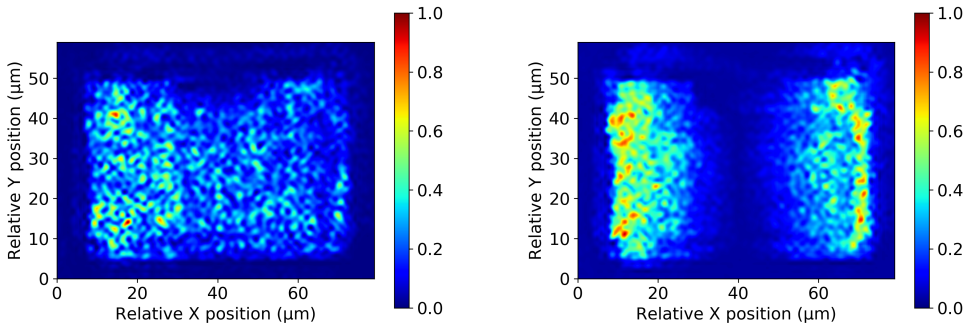

(a)

(b)

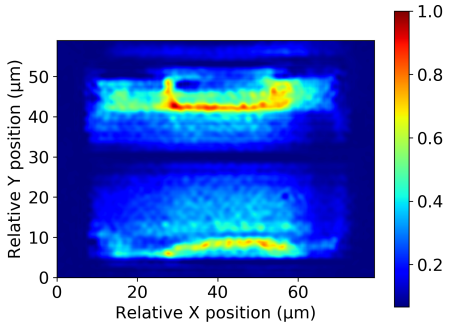

(c)

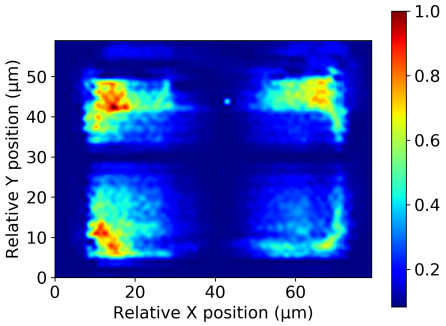

(d)

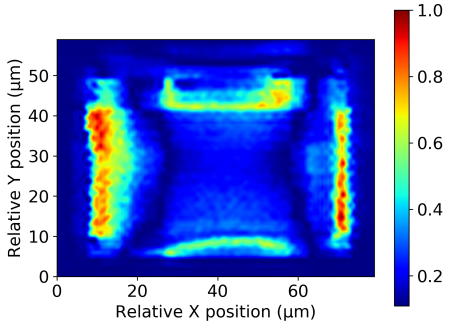

(e)

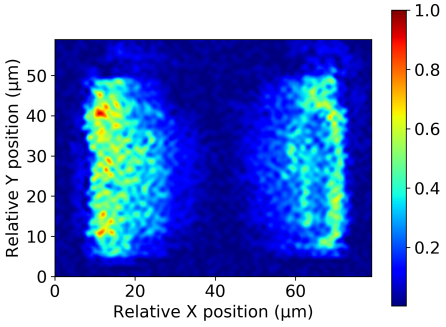

(f)

Figure 4.3: Mechanical mode tomography of a 70 μm $\times$ 40 μm GaAs membrane with $h = 100$ nm, $t = 24$ μm and $b = 2$ μm: (a) 63.5 kHz. (b) 80.8 kHz. (c) 169.1 kHz. (d) 244.9 kHz. (e) 255.9 kHz. (f) 85.3 kHz.

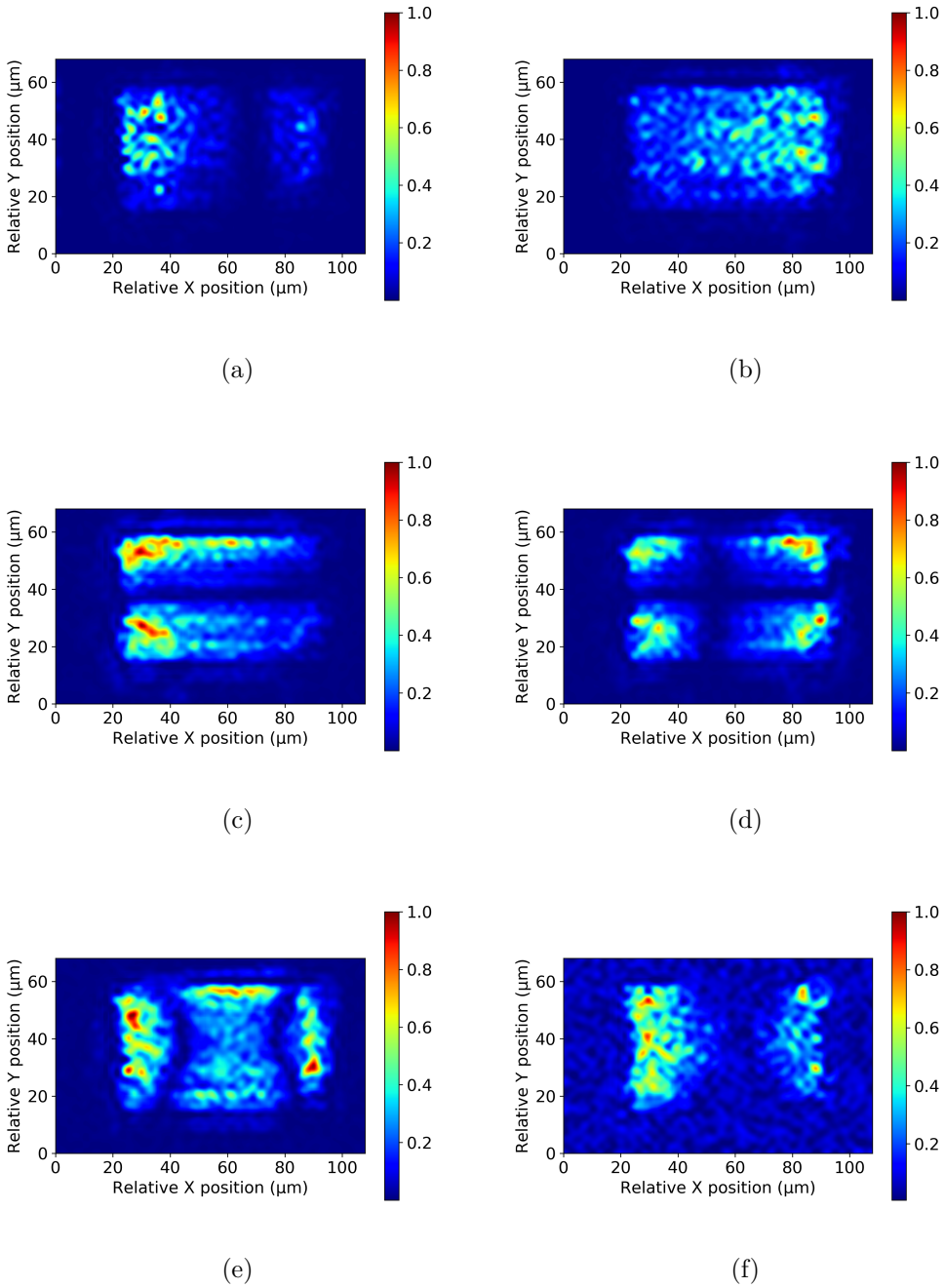

Figure 4.4: Mechanical mode tomography of a 70 μm $\times$ 40 μm GaAs membrane. The only geometrical difference with the device in Fig. 4.3 is that $t = 18$ μm: (a) 52.1 kHz. (b) 54.4 kHz. (c) 166.4 kHz. (d) 171.1 kHz. (e) 226.0 kHz. (f) 70.1 kHz. Mode hybridization is observed between the modes in panels (a, b), and also for the modes in panels (c, d).

4.1.3.3 Effective Young's modulus

Using mechanical mode tomography, it was possible to uniquely determine each eigenmode by comparing the mode shape to FEM simulations. As previously mentioned, if an eigenmode is uniquely determined in both experiment and simulations based on its mode shape, then the effective Young's modulus E' for that mode can be calculated as follows: Starting from the equation of the eigenfrequencies of a free-free beam, and assuming all other parameters in eqn 4.1 are constant. Therefore, $\omega_m \propto \sqrt{E}$. Thus:

$$\frac{E'}{E} = \left(\frac{\omega_{Exp}}{\omega_{FEM}}\right)^2. \tag{4.3}$$

Table 4.2 shows the eigenfrequenices of the first 5 experimental eigenmodes matched to the corresponding eigenfrequency in FEM based on their mode shape according to Figs. 4.2 and 4.3. Moreover, the square of the ratio between both is calculated. Using these ratios, one could change the value of E of GaAs in COMSOL according to eqn 4.3.

Table 4.3 shows the FEM eigenfrequencies when E is replaced by E' for the 5 modes according to eqn 4.3. The red-marked diagonal elements in Table 4.3 correspond to the eigenfrequency of a given mode for which E' was corrected. We can see that the diagonal elements remarkably agree with the experimental results. These observations are consistent with the way the FEM problem is set up. As previously mentioned, E and ρ are the only physical parameters in our problem aside from the geometry. Unfortunately in our case, this result is not satisfactory. As the scaling is mode dependent, and there is no one value of E' that could explain the shifting for all modes adequately.

In a previous work, Liu *et al* fabricated suspended GaAs membranes by sacrificial etching of AlGaAs layer. The geometry used is identical to the one that was analytically solved in section 2.1.1; that is a rectangular membrane with fixed boundaries.

Table 4.2: Eigenfrequenices of the first 5 experimental eigenmodes compared to the corresponding eigenfrequency in FEM based on their mode shape, and square the ratio between both columns. The device is a 70 μm × 40 μm simulated GaAs membrane with $h = 100$ nm, $t = 24$ μm and $b = 2$ μm. All data have an error of ±1 Hz.

N	FEM frequency (kHz)	Experimental frequency (kHz)	$\left(\frac{\omega_{\mathrm{Exp}}}{\omega_{\mathrm{FEM}}}\right)^2$
1	12.177	63.546	27.233
2	17.938	80.768	20.274
3	42.737	169.117	15.659
4	94.993	244.934	6.648
5	90.867	255.855	7.930

Table 4.3: Eigenfrequenices of the first 5 experimental eigenmodes when E is replaced by E' according to the ratios in the 1st row. The right-most column is the experimental eigenfrequencies. The device geometry is a 70 μm × 40 μm GaAs membrane with h = 100 nm, t = 24 μm and b = 2 μm. All data have an error of ±1 Hz.

$\left(\frac{\omega_{\text{Exp}}}{\omega_{\text{FEM}}}\right)^2$	27.233	20.274	15.659	6.648	7.930	NA
N	FEM (kHz)					Experiment (kHz)
1	63.546	54.829	48.185	31.396	34.290	63.546
2	93.608	80.768	70.981	46.249	50.512	80.768
3	223.03	192.43	169.120	110.19	120.35	169.117
4	495.72	427.72	375.90	244.93	267.50	244.934
5	474.19	409.14	359.57	234.29	255.88	255.855

To find a match between simulations and experiment, E was used as a fitting parameter. This allowed matching the frequencies of the modes within a 10% error range with a single fitting parameter for all modes [Liu et al., 2011] . This is in contrast to our observation, where there is not a single value for E' that could satisfactorily fit all the modes.

The conclusion drawn from this analysis is that the stress distribution in our membranes is highly anisotropic, which is potentially due to the different boundary conditions in our geometry. The anisotropic stress affects each mode differently, which means that the simple assumption in eqn 4.3 is not valid. Although the mode order is generally unchanged, except when the eigenfrequenices are very close to each other, but there is no single E' value that could effectively capture the stress induced frequency shift for all modes.

4.1.4 Characterization of mechanical eigenfrequencies of PhC patterned membranes

Similar to the mechanical characterization of un-patterned devices, PhC-patterned devices were characterized to extract ω_m and the mode shapes of each eigenmode. Fig. 4.5, shows the result of mode tomography of a 45 μm × 50 μm device. We notice that the same 5 eigenmodes appear in the same order as the un-patterned devices in Fig. 4.3. However, we notice that ω_m of each eigenmode is significantly lower than those seen in the un-patterned device. One has to keep in mind that this device has a smaller size compared to the un-patterned device. According to eqn 4.1, smaller membrane size should lead to higher frequencies. On the other hand, we observe the opposite.

To get a simple idea about the estimated ω_m for the membrane size, FEM simulations were used. However, the simulated membrane is un-patterned which could

lead to some deviations. Table 4.4 shows the FEM eigenfrequencies vs the experimental eigenfrequenices for the same geometry probed in Fig. 4.5. Similar to the un-patterned membranes, lower order modes are more shifted to higher frequencies compared to higher order modes. However, the ratio $\left(\frac{\omega_{\mathrm{Exp}}}{\omega_{\mathrm{FEM}}}\right)^2$ is more than a factor of 4 less for the PhC-patterned devices compared to the values in Table 4.2 for the un-patterned devices. Interestingly, the 5th eigenmode - the free-free mode - is shifted to lower frequenices in experiment compared to FEM. Such observations support the hypothesis that the nature of the stress in the membrane is highly anisotropic and that different eigenmodes are affected differently by the stress distribution. Moreover, it seems the etching of PhC holes partially relaxes the stress in the membrane leading to lower ω_m for the PhC-patterned devices.

Table 4.4: Eigenfrequenices of the first 5 experimental eigenmodes matched to the corresponding eigenfrequency in FEM based on their mode shape, and the ratio between both columns. The device geometry is a 45 μm $\times$ 50 μm simulated GaAs membrane with $h = 100$ nm, $t = 17$ μm and $b = 2$ μm. All data have an error of ± 1 Hz.

N	FEM frequency (kHz)	Experimental frequency (kHz)	$\left(\frac{\omega_{\mathrm{Exp}}}{\omega_{\mathrm{FEM}}}\right)^2$
1	12.700	32.041	6.366
2	24.076	44.040	3.345
3	39.882	76.164	3.648
4	109.530	121.060	1.211
5	210.440	151.980	0.521

4.1.5 Quality factor extraction

As discussed in section 3.1.1, *homodyne detection* can be used to measure the mechanical damping rate γ_m, which is used to calculate Q_m. Moreover, it was discussed that two different methods are used to measure γ_m in this thesis. Those are the Lorentzian fit method and the ringdown method.

Fig. 4.6a shows Q_m for different eigenmodes of un-patterned GaAs membranes having different geometries. We can observe that Q_m values are clustered into two regions. For low frequency modes, $Q_m > 10^4$ are achieved reaching a maximum value of $\approx 5 \times 10^4$. On the other hand, high frequency modes show an order of magnitude deterioration achieving $Q_m \sim 10^3$. If we compare the frequency ranges with the result of mechanical mode tomography, we notice that the high Q_m values are mainly achieved for two modes. Those are shown in Figs. 4.2a and 4.2b. To explain this observation, It is important to mention that the growth quality of the 100 nm GaAs layer was not optimal, and it had a surface roughness of more than 10 nm, especially on the bottom surface. One hypothesis to explain the clustering is that high order modes have more surface motion which could limit their Q_m because of surface losses. This effect is more significant for thin membranes; i.e. larger surface

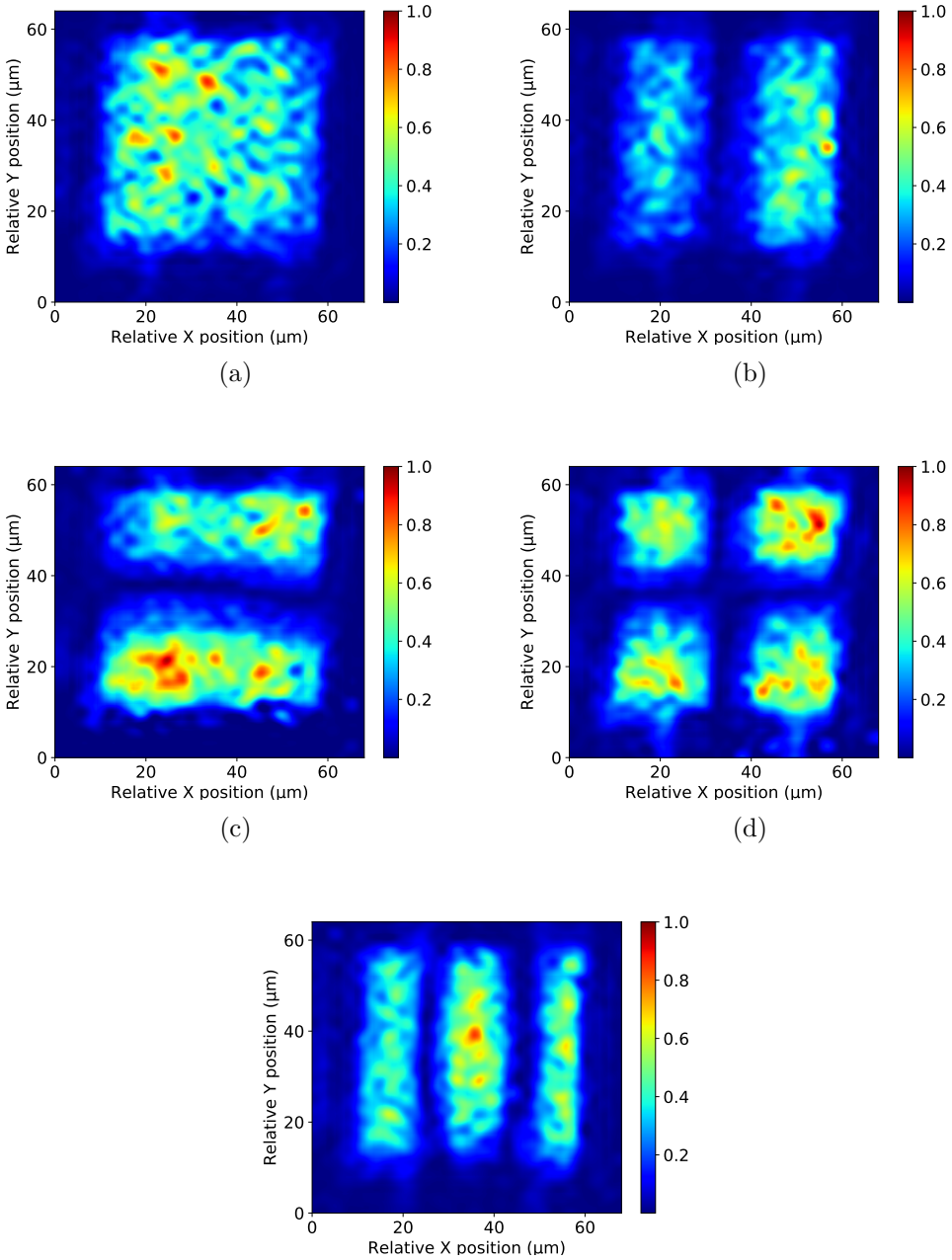

Figure 4.5: Mechanical mode tomography of a 45 μm × 50 μm PhC-patterned GaAs membrane with $h = 100$ nm, $t = 17$ μm and $b = 2$ μm: (a) 32.0 kHz. (b) 44.0 kHz. (c) 76.2 kHz. (d) 121.1 kHz. (e) 152.0 kHz.

to volume ratio [Imboden and Mohanty, 2014; Villanueva and Schmid, 2014]. To test this hypothesis, we needed to fabricate devices from a higher quality wafer, which was not possible in the time frame of this thesis.

Fig. 4.6b shows Q_m for different eigenmodes of PhC-patterned GaAs membranes having different geometries. In similarity with the un-patterned devices, the measured Q_m are clustered into 2 regions, where low frequency modes achieve $Q_m > 10^4$. The Q_m achieved are on average less than those for un-patterned devices, reaching a maximum value of $Q_m \approx 3 \times 10^4$. High frequency modes achieve $Q_m \sim 10^3$. The similar trend in un-patterned and PhC-patterned devices is not surprising, as both sets of devices were fabricated from the same wafer. However, it can be seen that PhC patterns do not severely deteriorate the mechanical properties of our membrane which is extremely important for the cavity optomechanical system.

The achieved Q_m values for our GaAs membranes are far from optimal. GaAs membranes with $Q_m > 10^6$ have been demonstrated [Liu et al., 2011]. To achieve ground state cooling for a mechanical mode at $T = 4$ K, we need to satisfy that:

$$Q_{initial} > \bar{n}_{initial}(T,\ \omega_m), \tag{4.4}$$

where $\bar{n}_{initial}$ is the initial phonon thermal occupation, which is given by:

$$\bar{n}(T, \omega_m) = \frac{1}{\exp\left(\frac{\hbar\omega_m}{k_B T}\right) - 1}, \tag{4.5}$$

the reasoning behind the above condition is that upon cooling, γ_m increases linearly by decreasing $\bar{n}(T, \omega_m)$. Thus, Q_m decreases till it reaches a minimal value of 1, and then we would have an overdamped mechanical system. Therefore, the above condition needs to be fulfilled to avoid reaching the overdamping regime. If we assume a mechanical mode with $\omega_m = 2\pi \times 100$ kHz. Then at 4 K, $Q \sim 10^6$ is needed to cool the resonator to its quantum mechanical ground state.

To check that the achieved Q_m is not limited by the viscous damping. i.e. the damping due to interaction with gas molecules of the surrounding medium, the Q_m of an un-patterned memrbrane is measured at different pressure P values. Fig. 4.7 shows pressure dependent Q_m measurements of a 100 nm thin 70 μm $\times$ 40 μm GaAs membrane. We can see that Q_m starts to saturate at $P < 1 \times 10^{-4}$ mbar. Mechanical characterization is normally done in a vacuum chamber at $P = 1 \times 10^{-5}$ mbar, which shows that viscous damping is negligible in our case. Thus, the inferior performance of our membranes is mainly attributed to the quality of the wafer used in the fabrication process. Fabrication of new devices with higher quality wafer is the next step in the path to achieve $Q_m > 10^6$.

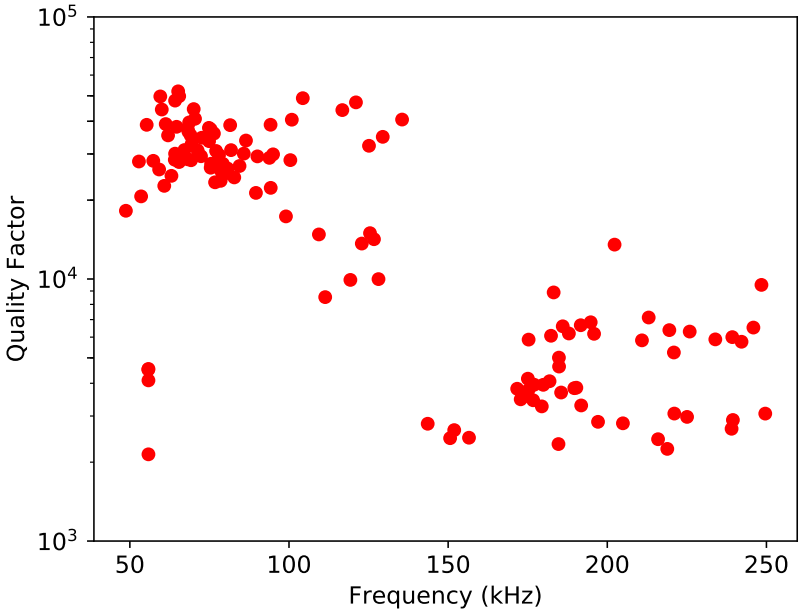

(a)

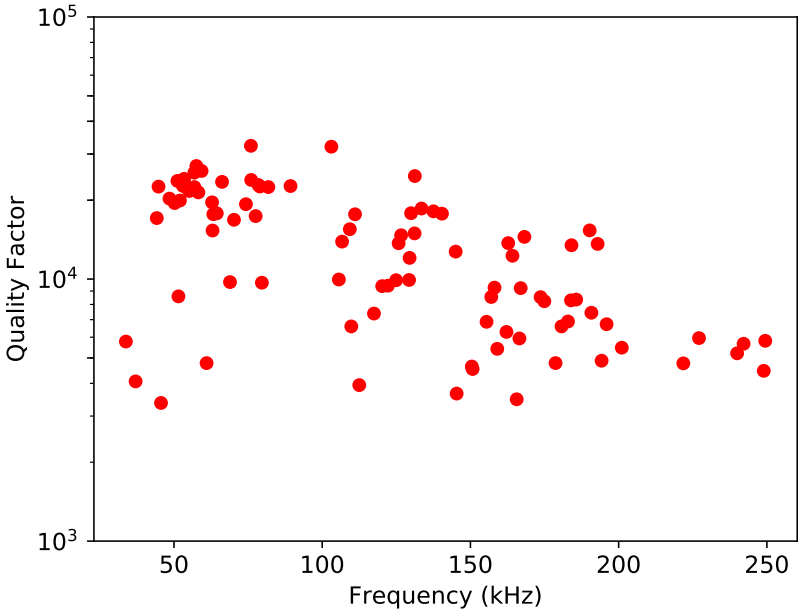

(b)

Figure 4.6: Quality factor of different mechanical eigenmodes for: (a) un-patterned membranes. (b) PhC-patterned membranes.

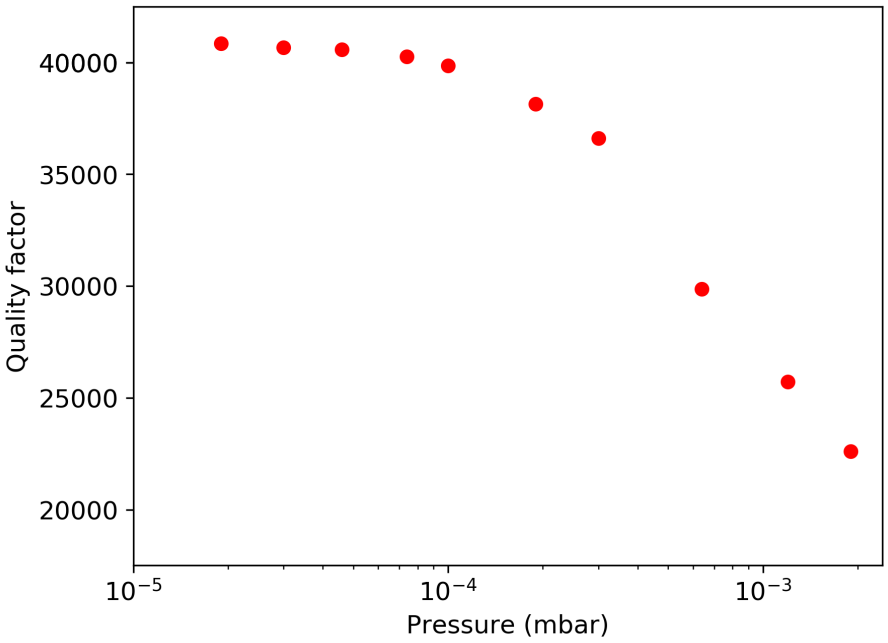

Figure 4.7: Quality factor of an un-patterned membrane at different chamber pressure.

4.2 Optical characterization

4.2.1 Photonic crystal slab design

The PhC pattern was designed using COMSOL multiphysics software by Jamie Fitzgerald from the group of Associate Professor Philippe Tassin at Chalmers physics department. The characteristic dimensions of the membrane are shown in Fig. 2.6. The membrane has a thickness $h = 100$ nm, period of hole structure a and hole radius r. The refractive index n of GaAs was taken to be 3.374 at 1550 nm, while the etched holes have the refractive index of vacuum ($n = 1$). Fig. 4.8 shows the reflectivity spectrum of GaAs PhC slab for a plane wave at normal incidence as a function of r and a values. The values of r and a are normalized by the wavelength. This is due to the scale invariance property of Maxwell's equations, which makes it preferable to work with normalized units. It can be clearly seen that for certain r and a values, the reflectivity R of the GaAs membrane approaches unity. We decided to fabricate devices with $r = 418$ nm and $a = 1081$ nm to give maximum reflectivity at the telecommunication wavelength ($\lambda = 1550$ nm). This (r, a) pair lies at the intersection of the dashed black lines in Fig. 4.8.

Fig. 4.9 shows the reflectivity spectrum for $r = 418$ nm and $a = 1081$ nm simulated by S^4 software package. We can observe that $R \approx 1$ is achieved at 1550 nm, and that $R > 99\%$ is maintained in a narrow wavelength window ~ 16 nm. Throughout

this section, S^4 package will be used to compare the experimental results of different investigated structures to simulations.

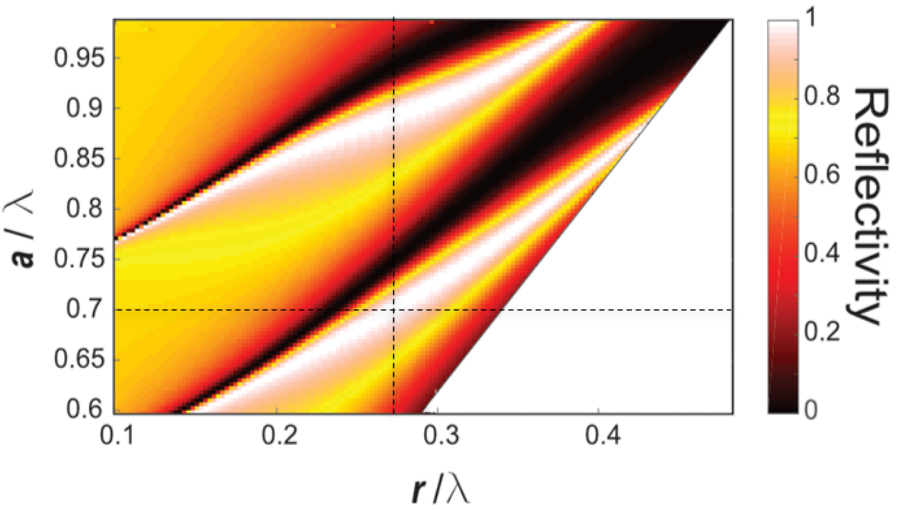

Figure 4.8: Reflectivity of a 100 nm thin GaAs PhC slab as a function of different r and a values. The intersection point represents the chosen (r, a) pair for the fabrication of high reflectivity membranes. Courtesy of Jamie Fitzgerald, Chalmers (Unpublished).

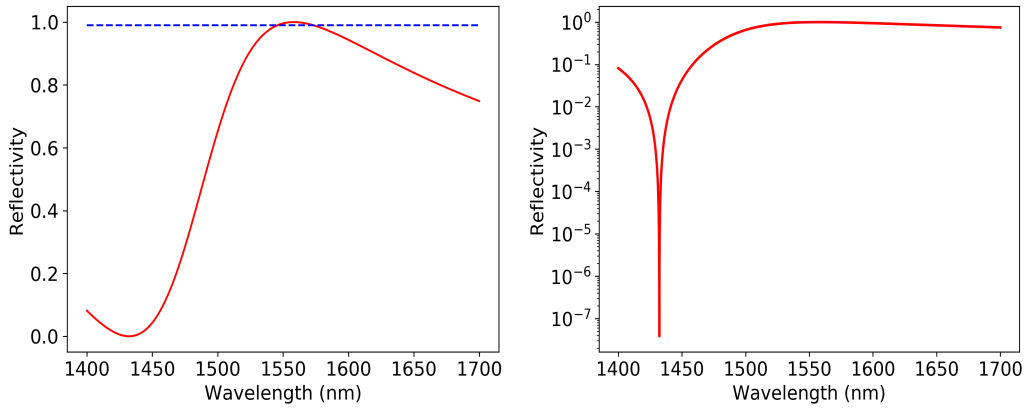

(a) (b)

Figure 4.9: Reflectivity spectrum of a 100 nm thin GaAs PhC slab for $r = 418$ nm and $a = 1081$ nm using S^4 software package. (a) Linear scale, the dashed blue line is for $R = 0.99$. (b) Logarithmic scale.

4.2.2 Fabricated GaAs membranes

The fabrication of GaAs membranes was done in Chalmers university MC2 cleanroom by Sushanth Kini. Examples of released GaAs membranes are seen in Fig. 4.10, where we can see SEM images of both PhC-patterned and un-patterned devices. It is important to note that the membranes are separated from the GaAs

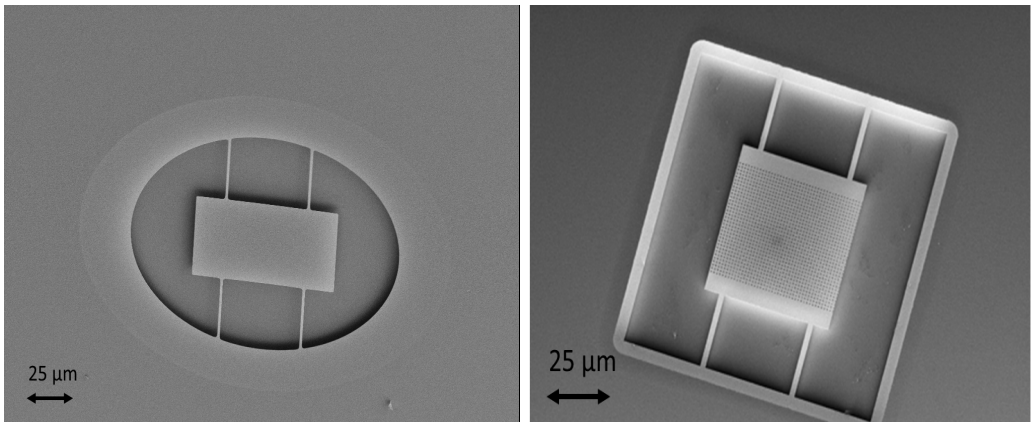

(a) (b)

Figure 4.10: (a) SEM image of PhC patterned GaAs membrane. (b) SEM image of un-patterned GaAs membrane.

susbtrate by a 4 μm air gap. This will be important to consider in our modeling, as this geometry forms a Fabry-Pérot cavity which contributes to the measured reflectivity spectrum, a topic that was discussed in section 2.2.

The design parameters for maximum reflectivity at 1550 nm are $r = 418$ nm and $a = 1081$ nm. However, errors in the microfabrication process can lead to deviation from these values. Therefore, the mask was designed with 3 different PhC parameters as shown in Table 4.5. If there was a systematic shift in the sample fabrication, then one of the designed PhC patterns would closely match the desired values. In addition, un-patterned devices were also fabricated as the one shown in Fig. 4.10b. Fig. 4.11 shows SEM pictures for the patterned GaAs membranes with different r values. Since r values are highly susceptible to variation during the etching process, images of several membranes with different PhC parameters were processed by the image processing software (ProSEM). The extracted r values are given in Table 4.6. Mean r values show less than 3 nm variation for devices having the same PhC pattern. The deviation of the mean r values from the design value is also within the standard deviation. This shows that the fabricated PhC pattern closely match the design parameters we aimed for.

Table 4.5: r and a parameters of PhC patterns used in the fabrication of high reflectivity GaAs membranes.

Photonic crystal	r (nm)	a (nm)
PhC1	410	1081
PhC2	418	1081
PhC3	427	1081

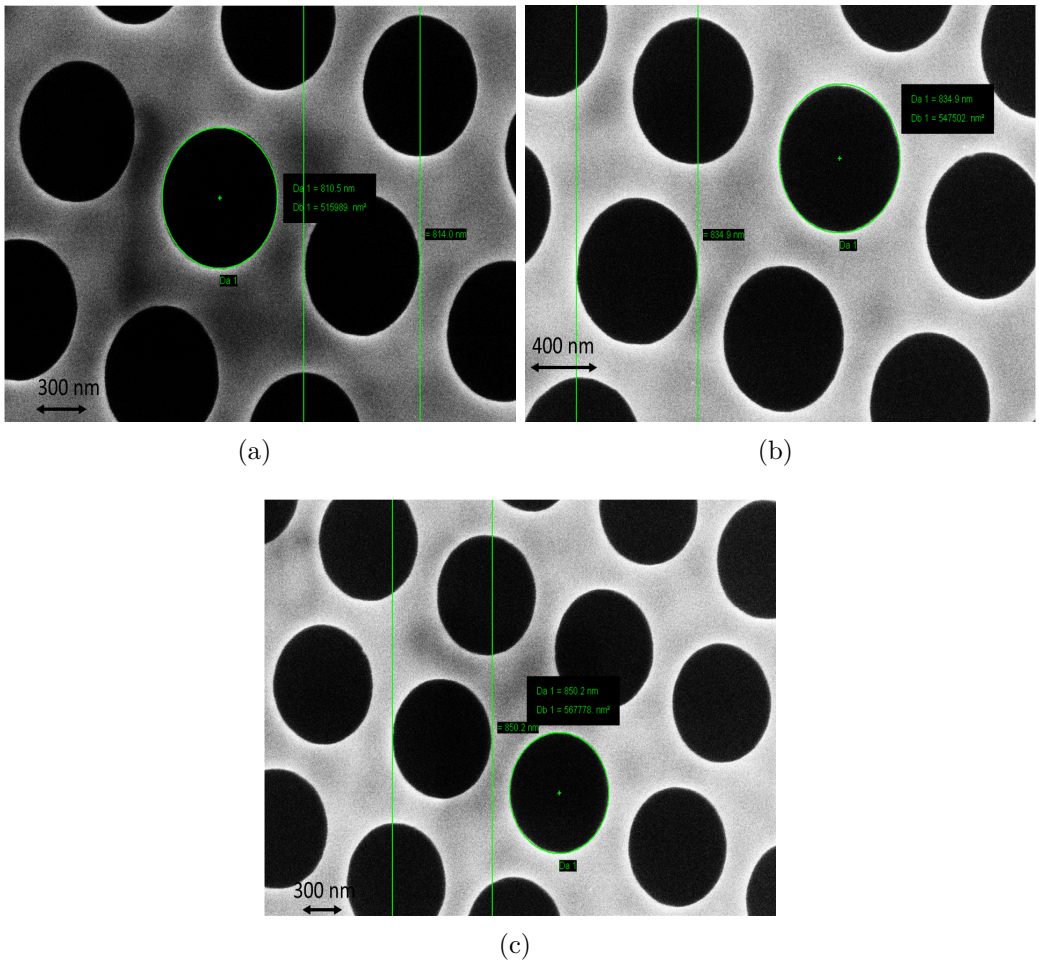

(a) (b)

(c)

Figure 4.11: SEM images of PhC-patterned GaAs membranes with different r parameters: (a) $r = 418$ nm. (b) $r = 410$ nm. (c) $r = 427$ nm.

Table 4.6: Extracted r values from different devices with different PhC patterns.

Photonic Crystal	Device 1 (nm)	Device 2 (nm)	Device 3 (nm)	Device 4 (nm)
PhC1	412.1 ± 2.2	412.4 ± 2.4	413.6 ± 2.0	412.1 ± 4.0
PhC2	419.2 ± 1.9	417.9 ± 3.0	419.3 ± 1.3	418.5 ± 1.7
PhC3	425.0 ± 1.9	427.5 ± 3.7	425.3 ± 2.1	425.1 ± 2.1

4.2.3 Reflectivity of MBE grown GaAs wafer

The first measurements were done on an unprocessed part of the wafer. As seen in Fig. 4.12, the wafer is composed of a multi-layer stack. 100 nm GaAs layer is grown on a 4 μm $Al_{0.65}Ga_{0.35}As$ layer. Both layers are grown by molecular beam epitaxy on a 350 μm GaAs substrate. As a result, the measured reflectivity spectrum is not flat as a function of wavelength due to interference effects. Fig. 4.13 shows the reflectivity spectrum measured using the custom built optical reflecivity setup discussed in section 3.2. We can notice two important features in the experimental

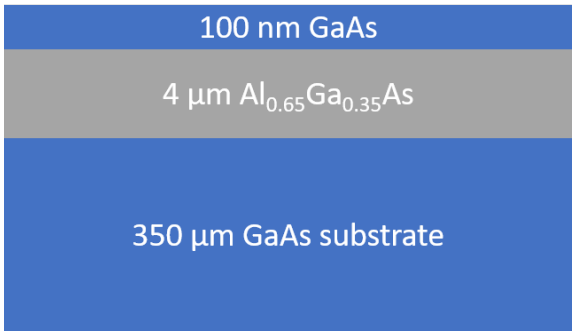

Figure 4.12: Schematic of the unprocessed wafer. It consists of 100 nm GaAs layer grown on 4 μm $Al_{0.65}Ga_{0.35}As$ layer. Both layers were grown by molecular beam epitaxy on a 350 μm GaAs substrate.

data. Firstly, the reflectivity spectrum has a slow modulation of ∼100 nm free spectral range ($\Delta\lambda$), where R varies between 24% and 36%. Secondly, the reflectivity spectrum has a fast modulation $\Delta\lambda \sim 1$ nm, where R varies within $\sim 4\%$. One can intuitively understand this modulation if one assumes that each layer acts as a Fabry-Pérot cavity with a certain $\Delta\lambda$. Since:

$$\frac{\Delta\lambda}{\lambda} = \frac{\Delta\nu}{\nu}, \tag{4.6}$$

one could combine this with eqn 2.22 to find:

$$\Delta\lambda = \frac{\lambda^2}{2nL}, \tag{4.7}$$

where c is the speed of light in vacuum, n is the refractive index of the medium and L is the layer thickness. Table 4.7 shows the estimated $\Delta\lambda$ for each layer in the stack according to eqn 4.7.

The 100 nm thin GaAs layer has a $\Delta\lambda \approx 3564$ nm $\gg$ the laser tuning window = 110 nm. On the other hand, The AlGaAs layer has nearly the same modulation $\Delta\lambda \approx 100$ nm as the slow modulation we see experimentally. Finally, The GaAs substrate gives $\Delta\lambda \approx 1$ nm which matches the fast oscillation. One way to model this multilayer stack, is through the transfer matrix method [Saleh and Teich, 2007]. Transfer matrix method relates the reflection and transmission coefficients of a multilayer stack based on the refractive index and thickness of each layer. Fig. 4.13 shows that the model matches nicely the experimental data. It is important to note that to match the dip position, L_{AlGaAs} was tuned to be 4.125 μm, which may be attributed to growth inaccuracy. The 1 nm oscillation is not present in the model as the substrate is treated as semi-infinite. The reason for this treatment is that the back surface of the wafer is extremely rough, which leads to excessive scattering and intensity loss. This contradicts with the basic assumption that the stack has perfectly flat layers. It is possible to effectively capture the scattering by adding an imaginary part to the refractive index, but in this case, the losses are used as a fitting parameter which does not increase our understanding of the problem. In

conclusion, the back reflection from the GaAs substrate contributes to the reflectivity spectrum, and appears as a fast modulation. This contribution will be seen in all optical reflectivity measurements.

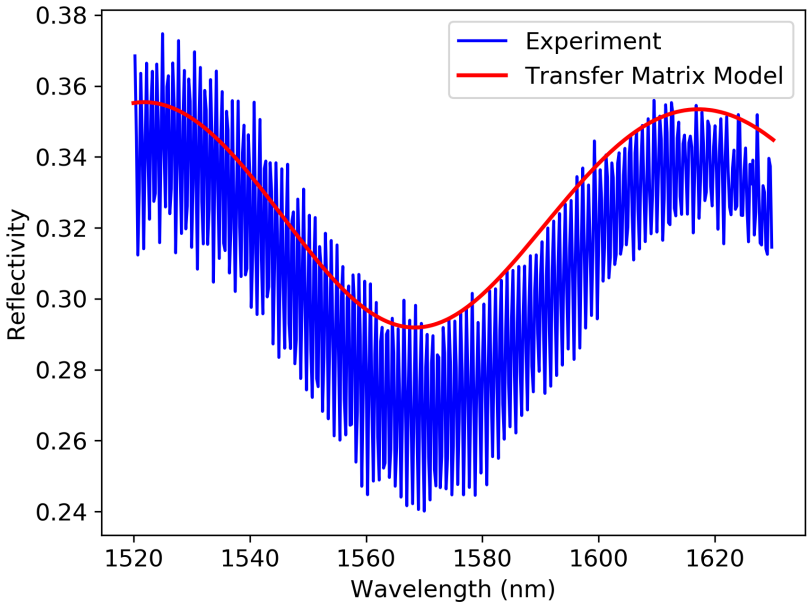

Figure 4.13: Reflectivity spectrum of unprocessed GaAs wafer vs transfer matrix model for the same stack but with a semi-infinite substrate.

Table 4.7: Free spectral range of different layers in the unprocessed GaAs wafer.

Material	L (μm)	n	$\Delta\lambda$ (nm)
GaAs	0.1	3.3702	3564.33
$Al_{0.65}Ga_{0.35}As$	4	3.0543	98.32
GaAs	350	3.3702	1.02

4.2.4 Reflectivity of un-patterned GaAs membranes

After understanding the reflectivity spectrum of the unprocessed wafer, the next step was to characterize GaAs membranes. Firstly, the un-patterned devices were characterized and analyzed. The motivation was that un-patterned devices are much simpler to understand and model using transfer matrix method, unlike PhC structures which are much more complicated to model. Fig. 4.14 shows the stack under investigation; a released 100 nm GaAs membrane separated from the GaAs substrate by a 4 μm air gap.

The experimental reflectivity spectrum of un-patterned GaAs membrane is shown in Fig. 4.15. R approaches 90%, which is due to the constructive interference of the multi-layer stack. This is in contrast to having a 100 nm thin GaAs membrane

surrounded by vacuum - the green line -, which would give $R = 68.3\%$ at 1550 nm with relatively small wavelength dependence. The transfer matrix model was used to fit two parameters: L_{GaAs} and L_{gap} using Matlab. It can be seen that the fitting matches closely the experimental data. The fitted values are: $L_{GaAs} = 85.1 \pm 2.0$ nm, and $L_{gap} = 4220.0 \pm 5.0$ nm. These numbers deviate from the growth thickness, but as previously mentioned, the processed wafer had a large variation in the thickness of the top layer. The L_{GaAs} extracted from optical ellipsometry measurement was ≈ 87 nm, which matches the estimated value from the optical reflectivity spectrum. Compared to Fig. 4.13, the dip in the reflectivity spectrum is out of the tuning window of our laser. Moreover, high frequency modulation is superimposed on our curve. This is due to the contribution from the 350 μm GaAs substrate.

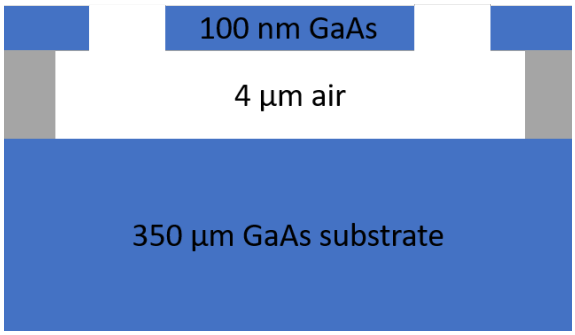

Figure 4.14: Schematic of a released 100 nm thin un-patterned GaAs membrane.

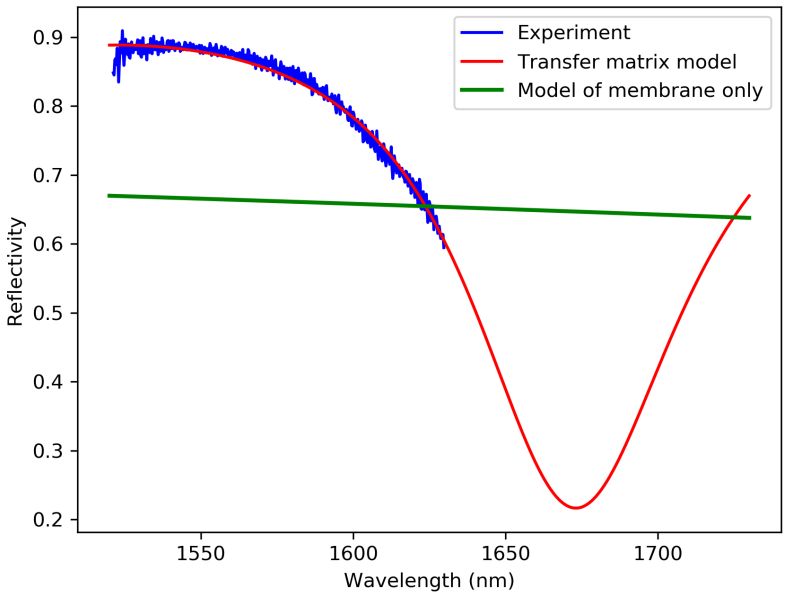

Figure 4.15: Reflectivity spectrum of un-patterned GaAs membrane vs transfer matrix model with a semi-infinite GaAs substrate.

4.2.5 Reflectivity of PhC-patterned GaAs membranes

To measure the fabricated GaAs PhC membranes, the optical reflectivity measurements were done in the same fashion. Fig. 4.16 shows the reflectivity spectrum for PhC-patterned GaAs membranes with the design parameters in Table 4.5. There are two main features that can be seen in this plot. Firstly, $R > 98\%$ is achieved for devices with $r = 410$ nm and $r = 418$ nm, which occurs at $\lambda = 1520$ nm. Reflectivity spectrum appears to be monotonically increasing towards shorter wavelength beyond our experimentally accessible range. Secondly, a sharp asymmetric dip appears, which shifts to shorter wavelength by increasing r.

The first hypothesis about the dip was that it occurred due to the multi-layer stack below the GaAs membrane in a similar fashion to the one seen in Fig. 4.15 due to the wafer structure shown in Fig. 4.14. S^4 software was used to simulate the spectral response of the whole stack with $L_{gap} = 4000$ nm and $L_{GaAs} = 100$ nm, and compare it to the response of a PhC slab with the parameters of PhC1 in Table 4.5 without taking the other layers into account. The plots can be seen in Fig. 4.17. In the region of maximum reflectivity, the multi-layer stack does not strongly affect the reflectivity value. Intuitively, as the reflectivity of the top membrane approaches 1, less light is coupled to the layers beneath. Thus, interference effects become less significant. At $\lambda \approx 1600$ nm, A resonance dip appears. However, this resonance dip can not explain the dip in the measurement in Fig. 4.16. The FWHM of the simulated dip is of the order of tens of nm. On the other hand, the measured dip

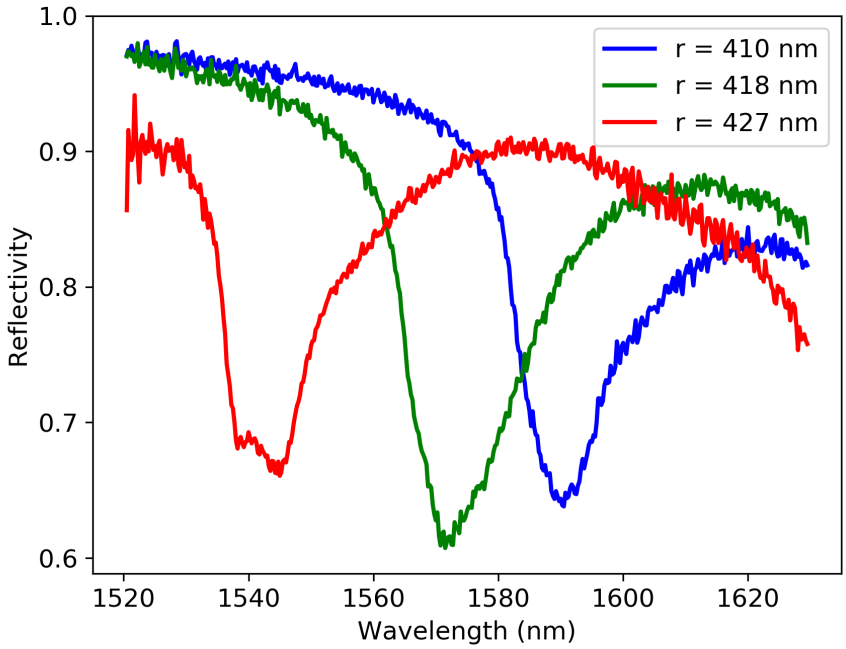

Figure 4.16: Reflectivity spectrum of 100 nm thin PhC-patterned GaAs membranes with PhC parameters given in Table 4.5.

is much sharper of the order of 10 nm. Another reason to reject this hypothesis is that these membranes were fabricated from the same wafer of the un-patterned membranes. If the dip was due to the multi-layer stack, the dip position would have been independent from the PhC pattern, and it would have occurred at the same position as the un-patterned devices. However, the reflectivity measurements of un-patterned devices shown in Fig. 4.15 show that the dip in the spectrum is beyond our laser tuning range (> 1630 nm), and Fig. 4.16 shows large dependence of the dip position on the PhC pattern within our tuning window.

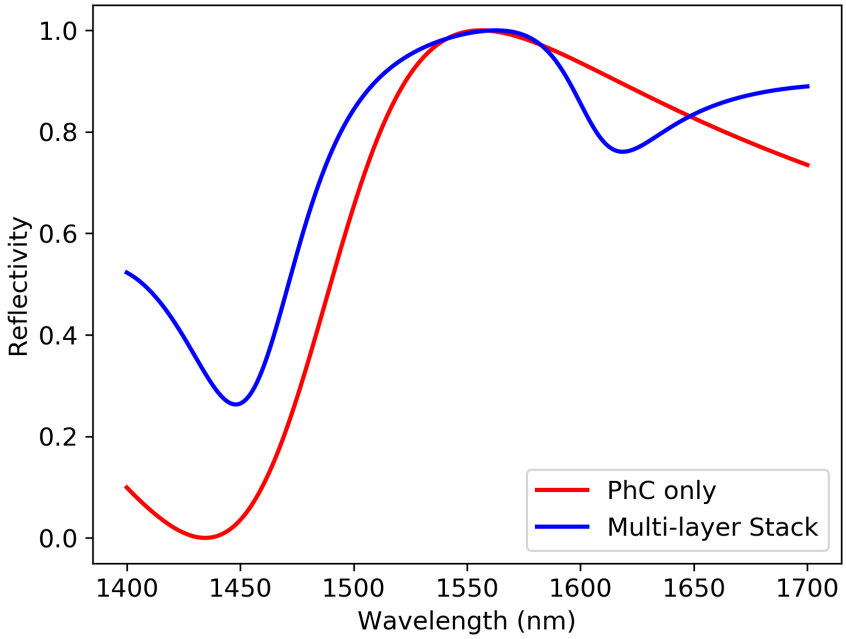

Figure 4.17: Reflectivity spectrum of a PhC-patterned membrane with $r = 418$ nm and $a = 1081$ nm in vacuum vs reflectivity spectrum of the same membrane but followed with 4 μm air gap and a semi-infinite GaAs substrate.

4.2.6 Beam-waist dependent measurements

The dip observed in reflectivity measurements of PhC membranes did not correspond to what the simulations had shown so far. Therefore, we started to question the different assumptions in our simulations and compare them to what was being done in experiment. One fundamental difference between simulation and experiment, is that the simulations shown in Figs. 4.8 and 4.9 are done for plane waves at normal incidence. On the other hand, the membranes are probed with a focused laser beam with a certain beam waist w_0 as shown in Fig. 4.18. The beam waist is given by eqn 2.40 for focusing a collimated Gaussian beam. It depends on the ratio of the lens focus and the input laser beam diameter. Thus, by increasing the focal length, w_0 increases. At the position of the beam waist of a Gaussian beam, around 86%

of the beam power lies in a circle with radius w_0, and about 99% of the power lies in in a circle with radius 1.5 w_0 [Saleh and Teich, 2007]. Normally in our setup, $w_0 \approx 4.2$ μm is used, which is around an order of magnitude smaller than the smallest membrane dimension (40 μm). This is to ensure that almost all the laser power falls on the membrane and to minimize clipping losses. i.e. minimize the power lost because of not hitting the membrane.

Fig. 4.19 shows the w_0 dependent measurements for a 50 μm $\times$ 40 μm membrane. We can observe that the reflectivity spectrum changes dramatically depending on w_0. There are three main features we can see in these plots:

1. The maximum reflectivity achieved is reduced for larger w_0.

2. The λ at which the dip occurs shifts to shorter wavelength for larger w_0.

3. The linewidth of the dip is reduced for larger w_0.

The reduction in the maximum reflectivity can be attributed to clipping losses. As shown in Fig. 4.18, as w_0 increases, more power is clipped because it does not probe the membrane. The dashed lines in Fig. 4.19, are the estimated clipping losses $L_{clipping}$ for each w_0 according to:

$$L_{clipping} = 1 - \mathrm{erf}\left(\frac{\sqrt{2}W}{2w_0}\right)\mathrm{erf}\left(\frac{\sqrt{2}L}{2w_0}\right), \tag{4.8}$$

where erf (x) is the error function. The calculation is done for a 50 μm $\times$ 40 μm membrane. The trend in Fig. 4.19 follows the experimentally measured reduction in maximum reflectivity, although the estimated losses are significantly less than the reduction in reflectivity. However, the estimated clipping losses are a minimum value assuming w_0 is exactly centered, and assuming no mis-alignment is present. The deviation from the theoretically estimated value is attributed to those reasons.

Since the simulations did not take into account that Gaussian beams are used to probe the devices, thus it was hypothesized that this parasitic feature is due to probing the PhC slab with a Gaussian beam. To test this hypothesis, it was decided to use S^4 software to model the experimental results.

4.3 Interaction of a Gaussian beam with a photonic crystal slab

4.3.1 Reflectivity spectrum of plane waves at tilted incidence

To reconstruct the Gaussian beam reflectivity spectrum, plane waves at different tilt angles were simulated for a PhC slab with $r = 418$ nm and $a = 1081$ nm according

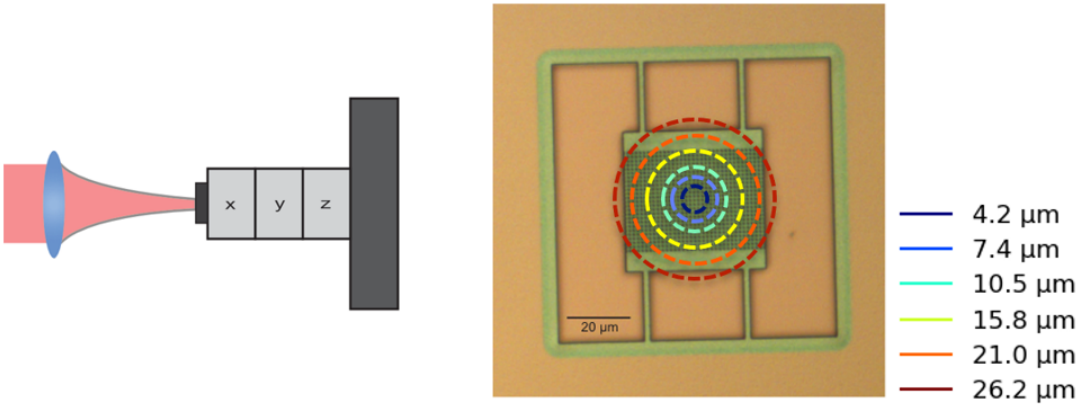

Figure 4.18: (left) A schematic of the focusing lens and the chip mounted on xyz stage, the lens focuses the laser beam on one membrane with w_0 depending on the focus on the lens. (right) An optical microscope image of a 40 μm × 40 μm PhC-patterned device, the dotted circles correspond to beam diameter ($2w_0$) in μm, the legend shows the corresponding w_0 values. - circles are drawn to scale -.

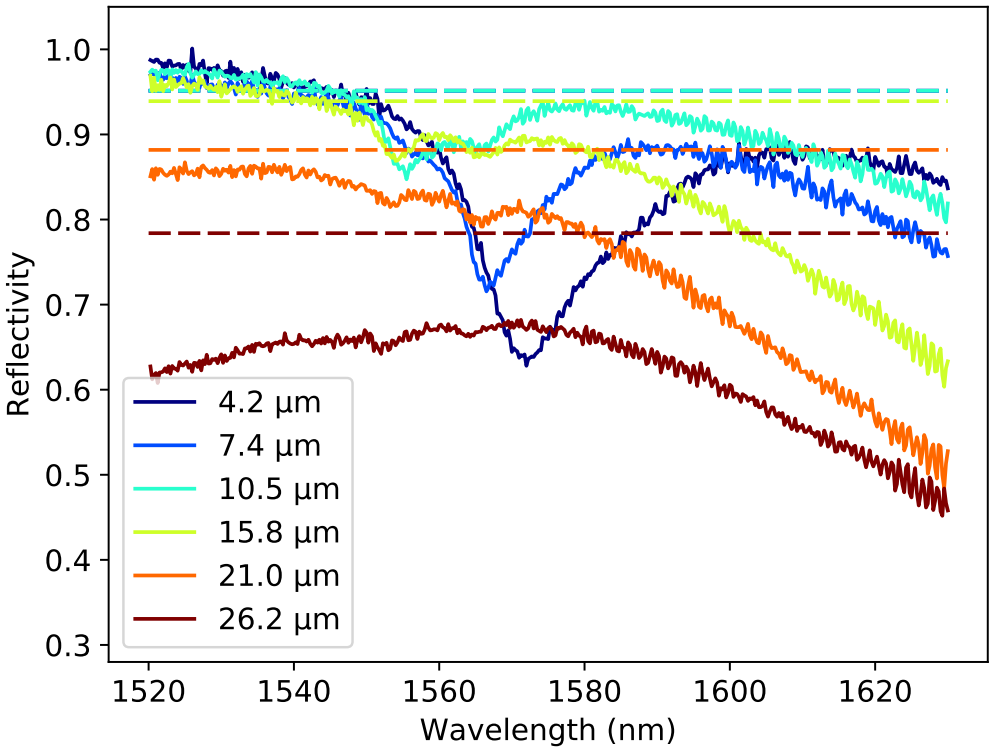

Figure 4.19: Reflectivity spectrum for different w_0 in μm. The dashed lines represent the estimated clipping losses for each w_0. The clipping loss lines for the $w_0 = 4.2$ μm and $w_0 = 7.4$ μm beams are almost identical to the $w_0 = 10.5$ μm due to negligible losses. The device is patterned with $r = 418$ nm and $a = 1081$ nm.

to the methodology presented in section 2.5.3. Fig. 4.20b shows the reflectivity spectrum between 1550 nm and 1700 nm for different polar angles ϕ at an azimuthal angle $\theta = 0°$, the coordinate system can be seen in Fig. 4.20a. We can see that for normal incidence, the curve is smooth. However, sharp resonance initially appears at $\lambda \approx 1653$ nm for $\phi = 1°$. The resonance shifts to longer wavelength by increasing ϕ, and the linewidth increases.

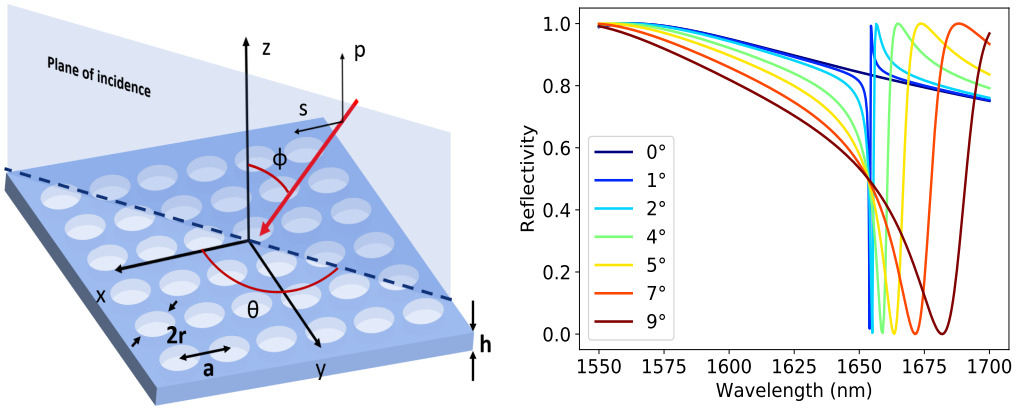

(a) (b)

Figure 4.20: (a) Plane wave incident on a PhC slab in spherical coordinates system. (b) Reflectivity spectrum for plane waves incident with different polar angles ϕ in degrees at azimuthal angle $\theta = 0°$. The polarization of each wave is aligned for the s-polarized beam case.

4.3.2 Comparison of simulation and experiment

Eqn 2.43 reconstructs the reflectivity spectrum of a Gaussian beam with a certain w_0 from the plane wave reflectivity spectra. Fig. 4.21 shows the result of the simulations for the same w_0 as those in the experimental results in Fig. 4.19. The simulations shown here are for the s-polarized beam case. However, it shall be proven that a p-polarized beam has an identical response.

By comparing Figs. 4.21 and 4.19, it is possible to interpret the w_0 dependent measurements. Considering the resonance linewidth and position, by integrating over the different plane wave components in Fig. 4.20, an asymmetric resonance dip would appear. The linewidth of the dip highly depends on the tilt angle. As it was discussed in Fig. 2.10, for small w_0, the integration incorporates more tilt angles, and hence the linewidth is wider and shifted to longer λ. On the contrary, large w_0 incorporates less tilt angles. Thus, the resonance is sharper and shifted to shorter λ. This trend can be clearly seen in the experimental data in Fig. 4.19. Moreover, for the smallest w_0, the reflectivity value achieved at the resonance condition is consistent with the experimental value.

Fig. 4.22 compares the relative shift of the dip position in theory and experiment.

The shift is done relative to the dip position at $w_0 = 4.2$ μm for each sample. We can see that the same trend is observed in theory and experiment. The shift increases significantly for small w_0, and saturates at longer w_0. However, the relative shift strongly differs from one sample to the other. The reason for this variation probably lies in the alignment of the device during measurement. Gaussian beam reconstruction assumes the sample is at the beam waist position and under normal incidence. This is complicated to control experimentally, and one can intuitively see that the averaging over all resonances will strongly depend on the tilt angle.

For the differences between simulation and experiment, firstly, the maximum reflectivity in simulations does not decrease with increasing w_0. This is due to the fact that the S^4 simulations assumes infinite periodicity in the xy plane, while the reduction in reflectivity is due to clipping losses. Secondly, the resonance dip in simulations gets sharper but it does not vanish. However, in experiment it vanishes for large w_0. This is can be explained by noting that S^4 simulates a perfect lattice, but in reality our slab has imperfections which reduces the quality factor of the guided resonance modes in PhC slabs. Finally, the resonance dip appears to be shifted by about 100 nm to longer wavelength compared to experiment. To explain this shift, we recall that in section 4.2.4, the reflectivity of un-patterned membranes were used to fit the thickness h of the slab, which was estimated to be around 85 nm. Moreover, characterization techniques like ellipsometry and SEM showed that h has a large variation of the same order. To study the effect of h, the previous simulations was repeated for a membrane with $h = 90$ nm. Fig. 4.23 shows that by reducing h from 100 nm to 90 nm, the resonance dip shifts by 50 nm to shorter wavelength. Therefore, the mismatch in λ is attributed to the variation in our membrane thickness from its ideal value of 100 nm.

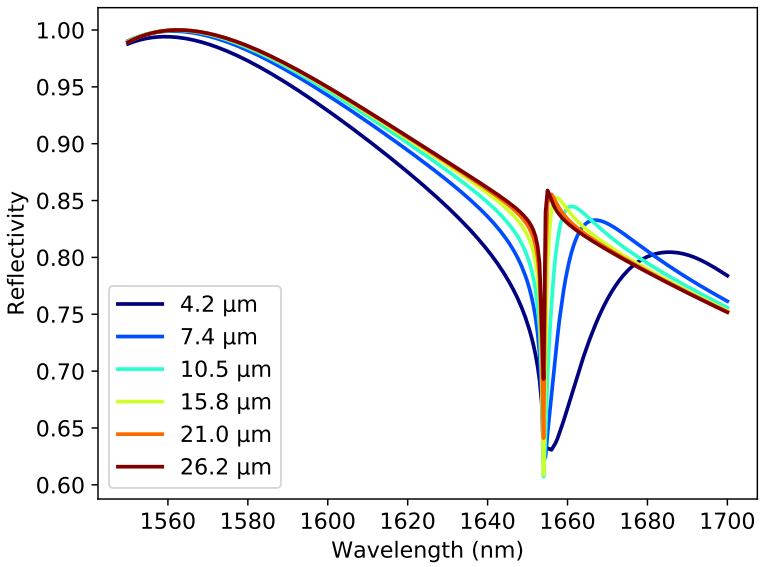

Figure 4.21: Reflectivity simulations of an s-polarized Gaussian beam with different w_0.

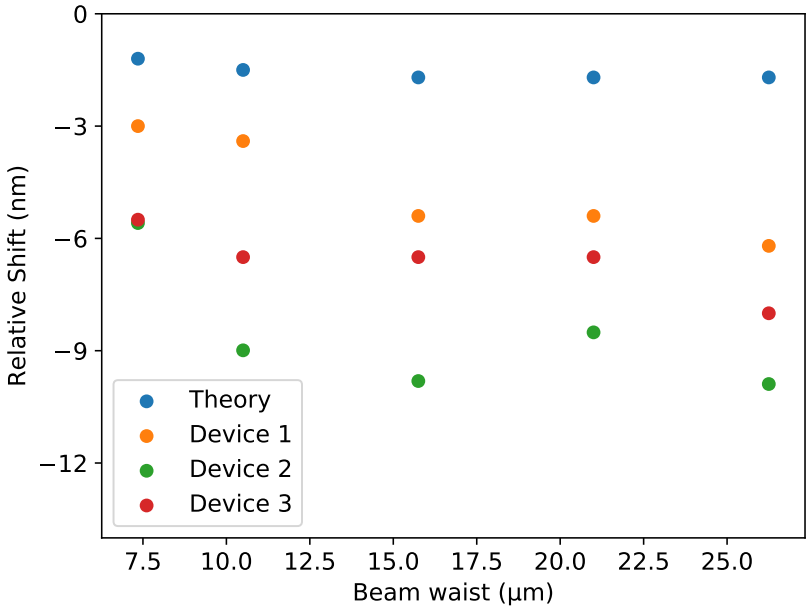

Figure 4.22: Shift of the dip position at different beam waists w_0 relative to its position at $w_0 = 4.2$ μm.

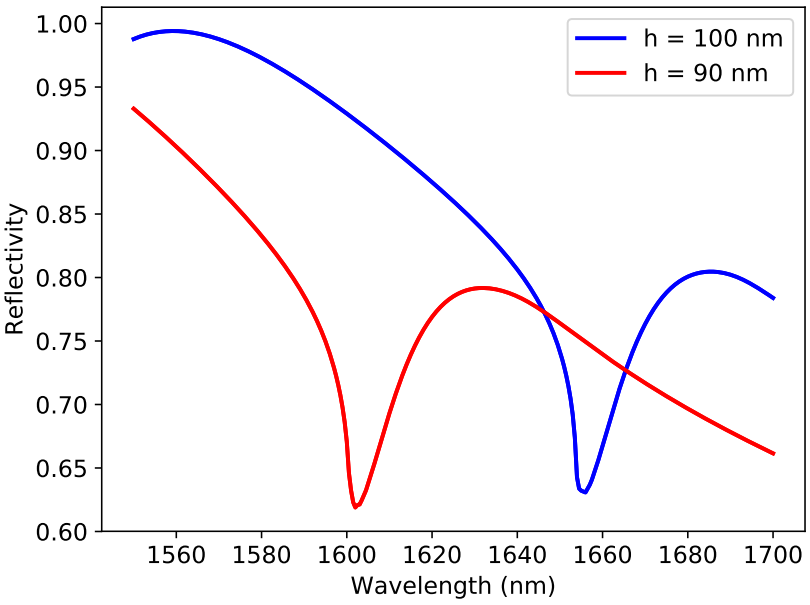

Figure 4.23: Reflectivity simulations of an s-polarized Gaussian beam with $w_0 = 4.2$ μm for different slab thickness h.

4.3.3 Resonance dependence on photonic crystal parameters

Our experimental data showed a clear dependence of the resonance position on the PhC parameters as it was shown in Fig. 4.16. To study the origin of this dependence, the simulations were repeated for different PhC parameters given by Table 4.5. Fig. 4.24 shows the reconstruction of a Gaussian beam with $w_0 = 4.2\ \mu$m for the 3 different sets of PhCs. Increasing the value of r by ~ 10 nm shifts the resonance to shorter λ by ~ 20 nm. This value is quantitatively consistent with the experimental data in Fig. 4.16, and proves that the simulation model captures the essential physics of the problem.

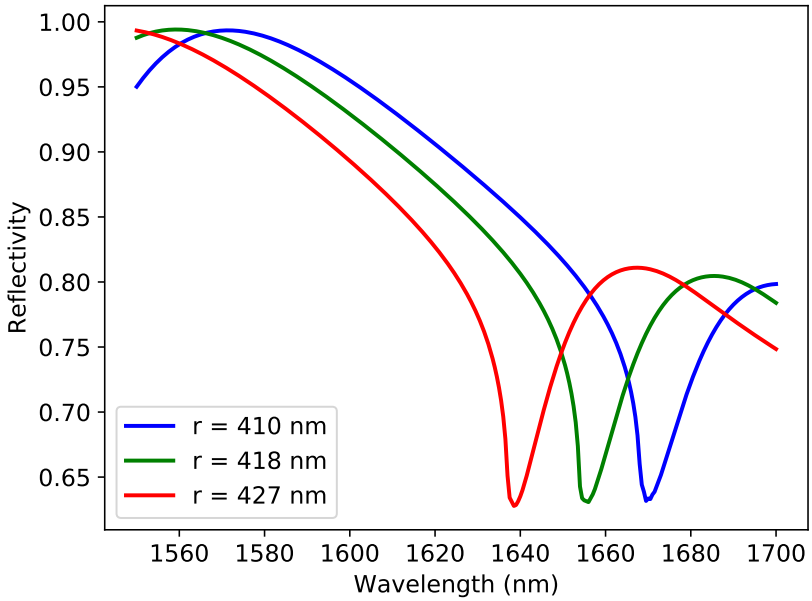

Figure 4.24: Reflectivety simulations of an s-polarized Gaussian beam with $w_0 = 4.2\ \mu$m for different PhC parameters given by Table 4.5.

4.3.4 Resonance dependence on Gaussian beam polarization

The simulations shown so far are for an s-polarized Gaussian beam. To check for the polarization dependence of our structure, the simulations were also done for a p-polarized Gaussian beam. Fig. 4.25 shows the θ dependence of the reflectivity spectrum, after averaging over ϕ, i.e. after averaging over all angles in the plane of incidence. We can see that the curves are identical if the angle θ for one polarization is replaced by $90° - \theta$ for the opposite polarization. Intuitively, one expects that after averaging over all θ then both polarization should give an identical spectrum. This can exactly be seen in Fig. 4.26, where an s-polarized and a p-polarized Gaussian

beam give the same response. This is particularly important for our setup, as the slab is probed by a circularly polarized Gaussian beam which can be described as a superposition of an s-polarized and a p-polarized Gaussian beam. This conclusion is consistent with the one reported in [Moura et al., 2018].

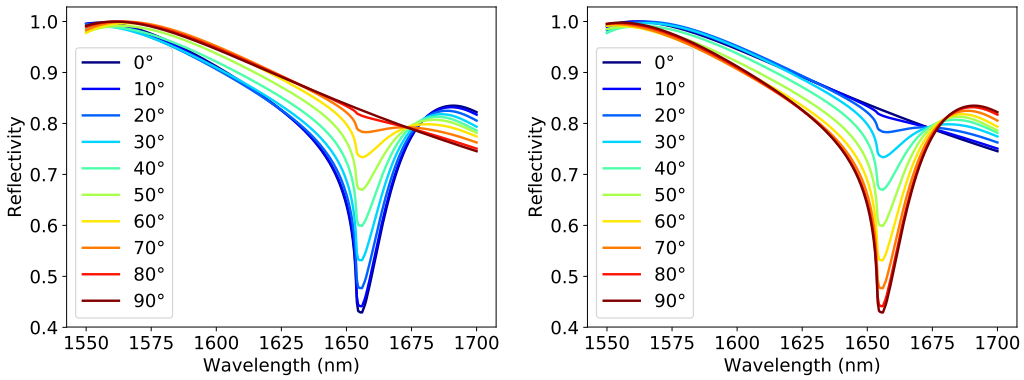

Figure 4.25: Reflectivity spectrum of an s-polarized Gaussian beam for different azimuthal angles θ averaged over all polar angles ϕ. (a) s-polarized Gaussian beam. (b) p-polarized Gaussian beam.

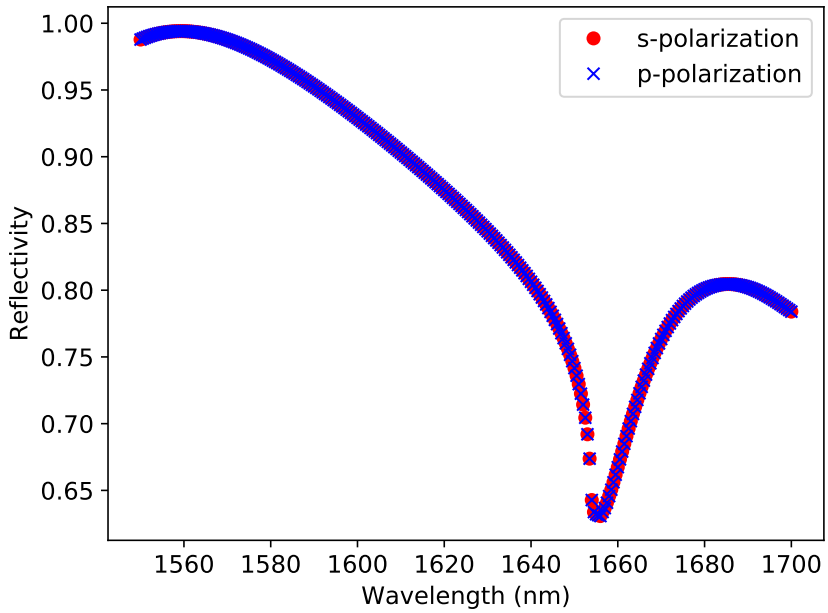

Figure 4.26: Reflectivity simulations of a Gaussian beam with $w_0 = 4.2$ μm for s and p polarization.

5

Conclusion

This work was concerned with the mechanical and optical characterization of GaAs membranes. The device under investigation constitutes the building block of the future goal of building a GaAs-based multi-element optomechanical system. The characterization included both un-patterned devices and PhC-patterned devices. One part of this thesis was concerned with building and/or modifying experimental setups. An optical reflectivity setup was built with the purpose of measuring the reflectivity of GaAs membranes. The *homodyne detection* setup was automated to characterize the eigenfrequenices (ω_m), quality factors (Q_m) and mode shapes of different mechanical eigenmodes.

Mechanical characterization of GaAs membranes showed that the ω_m are significantly shifted to higher frequencies. The shift was highly dependent on the eigenmode, the analysis showed that low frequency modes are significantly more shifted compared to higher frequency modes. This could be explained to be due to anisotropic stress distribution which would shift the eigenmodes differently. Moreover, the PhC-patterned devices showed less shift compared to the un-patterned devices, this led to the hypothesis that the etching of PhC patterns partially relaxes the internal stress in the membrane. Q_m analysis showed a maximum achieved value $\approx 5 \times 10^4$ for an un-patterned GaAs membrane. PhC-patterned membranes showed Q_m of the same order. However, the values achieved are inferior to those reported for GaAs membranes in literature, where Q_m values $> 10^6$ were reported [Liu et al., 2011]. This is mainly attributed to growth problems, as the 100 nm GaAs layer showed a thickness variation of more than 10 nm on the bottom surface.

Devices with PhC patterns optimized for high reflectivity at $\lambda = 1550$ nm were designed and fabricated. Optical characterization showed $R > 98\%$ for several measured devices. However, a peculiar asymmetric resonance dip appeared in the R spectrum. The dip showed large dependence on the radius of the PhC pattern. Beam waist dependent measurements combined with RCWA S^4 simulations showed that the parasitic feature was due to probing the membrane with a Gaussian beam having a certain beam waist. A Gaussian beam can be decomposed into plane waves incident from different direction, and the tilted components excited a parasitic guided resonance in the PhC slab. As a result, when a large Gaussian beam waist is used, it approximates better the behaviour of a plane wave, and the feature starts to vanish. However, large beam waist also lead to large clipping losses when the

beam waist becomes comparable to the membrane size. The simulated response is highly consistent with similar work done on SiN PhC-patterned membranes [Moura et al., 2018].

This work demonstrated a clear trade-off for the membrane dimensions. On one hand, having small pad sizes leads to higher mechanical frequencies which is favorable for optomechanics. However, this requires working with highly focused laser beams to minimize optical losses. Focused Gaussian beams induces parasitic resonances in the R spectrum, and prevent entering the desirable $R > 99.9\%$ regime. Experimental characterization showed that to avoid the parasitic features in the spectrum, a beam waist ≈ 25 μm would be sufficient. But this requires a pad size around an order of magnitude larger to avoid clipping losses.

Future work may include studying the stress patterns in the GaAs membrane, and finding a model which accurately predicts the evolution of ω_m in GaAs membranes for different stress values. Higher quality wafers can be used to understand the main limitation that prevents reaching $Q_m > 10^6$. Furthermore, other PhC pattern parameters can be studied to see if other design parameters have more immunity to parasitic resonances compared to the studied PhC pattern. Finally, it is natural to move to double-membrane devices and characterize them mechanically and optically. This would allow the demonstration of enhanced optomechanical effects.

Bibliography

R. W. Andrews, R. W. Peterson, T. P. Purdy, K. Cicak, R. W. Simmonds, C. A. Regal, and K. W. Lehnert. Bidirectional and efficient conversion between microwave and optical light. *Nature Physics*, 10(4):321, 2014.

G. Anetsberger, R. Rivière, A. Schliesser, O. Arcizet, and T. J. Kippenberg. Ultralow-dissipation optomechanical resonators on a chip. *Nature Photonics*, 2 (10):627, 2008.

O. Arcizet, P.-F. Cohadon, T. Briant, M. Pinard, and A. Heidmann. Radiation-pressure cooling and optomechanical instability of a micromirror. *Nature*, 444 (7115):71, 2006.

M. Aspelmeyer, T. J. Kippenberg, and F. Marquardt. Cavity optomechanics. *Reviews of Modern Physics*, 86(4):1391, 2014.

J. Chan, T. M. Alegre, A. H. Safavi-Naeini, J. T. Hill, A. Krause, S. Gröblacher, M. Aspelmeyer, and O. Painter. Laser cooling of a nanomechanical oscillator into its quantum ground state. *Nature*, 478(7367):89, 2011.

D. Chang, A. H. Safavi-Naeini, M. Hafezi, and O. Painter. Slowing and stopping light using an optomechanical crystal array. *New Journal of Physics*, 13(2):023003, 2011.

G. D. Cole, I. Wilson-Rae, M. R. Vanner, S. Gröblacher, J. Pohl, M. Zorn, M. Weyers, A. Peters, and M. Aspelmeyer. Megahertz monocrystalline optomechanical resonators with minimal dissipation. In *2010 IEEE 23rd International Conference on Micro Electro Mechanical Systems (MEMS)*, pages 847–850. IEEE, 2010.

G. D. Cole, I. Wilson-Rae, K. Werbach, M. R. Vanner, and M. Aspelmeyer. Phonon-tunnelling dissipation in mechanical resonators. *Nature communications*, 2:231, 2011.

A. Dorsel, J. D. McCullen, P. Meystre, E. Vignes, and H. Walther. Optical bistability and mirror confinement induced by radiation pressure. *Phys. Rev. Lett.*, 51:1550–1553, Oct 1983. doi: 10.1103/PhysRevLett.51.1550. URL `https://link.aps.org/doi/10.1103/PhysRevLett.51.1550`.

M. Eichenfield, J. Chan, R. M. Camacho, K. J. Vahala, and O. Painter. Optomechanical crystals. *Nature*, 462(7269):78, 2009.

S. Fan and J. D. Joannopoulos. Analysis of guided resonances in photonic crystal slabs. *Physical Review B*, 65(23):235112, 2002.

C. Gärtner, J. P. Moura, W. Haaxman, R. A. Norte, and S. Groblacher. Integrated optomechanical arrays of two high reflectivity sin membranes. *Nano letters*, 18 (11):7171–7175, 2018.

S. Gigan, H. Böhm, M. Paternostro, F. Blaser, G. Langer, J. Hertzberg, K. C. Schwab, D. Bäuerle, M. Aspelmeyer, and A. Zeilinger. Self-cooling of a micromirror by radiation pressure. *Nature*, 444(7115):67, 2006.

S. Gröblacher. *Quantum opto-mechanics with micromirrors: combining nanomechanics with quantum optics*. Springer Science & Business Media, 2012.

D. Hall. *Musical Acoustics*. Physics Series. Brooks/Cole Publishing Company, 2002. ISBN 9780534377281. URL `https://books.google.se/books?id=abe7AAAAIAAJ`.

G. Heinrich, M. Ludwig, J. Qian, B. Kubala, and F. Marquardt. Collective dynamics in optomechanical arrays. *Phys. Rev. Lett.*, 107:043603, Jul 2011. doi: 10.1103/PhysRevLett.107.043603. URL `https://link.aps.org/doi/10.1103/PhysRevLett.107.043603`.

M. Imboden and P. Mohanty. Dissipation in nanoelectromechanical systems. *Physics Reports*, 534(3):89–146, 2014.

J. D. Joannopoulos, P. R. Villeneuve, and S. Fan. Photonic crystals. *Solid State Communications*, 102(2-3):165–173, 1997.

T. J. Kippenberg, H. Rokhsari, T. Carmon, A. Scherer, and K. J. Vahala. Analysis of radiation-pressure induced mechanical oscillation of an optical microcavity. *Phys. Rev. Lett.*, 95:033901, Jul 2005. doi: 10.1103/PhysRevLett.95.033901. URL `https://link.aps.org/doi/10.1103/PhysRevLett.95.033901`.

J. Liu, K. Usami, A. Naesby, T. Bagci, E. S. Polzik, P. Lodahl, and S. Stobbe. High-q optomechanical gaas nanomembranes. *Applied Physics Letters*, 99(24):243102, 2011.

V. Liu and S. Fan. S4: A free electromagnetic solver for layered periodic structures. *Computer Physics Communications*, 183(10):2233–2244, 2012.

V. Lousse, W. Suh, O. Kilic, S. Kim, O. Solgaard, and S. Fan. Angular and polarization properties of a photonic crystal slab mirror. *Optics express*, 12(8):1575–1582, 2004.

M. Ludwig, B. Kubala, and F. Marquardt. The optomechanical instability in the quantum regime. *New Journal of Physics*, 10(9):095013, 2008.

K. Makles, T. Antoni, A. Kuhn, S. Deléglise, T. Briant, P.-F. Cohadon, R. Braive, G. Beaudoin, L. Pinard, C. Michel, et al. 2d photonic-crystal optomechanical nanoresonator. *Optics letters*, 40(2):174–177, 2015.

F. Marquardt and S. M. Girvin. Optomechanics (a brief review). *arXiv preprint arXiv:0905.0566*, 2009.

J. P. Moura, R. A. Norte, J. Guo, C. Schäfermeier, and S. Gröblacher. Centimeter-scale suspended photonic crystal mirrors. *Optics express*, 26(2):1895–1909, 2018.

B. Nair, A. Naesby, and A. Dantan. Optomechanical characterization of silicon nitride membrane arrays. *Optics letters*, 42(7):1341–1344, 2017.

P. Piergentili, L. Catalini, M. Bawaj, S. Zippilli, N. Malossi, R. Natali, D. Vitali, and G. Di Giuseppe. Two-membrane cavity optomechanics. *New Journal of Physics*, 20(8):083024, 2018.

A. N. Rasmussen. *Optomechanics with Semiconductor Nanomembranes*. PhD thesis, The Niels Bohr Institute, Faculty of Science, University of Copenhagen, 2013.

G. Rempe, R. J. Thompson, H. J. Kimble, and R. Lalezari. Measurement of ultralow losses in an optical interferometer. *Opt. Lett.*, 17(5):363–365, Mar 1992. doi: 10.1364/OL.17.000363. URL `http://ol.osa.org/abstract.cfm?URI=ol-17-5-363`.

B. E. A. Saleh and M. C. Teich. *Fundamentals of photonics; 2nd ed.* Wiley series in pure and applied optics. Wiley, New York, NY, 2007. URL `https://cds.cern.ch/record/1084451`.

A. Schliesser, P. Del'Haye, N. Nooshi, K. J. Vahala, and T. J. Kippenberg. Radiation pressure cooling of a micromechanical oscillator using dynamical backaction. *Phys. Rev. Lett.*, 97:243905, Dec 2006. doi: 10.1103/PhysRevLett.97.243905. URL `https://link.aps.org/doi/10.1103/PhysRevLett.97.243905`.

K. Schneider, P. Welter, Y. Baumgartner, S. Hönl, H. Hahn, L. Czornomaz, and P. Seidler. Optomechanics with one-dimensional gallium phosphide photonic crystal cavities. In *Quantum Nanophotonics*, volume 10359, page 103590K. International Society for Optics and Photonics, 2017.

J. Thompson, B. Zwickl, A. Jayich, F. Marquardt, S. Girvin, and J. Harris. Strong dispersive coupling of a high-finesse cavity to a micromechanical membrane. *Nature*, 452(7183):72, 2008.

V. Tsvirkun. *Optomechanics in hybrid fully-integrated two-dimensional photonic crystal resonators*. PhD thesis, 2015.

E. Ventsel and T. Krauthammer. *Thin Plates and Shells: Theory: Analysis, and Applications*. Taylor & Francis, 2001. ISBN 9780824705756. URL `https://books.google.se/books?id=-veAngEACAAJ`.

L. G. Villanueva and S. Schmid. Evidence of surface loss as ubiquitous limiting damping mechanism in sin micro-and nanomechanical resonators. *Physical review letters*, 113(22):227201, 2014.

K. Wang, A.-C. Wong, and C. T.-C. Nguyen. Vhf free-free beam high-q micromechanical resonators. *Journal of Microelectromechanical Systems*, 9:347–360, 1999.

G. S. Wiederhecker, L. Chen, A. Gondarenko, and M. Lipson. Controlling photonic structures using optical forces. *Nature*, 462(7273):633, 2009.

A. Xuereb, C. Genes, and A. Dantan. Strong coupling and long-range collective interactions in optomechanical arrays. *Physical review letters*, 109(22):223601, 2012.

A. Xuereb, C. Genes, and A. Dantan. Collectively enhanced optomechanical coupling in periodic arrays of scatterers. *Physical Review A*, 88(5):053803, 2013.

H. Yang, D. Zhao, J.-H. Seo, S. Chuwongin, S. Kim, J. A. Rogers, Z. Ma, and W. Zhou. Broadband membrane reflectors on glass. *IEEE Photonics Technology Letters*, 24(6):476–478, 2011.

W. Zhou, D. Zhao, Y.-C. Shuai, H. Yang, S. Chuwongin, A. Chadha, J.-H. Seo, K. X. Wang, V. Liu, Z. Ma, et al. Progress in 2d photonic crystal fano resonance photonics. *Progress in Quantum Electronics*, 38(1):1–74, 2014.